For Xeroxing

PREDICTION OF THREE-DIMENSIONAL COMPRESSIBLE TURBULENT BOUNDARY LAYERS ON TRANSONIC COMPRESSOR BLADES

William James Usab, Jr.

GT&PDL Report No. 152 October 1980

GAS TURBINE & PLASMA DYNAMICS LABORATORY
MASSACHUSETTS INSTITUTE OF TECHNOLOGY
CAMBRIDGE, MASSACHUSETTS

PREDICTION OF THREE-DIMENSIONAL COMPRESSIBLE TURBULENT BOUNDARY LAYERS ON TRANSONIC COMPRESSOR BLADES

William James Usab, Jr.

GT&PDL Report No. 152 October 1980

This research, carried out in the Gas Turbine and Plasma Dynamics Laboratory, MIT, was supported by the NASA Lewis Research Center under Grant No. NAG3-9.

ABSTRACT

A small crossflow approximation to the full three-dimensional compressible turbulent boundary layer equations for turbomachine blade rows is developed by taking advantage of the nature of blade geometry and inviscid flow field when an intrinsic coordinate system is used. The resulting system of equations is solved by Keller's box scheme, providing the capability of numerically calculating compressible turbulent boundary layers on transonic compressor blades to a good approximation. The scheme is checked with two known solutions of incompressible flow over unloaded zero thickness blades. It is then applied to the first stage of a NASA Low-aspect-ratio rotor blade for which the inviscid flow field is available. The results give insight to the three-dimensional boundary layer character of transonic compressor blades, caused by an imbalance of centrifugal and Coriolis forces within the boundary layer.

ACKNOWLEDGEMENTS

The author would like to thank Professor William T. Thompkins Jr. for his many hours of guidance and unending patience through the course of this thesis. Further the author wishes to express his appreciation to those at the United Technologies Research Center, especially Dr. Mike Werle, Dr. Jim Carter, and Dr. Veer Vatsa whose expertise on the subject was invaluable. Finally, special thanks to my wife Karen for typing this thesis and her unwavering support throughout.

This research was supported by NASA Lewis Research Center under grant No. NAG3-9. The support is especially appreciated.

TABLE OF CONTENTS

LIST OF FIGURES

1.0 INTRODUCTION

In recent years there has been a growing effort to understand and improve transonic compressor performance. Design work currently being done in this area depends very heavily on experimental work done in compressor test rigs. Unfortunately the data from these tests is usually limited to measurements between blade rows, providing information on stage performance but very little understanding of the flow detail within the blade passage. This point is particularly true in terms of the boundary layer development on transonic compressor blades. In the past designers have attempted to use standard two dimensional airfoil boundary layer calculations to characterize the flow, but stage performance can only be loosely related to this boundary layer theory. In an effort to predict the boundary layer influence on performance, designers have been forced to rely heavily on the development of correlations based on rig data.

The poor performance of two dimensional airfoil calculations should come as no surprise since the high twist and large rotational speeds encountered in transonic compressors produce large centrifugal and Coriolis forces within the boundary layer making the flow highly three dimensional in nature.

In the past three dimensional boundary layer solutions on rotating blades were limited to a small number of special laminar incompressible cases where similarity or series type solutions could be found. These types of solutions are only possible for the simplest of blade geometries and invisid flows of which the work of Fogary [1] and Tan [2] for helicopter blades and Miyake [3] and Horlock [4] for the helical blades are notable. With the development of efficient numerical schemes full three dimensional turbulent boundary layer calculations are now possible for external wing calculations such as those of Cebeci, Kaups, and Ramecy ref.[5]. Direct extension of one of these three dimensional schemes to rotating transonic blades might seem to be of value. Unfortunately, although the invisid solution is available, these solution schemes also require a complete definition of boundary layer at the hub and tip sections of the blade, information which is not presently available even to a good approximation. Without these initial planes of data any three dimensional calculation would have questionable value.

In light of the need for a better understanding of the three dimensionality of boundary layers in transonic compressors and the difficulty of implimenting a full three dimensional calculation, this thesis develops a small crossflow approximation to the full three dimensional equations. This is made possible by taking advantage

of the nature of transonic blade geometries and invisid flow fields. The resulting set of equations are then solved using Keller's box scheme. This solution scheme presents the capability of numerically calculating laminar/turbulent compressible boundary layers to a good approximation over a majority of the blade.

The solution scheme is checked with the few available simple incompressible solutions. Then the scheme is applied to the NASA low-aspect-ratio transonic compressor stage to investigate possible regions of separation, the amount of boundary layer blockage and the magnitude of radial flow within the boundary layer.

2. DEVELOPMENT OF GOVERNING EQUATIONS

2.1 THREE DIMENSIONAL COMPRESSIBLE TURBULENT BOUNDARY LAYER EQUATIONS

The full three dimensional boundary layer equations for turbulent flow on a rotating blade are derived beginning with the Navier-Stokes equations and a chosen form of the energy equation. The time dependence of the flow due to the blade rotation is eliminated by considering a reference frame fixed with respect to the rotating blade. Expressed in tensor notation the Navier-Stokes equations are given in Mager [6] as:

CONTINUITY

$$\frac{\partial \rho}{\partial t} + (\rho u_j)_{,j} = 0 \tag{2.1}$$

MOMENTUM

$$\rho \left[\frac{\partial u_i}{\partial t} + u_j u_{i,j} + 2(\omega_j u_k - \omega_k u_j) - \omega^2 R R_{,j} \right] = -P_{,j} + \tau_{ij,j} \tag{2.2}$$

ENERGY

$$\rho \left[\frac{\partial I}{\partial t} + u_j I_{,j} \right] = \frac{\partial P}{\partial t} + (u_i \tau_{ij})_{,j} + (k T_{,j})_{,j} \tag{2.3}$$

Where

$$\tau_{ij} = -\frac{2}{3} \mu \delta_{ij} u_{k,k} + \mu (u_{i,j} + u_{j,i}) \tag{2.4}$$

$$I = C_p T + \tfrac{1}{2} u_i u_i - \tfrac{1}{2} \omega^2 R^2 \qquad (2.5)$$

Note in this equation set ω_i are the components of angular velocity of the blade and R is the perpendicular distance from the axis of rotation. The effects of turbulence are isolated in terms of Reynolds stresses after taking suitable time averages of each of the flow quatities. Applying the usual boundary layer approximation of dropping terms of $O(\delta)$ or smaller reduces the governing equations to the standard three dimensional boundary layer form.

It is often convenient in boundary layer calculations to consider the equations of motion in terms of an orthogonal curvalinear coordinate system, as shown in fig. (1), where X_3 has been chosen as the normal to the blade surface. The full three dimensional laminar compressible boundary layer equations are expressed by Mager [6], the full three dimensional turbulent compressible boundary layer equations in non-rotating frame are presented in Cebeci [5] by including the Reynolds stress terms. With the addition of the Reynolds stress terms the full turbulent compressible form in a rotating reference frame becomes:

CONTINUITY

$$\frac{\partial}{\partial x_1}(\rho u_1 h_2 h_3) + \frac{\partial}{\partial x_2}(\rho u_2 h_1 h_3) + \frac{\partial}{\partial x_3}(\rho u_3 h_1 h_2) = 0 \qquad (2.6)$$

X_1 MOMENTUM EQUATION

$$\frac{\rho u_1}{h_1}\frac{\partial u_1}{\partial x_1} + \frac{\rho u_2}{h_2}\frac{\partial u_1}{\partial x_2} + \frac{\rho u_3}{h_3}\frac{\partial u_1}{\partial x_3} + \rho u_2\left[\frac{u_1}{h_1 h_2}\frac{\partial h_1}{\partial x_2} - \frac{u_2}{h_2 h_1}\frac{\partial h_2}{\partial x_1}\right]$$

$$- 2\rho\omega_3 u_2 - \frac{\rho\omega^2 R}{h_1}\frac{\partial R}{\partial x_1} = -\frac{1}{h_1}\frac{\partial P}{\partial x_1} + \frac{1}{h_3}\frac{\partial}{\partial x_3}\left[\frac{\mu}{h_3}\frac{\partial u_1}{\partial x_3} - \rho\overline{u_1' u_3'}\right] \qquad (2.7)$$

X_2 MOMENTUM EQUATION

$$\frac{\rho u_1}{h_1}\frac{\partial u_2}{\partial x_1} + \frac{\rho u_2}{h_2}\frac{\partial u_2}{\partial x_2} + \frac{\rho u_3}{h_3}\frac{\partial u_2}{\partial x_3} + \rho u_1\left[\frac{u_2}{h_1 h_2}\frac{\partial h_2}{\partial x_1} - \frac{u_1}{h_1 h_2}\frac{\partial h_1}{\partial x_2}\right]$$

$$+ 2\rho\omega_3 u_1 - \frac{\rho\omega^2 R}{h_2}\frac{\partial R}{\partial x_2} = -\frac{1}{h_2}\frac{\partial P}{\partial x_2} + \frac{1}{h_3}\frac{\partial}{\partial x_3}\left[\frac{\mu}{h_3}\frac{\partial u_2}{\partial x_3} - \rho\overline{u_2' u_3'}\right] \qquad (2.8)$$

X_3 MOMENTUM EQUATION

$$2\rho(\omega_1 u_2 - \omega_2 u_1) - \frac{\rho\omega^2 R}{h_3}\frac{\partial R}{\partial x_3} = -\frac{1}{h_3}\frac{\partial P}{\partial x_3} \qquad (2.9)$$

ENERGY EQUATION

$$\frac{\rho u_1}{h_1}\frac{\partial I}{\partial x_1} + \frac{\rho u_2}{h_2}\frac{\partial I}{\partial x_2} + \frac{\rho u_3}{h_3}\frac{\partial I}{\partial x_3} = \frac{1}{h_3}\frac{\partial}{\partial x_3}\left[\frac{\mu}{Pr\, h_3}\frac{\partial H}{\partial x_3}\right.$$

$$\left. + \mu\left(1 - \frac{1}{Pr}\right)\left(\frac{u_1}{h_3}\frac{\partial u_1}{\partial x_3} + \frac{u_2}{h_3}\frac{\partial u_2}{\partial x_3}\right) - \rho\overline{H' u_3'}\right] \qquad (2.10)$$

The Reynolds stress terms mentioned above appear as averages of unsteady purturbation quantities ($\rho\overline{u_1' u_3'}$, $\rho\overline{u_2' u_3'}$ $\rho\overline{H' u_3'}$) in the above equation set. In reality the terms shown are only the primary turbulent terms but it is customary to assume the other terms due to curvature and density variations are absorbed in these terms. Later these terms must be modeled and those terms lost will be accounted for in the turbulence model used.

In the energy equation we have defined $I = H - \frac{1}{2}\omega^2 R^2$. In the definition of total enthalpy we have neglected the velocity component normal to the surface so $H = C_p T + \frac{1}{2}(u_1^2 + u_2^2)$.

The choice of coordinates fixed to the blade is apparent in the appearance of Coriolis acceleration terms depending on ω_i , the angular velocity of the blade in local coordinates. In addition R has been defined as the perpendicular distance from the point of rotation.

As discussed in Mager [6] the Coriolis accelerations create a pressure gradient normal to the blade surface which is of 0(1) but, even though this is larger than in usual boundary layer calculations, the total change in pressure across the boundary layer is negligible if the boundary layer thickness is small. This implies the assumption of zero pressure gradient across the boundary layer is still valid. With $\frac{\partial P}{\partial x_3} = 0$ we may express the pressure gradient components, as in standard boundary layer approximations, in terms of the invisid edge flow where:

$$-\frac{1}{h_1}\frac{\partial P}{\partial x_1} = \frac{\rho_e u_{1e}}{h_1}\frac{\partial u_{1e}}{\partial x_1} + \frac{\rho_e u_{2e}}{h_2}\frac{\partial u_{1e}}{\partial x_2} + \frac{\rho_e u_{1e} u_{2e}}{h_1 h_2}\frac{\partial h_1}{\partial x_2} - \frac{\rho_e u_{2e}^2}{h_1 h_2}\frac{\partial h_2}{\partial x_1} - 2\rho_e \omega_3 u_{2e} - \frac{\rho_e \omega^2 R}{h_1}\frac{\partial R}{\partial x_1} \qquad (2.11)$$

$$-\frac{1}{h_2}\frac{\partial P}{\partial x_2} = \frac{\rho_e u_{1e}}{h_1}\frac{\partial u_{2e}}{\partial x_1} + \frac{\rho_e u_{2e}}{h_2}\frac{\partial u_{2e}}{\partial x_2} + \frac{\rho_e u_{1e} u_{2e}}{h_1 h_2}\frac{\partial h_2}{\partial x_1} - \frac{\rho_e u_{1e}^2}{h_1 h_2}\frac{\partial h_1}{\partial x_2} + 2\rho_e \omega_3 u_{1e} - \frac{\rho_e \omega^2 R}{h_2}\frac{\partial R}{\partial x_2} \qquad (2.12)$$

The subscript "e" is used to denote the invisid external flow and ω is taken as constant through the boundary layer.

It is convenient at this point to express the Reynolds stress terms by Boussinesq's eddy viscosity concept in the following forms,

$$-\rho\overline{u_1'u_3'} = \rho\,\varepsilon_m\,\frac{\partial u_1}{\partial x_3} \tag{2.13}$$

$$-\rho\overline{u_2'u_3'} = \rho\,\varepsilon_m\,\frac{\partial u_2}{\partial x_3} \tag{2.14}$$

$$-\rho\overline{H'u_3'} = \rho\,\varepsilon_H\,\frac{\partial H}{\partial x_3} = \rho\left(\frac{\varepsilon_m}{Pr_t}\right)\frac{\partial H}{\partial x_3} \tag{2.15}$$

As will be described in a later section, ε_m is the eddy viscosity which is to be modeled following the work of Cebeci and others.

The boundary conditions that apply to this set of equations, (2.6),(2.7),(2.8) and (2.9), are no-slip at the wall ($X_3 = 0$), prescribed blowing, and prescribed temperature or temperature gradient. At the outer edge of the boundary layer the velocity components and temperature take on the invisid external flow values. In summary then:

@ $x_3 = 0$ $\qquad u_1 = u_2 = 0$ (2.16a)

$$u_3 = u_{3_w}(x_1, x_2) \tag{2.16b}$$

$$T = T_w(x_1, x_2) \quad \text{or} \quad \frac{\partial T}{\partial x_3} = T_w'(x_1, x_2) \tag{2.16c}$$

$$@\ x_3 \to \infty \qquad u_1 \longrightarrow u_{1e}(x_1, x_2) \tag{2.17a}$$

$$u_2 \longrightarrow u_{2e}(x_1, x_2) \tag{2.17b}$$

$$T \longrightarrow T_e(x_1, x_2) \tag{2.17c}$$

Up to this point no simplifications have been made with the coordinate system itself. As Lin [7], Howarth [8] and others have suggested, it is consistent with the standard boundary layer approximations used to this point to restrict the orthogonal system by setting $h_3 = 1$. X_3 is then the true normal distance from the surface of the blade.

In summary the final form of the full three dimensional turbulent compressible boundary layer equations are;

CONTINUITY EQUATION

$$\frac{\partial}{\partial x_1}(\rho u_1 h_2) + \frac{\partial}{\partial x_2}(\rho u_2 h_1) + \frac{\partial}{\partial x_3}(\rho u_3 h_1 h_2) = 0 \tag{2.18}$$

X_1 MOMENTUM EQUATION

$$\frac{\rho u_1}{h_1}\frac{\partial u_1}{\partial x_1} + \frac{\rho u_2}{h_2}\frac{\partial u_1}{\partial x_2} + \rho u_3 \frac{\partial u_1}{\partial x_3} + \rho u_2\left[\frac{u_1}{h_1 h_2}\frac{\partial h_1}{\partial x_2} - \frac{u_2}{h_1 h_2}\frac{\partial h_2}{\partial x_1}\right] - 2\rho w_3 u_2$$

$$- \frac{\rho w^2 R}{h_1}\frac{\partial R}{\partial x_1} = \left[\frac{\rho_e u_{1e}}{h_1}\frac{\partial u_{1e}}{\partial x_1} + \frac{\rho_e u_{2e}}{h_2}\frac{\partial u_{1e}}{\partial x_2} + \frac{\rho_e u_{1e} u_{2e}}{h_1 h_2}\frac{\partial h_1}{\partial x_2}\right.$$

$$\left. - \frac{\rho_e u_{2e}^2}{h_1 h_2}\frac{\partial h_2}{\partial x_1} - 2\rho_e w_3 u_{2e} - \frac{\rho_e w^2 R}{h_1}\frac{\partial R}{\partial x_1}\right] + \frac{\partial}{\partial x_3}\left[\mu\left(1 + \frac{\rho \varepsilon_m}{\mu}\right)\frac{\partial u_1}{\partial x_3}\right] \tag{2.19}$$

X_2 MOMENTUM EQUATION

$$\frac{\rho u_1}{h_1}\frac{\partial u_2}{\partial x_1} + \frac{\rho u_2}{h_2}\frac{\partial u_2}{\partial x_2} + \rho u_3 \frac{\partial u_2}{\partial x_3} + \rho u_1\left[\frac{u_2}{h_1 h_2}\frac{\partial h_2}{\partial x_1} - \frac{u_1}{h_1 h_2}\frac{\partial h_1}{\partial x_2}\right]$$

$$+ 2\rho w_3 u_1 - \frac{\rho w^2 R}{h_2}\frac{\partial R}{\partial x_2} = \left[\frac{\rho_e u_{1e}}{h_1}\frac{\partial u_{2e}}{\partial x_1} + \frac{\rho_e u_{2e}}{h_2}\frac{\partial u_{2e}}{\partial x_2} + \frac{\rho_e u_{1e} u_{2e}}{h_1 h_2}\frac{\partial h_2}{\partial x_1}\right.$$

$$\left. - \frac{\rho_e u_{1e}^2}{h_1 h_2}\frac{\partial h_1}{\partial x_2} + 2\rho_e w_3 u_{1e} - \frac{\rho_e w^2 R}{h_2}\frac{\partial R}{\partial x_2}\right] + \frac{\partial}{\partial x_3}\left[\mu\left(1 + \frac{\rho \varepsilon_m}{\mu}\right)\frac{\partial u_2}{\partial x_3}\right] \tag{2.20}$$

X_3 MOMENTUM EQUATION

$$\frac{\partial P}{\partial x_3} = 0 \tag{2.21}$$

ENERGY EQUATION

$$\frac{\rho u_1}{h_1}\frac{\partial H}{\partial x_1} + \frac{\rho u_2}{h_2}\frac{\partial H}{\partial x_2} - \rho u_3 \frac{\partial H}{\partial x_3} - \omega^2 R\left[\frac{u_1}{h_1}\frac{\partial R}{\partial x_1} + \frac{u_2}{h_2}\frac{\partial R}{\partial x_2} + u_3\frac{\partial R}{\partial x_3}\right]$$

$$= \frac{\partial}{\partial x_3}\left[\frac{\mu}{P_r}\left(1 + \frac{P_r}{P_{r_t}}\frac{\rho \varepsilon_m}{\mu}\right)\frac{\partial H}{\partial x_3} + \mu\left(1 - \frac{1}{P_r}\right)\left(u_1\frac{\partial u_1}{\partial x_3} + u_2\frac{\partial u_2}{\partial x_3}\right)\right] \tag{2.22}$$

Where

$$H = C_p T + \frac{1}{2}\left(u_1^2 + u_2^2\right) \tag{2.23a}$$

BOUNDARY CONDITIONS

$$@\ x_3 = 0 \qquad u_1 = u_2 = 0 \qquad u_3 = u_{3w}(x_1, x_2) \tag{2.24a,b}$$

$$T = T_w(x_1, x_2) \quad \text{or} \quad \frac{\partial T}{\partial x_3} = T_w'(x_1, x_2) \tag{2.24c}$$

$$@\ x_3 \to \infty \qquad u_1 \to u_{1e}(x_1, x_2) \tag{2.25a}$$

$$u_2 \to u_{2e}(x_1, x_2) \tag{2.25b}$$

$$T \to T_e(x_1, x_2) \tag{2.25c}$$

2.2 NATURE OF THE FULL THREE DIMENSIONAL EQUATIONS

With little effort it can be shown that the full three dimensional boundary layer equations as given in the previous section are of parabolic class type but, as Ketchen and Lidney [9] point out, it may be more appropriate to say the equations have a dominant parabolic property with a secondary property hyperbolic in nature. It is this hyperbolic property which affects the accuracy and stability of present numerical solution schemes. To gain accuracy and stability of numerical schemes one must pay close attention to the zone of dependence and step sizes of the chosen solution scheme.

We now consider in an over simplified sense the zones of dependence of a general grid on a flat plate blade as shown in fig.(2). Assuming the boundary conditions are known as given in equations (2.24a,b,c) and (2.25a,b,c) we will consider what initial conditions are required to solve the boundary layer flow over the blade. In addition we will assume the U_1 velocity is always positive and the crossflow velocity U_2 is also positive. To implement a general marching scheme, as those used frequently for external wing calculations, requires two orthogonal initial planes of data. Over plane 1 and 2 shown in fig.(2) the temperature and all velocity components are

required. Plane 1 generally can be computed by a similarity or stagnation line solution, but plane 2 must come from some other source assumed known. With U_1 and U_2 being positive the solution across the boundary layer at each (X_1 , X_2) node can be found satisfying the required zone of dependence by the following marching scheme. Starting at the intersection of the two planes we march one step in X_1 then sweep through each X_2. This marching scheme is then repeated down the entire blade. No comment has been made on the actual step size though there are restrictions more closely dependent on the chosen solution scheme. It becomes obvious, even in this simple example, that if the crossflow U_2 becomes negative the zone of dependence requirement will be violated. The remainder of this sweep may only be found by marching from yet a third plane of data, plane 3.

For a complete solution over a general blade with the possibility of negative crossflows then would require three initial planes of data. Plane 1 is easily found from stagnation line solutions but at once the problem of generating the other two planes at hub and tip sections is encountered. In these regions very little is known either experimentally or through numerical solutions. Attempting to provide a full three dimensional calculation without correct initial conditions in these regions would have

questionable value. This problem of intial data for three dimensional calculations leads us to look for further simplifications that are possible when transonic compressor blades are considered which will enable a prediction of three dimensional boundary layers on transonic blades.

2.3 INTRINSIC COORDINATES AND BLADE PROPERTIES

The first step in specializing the equations for transonic compressor blades is in the choice of grid geometry on the blade surface. An intrinsic coordinate system was chosen since it greatly simplifies the outer flow boundary conditions. The essence of this system is the choice of invisid streamlines as one family of coordinate lines, lines of constant X_2. The other coordinate family, lines of constant X_1, are then orthogonal trajectories of the invisid streamlines as shown in fig. (3). The outer flow boundary conditions and pressure gradient expressions are simplified since the velocity component normal to streamlines is identically zero over the entire invisid flow field. This coordinate system also leads to the possibility of small crossflow solutions since the crossflow velocity U_2 is zero at the wall and outer flow as is discussed later. This system has the added benefit that an intrinsic coordinate system requires the least amount of input data manipulation in predicting boundary layers from invisid data generated by Thompkins [10], an important objective of this thesis.

The equations can be simplified still further by considering the actual blade geometry of a common transonic compressor blade. Typical blade sections at hub, midspan,

and tip are shown in fig.(4) from which the following points can be seen. The transonic blade shown has a very sharp leading edge, approximately a knife edge. This will later lead to assumptions on the type of stagnation line solution. The sections each have very large radius of curvature, both suction and pressure side. Further fig.(5) shows typical invisid streamlines over the surface of the blade. Again the radius of curvature of streamlines is very large. Since the total radius of curvature of streamlines on both the pressure and suction sides of this blade are very large,or nearly straight, the assumption of no curvature of streamlines ($h_1 = h_2 = 1$) seems to be valid. This statement is nearly correct except that as will be shown later, the terms containing the curvature of coordinate lines

$$K_1 = \frac{1}{h_1 h_2} \frac{\partial h_1}{\partial \kappa_2} \tag{2.26a}$$

$$K_2 = \frac{1}{h_1 h_2} \frac{\partial h_2}{\partial \kappa_1} \tag{2.26b}$$

may be important in obtaining correct solutions since the acceleration represented by these terms may not be small. It is then important to retain these terms while taking $h_1 = h_2 = 1$ elsewhere. This reduces the governing equations to the following,

CONTINUITY EQUATION

$$\frac{\partial}{\partial \kappa_1}(\rho u_1) + \frac{\partial}{\partial \kappa_2}(\rho u_2) + \frac{\partial}{\partial \kappa_3}(\rho u_3) = 0 \tag{2.27}$$

X_1 MOMENTUM EQUATION OR STREAMWISE EQUATION

$$\rho u_1 \frac{\partial u_1}{\partial x_1} + \rho u_2 \frac{\partial u_1}{\partial x_2} + \rho u_3 \frac{\partial u_1}{\partial x_3} + \rho u_2 [u_1 k_1 - u_2 k_2] - 2\rho \omega_3 u_2$$

$$-\rho \omega^2 R \frac{\partial R}{\partial x_1} = \rho_e u_{1e} \frac{\partial u_{1e}}{\partial x_1} - \rho_e \omega^2 R \frac{\partial R}{\partial x_1} + \frac{\partial}{\partial x_3}\left[\mu\left(1 + \frac{\rho \varepsilon_m}{\mu}\right) \frac{\partial u_1}{\partial x_3}\right] \tag{2.28}$$

X_2 MOMENTUM EQUATION OR CROSSFLOW EQUATION

$$\rho u_1 \frac{\partial u_2}{\partial x_1} + \rho u_2 \frac{\partial u_2}{\partial x_2} + \rho u_3 \frac{\partial u_2}{\partial x_3} + \rho u_1 [u_2 k_2 - u_1 k_1] + 2\rho \omega_3 u_1$$

$$-\rho \omega^2 R \frac{\partial R}{\partial x_2} = -\rho_e u_{1e}^2 k_1 + 2\rho_e \omega_3 u_{1e} - \rho_e \omega^2 R \frac{\partial R}{\partial x_2}$$

$$+ \frac{\partial}{\partial x_3}\left[\mu\left(1 + \frac{\rho \varepsilon_m}{\mu}\right) \frac{\partial u_2}{\partial x_3}\right] \tag{2.29}$$

ENERGY EQUATION

$$\rho u_1 \frac{\partial H}{\partial x_1} + \rho u_2 \frac{\partial H}{\partial x_2} + \rho u_3 \frac{\partial H}{\partial x_3} - \omega^2 R\left[u_1 \frac{\partial R}{\partial x_1} + u_2 \frac{\partial R}{\partial x_2} + u_3 \frac{\partial R}{\partial x_3}\right]$$

$$= \frac{\partial}{\partial x_3}\left[\frac{\mu}{Pr}\left(1 + \frac{Pr}{Pr_T} \frac{\rho \varepsilon_m}{\mu}\right) \frac{\partial H}{\partial x_3} + \mu\left(1 - \frac{1}{Pr}\right)\left(u_1 \frac{\partial u_1}{\partial x_3} + u_2 \frac{\partial u_2}{\partial x_3}\right)\right] \tag{2.30}$$

Where $$H = C_p T + \frac{1}{2}(u_1^2 + u_2^2) \tag{2.31}$$

BOUNDARY CONDITIONS

@ $x_3 = 0$ $\qquad u_1 = u_2 = 0 \qquad u_3 = u_{3w}(x_1, x_2)$ (2.32a,b)

$$T = T_w(x_1, x_2) \text{ OR } \frac{\partial T}{\partial x_3} = T_w'(x_1, x_2) \tag{2.32c}$$

@ $x_3 \to \infty$ $\qquad u_1 \to u_{1e}(x_1, x_2)$ (2.33a)

$$u_2 \to 0 \tag{2.33b}$$

$$T \to T_e(x_1, x_2) \tag{2.33c}$$

It is convenient at this point to call the X_1 momentum equation the streamwise momentum equation, and the X_2 momentum equation the crossflow equation. In essence the problem has been reduced to the application of an invisid velocity distribution and an associated Coriolis force field to a flat plate blade. The solution of these equations is then the boundary layer solution along invisid streamlines of the actual blade.

2.4 SMALL CROSSFLOW APPROXIMATION

Although consideration of the invisid flow field, blade geometry, and coordinate system have reduced the equations to a much simpler form, the resulting equations still remain a highly coupled system presenting the same problems mentioned in section 2.2. It will now be assumed that gradients of all flow properties in the X_2 direction are zero, with the exception of the Coriolis force terms. This reduces the coupling of the X_2 momentum equation with the other equations. It is to some extent equivalent to the small crossflow approximation and is a valid approximation in many regions on compressor blades. This assumption is at least valid in a first approximation over a majority of the blade, and provides insight to the characteristic of the boundary layer three dimensionality without having to deal with the complications of a full three dimensional calculation. It must be realized that, although of great value, this approximation is not as strong as the standard boundary layer approximations used to this point.

Finally, considering the curvature terms, (terms containing K_1 or K_2) in equations (2.28) and (2.29), the term containing K_2 is always of smaller order than that containing K_1 and is therefore negligible. This is

true since in both equations the term contining K_2 is of higher order in U_2 than the other term and U_2 is assumed small. Also refering back to fig.(5) it is apparent that the streamlines are locally parallel which implies $K_2=0$ identically.

For generality no assumptions about the relative ordering of the Coriolis acceleration terms will be made since it requires no additional effort to include them and those terms that are higher order will not effect the calculation. After dropping the terms mentioned above the final equation set results,

EQUATION SET 1:
CONTINUITY EQUATION

$$\frac{\partial}{\partial x_1}(\rho u_1) + \frac{\partial}{\partial x_2}(\rho u_3) = 0$$

(2.34)

STREAMWISE MOMENTUM EQUATION

$$\rho u_1 \frac{\partial u_1}{\partial x_1} + \rho u_3 \frac{\partial u_1}{\partial x_3} + \underline{\rho u_1 u_2 k_1 - 2\rho\omega_3 u_2} - \rho\omega^2 R \frac{\partial R}{\partial x_1}$$
$$= \rho_e u_{1e} \frac{\partial u_{1e}}{\partial x_1} - \rho_e \omega^2 R \frac{\partial R}{\partial x_1} + \frac{\partial}{\partial x_3}\left[\mu\left(1 + \frac{\rho\varepsilon_m}{\mu}\right)\frac{\partial u_1}{\partial x_3}\right]$$

(2.35)

ENERGY EQUATION

$$\rho u_1 \frac{\partial H}{\partial x_1} + \rho u_3 \frac{\partial H}{\partial x_3} - \rho\omega^2 R\left[u_1 \frac{\partial R}{\partial x_1} + u_2 \frac{\partial R}{\partial x_2} + u_3 \frac{\partial R}{\partial x_3}\right]$$
$$= \frac{\partial}{\partial x_3}\left[\frac{\mu}{Pr}\left(1 + \frac{Pr}{Pr_T}\frac{\rho\varepsilon_m}{\mu}\right)\frac{\partial H}{\partial x_3} + \mu\left(1 - \frac{1}{Pr}\right)\left(u_1 \frac{\partial u_1}{\partial x_3}\right)\right]$$

(2.36)

EQUATION SET 2:
CROSSFLOW MOMENTUM EQUATION

$$\rho u_1 \frac{\partial u_2}{\partial x_1} + \rho u_3 \frac{\partial u_2}{\partial x_3} - \rho u_1^2 k_1 + 2\rho \omega_3 u_1 - \rho \omega^2 R \frac{\partial R}{\partial x_2}$$
$$= -\rho_e u_{1e}^2 k_1 - 2\rho_e \omega_3 u_{1e} - \rho_e \omega^2 R \frac{\partial R}{\partial x_2}$$
$$+ \frac{\partial}{\partial x_3}\left[\mu\left(1 + \frac{\rho \varepsilon_m}{\mu}\right)\frac{\partial u_2}{\partial x_3}\right] \qquad (2.37)$$

Through the assumption of small crossflow, all the important coupling terms have dropped out, with the exception of the Coriolis force terms and curvature terms on which no additional assumptions have been made. As a result the crossflow equation is now only weakly coupled to the continuity-streamwise momentum-energy equation set. The two initial data planes are no longer required for solution of the boundary layer over the compressor blade. Instead it is possible to march independently along each streamline in the following manner. Starting with the attachment line solution, first the combined continuity-streamwise momentum-energy equation set is solved without the underlined coupling term followed by solution of the crossflow equation. Then the term dropped in the first set is inserted and iteration between the two equation sets is repeated until convergence. This is then repeated at each point down the streamline.

After studying the form of the first equation set, it becomes clear that this is the standard two dimensional

boundary layer equation set with the addition of special body force terms. Following the solution of this set there remains a simple ordinary differential equation for the crossflow velocity. With the underlined weakly coupling term included, iteration is required for a good solution.

2.5 FLUID PROPERTIES

In addition to the equations of motion discussed thus far, an equation of state is required to relate pressure, density, and temperature. For the range of temperatures, Mach numbers and types of gases involved it is sufficient to use the ideal gas law $P = \rho R T$. (2.38)

The viscocity is determined through use of Sutherland's Law as describe in Schlicting [11],

$$\frac{\mu}{\mu_0} = \left(\frac{T}{T_0}\right)^{3/2} \frac{T_0 + S_1}{T + S_1} \tag{2.39}$$

where μ_0 denotes the viscocity at reference temperature T_0 and S_1 is a constant which for air is 110 K.

The Prandtl number is also required but is only a function of temperature. For the range of temperatures encountered in transonic compressor calculations the variation in Prandtl number is small enough that it maybe taken as a constant evaluated at the average wall temperature of the blade. Finally the turbulent Prandtl number for air has been taken as constant equal to 0.9.

2.6 TURBULENCE MODELS

The problem of turbulence modeling can be very complex and at this point in time is often looked upon as a kind of "Black Art" in the sense that there is very little theoretical basis for the choice of one model over another except that a model does or does not fit experimental data. Since the main point of this work is development of an efficient scheme to predict crossflows on compressor blades, no attempt has been made to develop a detailed well tuned turbulence model with complex determination of transition. Since it was desired to have the capability of computing either standard two dimensional flows or the small crossflow approximation to three dimensional flows, two different turbulence models are provided below. The first is a simple two dimensional model while the second is a full three dimensional model.

2.6.1 CEBECI'S TWO DIMENSIONAL TURBULENCE MODEL

The following is a simple version of Cebeci's extension to Van Driest's two layer mixing length model described in Cebeci [12] without any form of transition. This model has been will tuned to yield excellent results for a variety of two dimensional flows. Included in this

model are corrections for pressure gradient and wall blowing, although no cases were considered with wall blowing.

TWO LAYER MODE
INNER REGION:

$$(\varepsilon_m)_i = L^2 \left| \partial u_1 / \partial x_3 \right| \tag{2.40a}$$

$$L = k\, x_3 \left[1 - \exp(-x_3/A)\right] \tag{2.40b}$$

$$A = 26 \frac{\nu}{N} \left(\frac{\tau_w}{\rho_w}\right)^{1/2} \left(\rho/\rho_w\right)^{1/2} \tag{2.40c}$$

FOR $u_{3w}=0$ NO WALL BLOWING,

$$N = \left[1 - 11.8 \left(\mu_w/\mu_e\right)\left(\rho_e/\rho_w\right)^2 p^+\right]^{1/2} \tag{2.40d}$$

$$p^+ = \left(\nu_e u_{1e}/u_\tau^3\right)\left(d u_{1e}/dx_1\right) \tag{2.40e}$$

$$u_\tau = \left(\tau_w/\rho_w\right)^{1/2} \tag{2.20f}$$

$$k = 0.4 \tag{2.40g}$$

OUTER REGION:

$$(\varepsilon_m)_o = \alpha \left| \int_o^\infty (u_{1e} - u_1)\, dx_3 \right|$$

$$\alpha = 0.0168 \tag{2.41}$$

Location of inner and outer regions is at point where

$$(\varepsilon_m)_i = (\varepsilon_m)_o \ .$$

2.6.2 THREE DIMENSIONAL TURBULENCE MODEL

The model used in all small crossflow turbulent calculations in this thesis is an extension of the two dimensional version presented above. This model is again a simple two layer mixing length model described in

Cebeci [5], which has been applied to many three dimensional turbulent calculations including swept infinite cylinders and wing calculations. In the form presented here the outer region model has been modified as discussed in Mellor [13].

INNER REGION:

$$(\varepsilon_m)_i = \ell^2 \left[\left(\partial u_1 / \partial x_3 \right)^2 + \left(\partial u_2 / \partial x_3 \right)^2 \right]^{1/2} \tag{2.42a}$$

$$\ell = 0.4\, x_3 \left[1 - \exp\left(-x_3 / A \right) \right] \tag{2.42b}$$

$$A = 26 \frac{\nu}{u_\tau} \left(\rho / \rho_w \right)^{1/2} \tag{2.42c}$$

$$u_\tau = \left(\tau_{tw} / \rho_w \right)^{1/2} \tag{2.42d}$$

$$\tau_{w_t} = \mu_w \left[\left(\frac{\partial u_1}{\partial x_3} \right)_w^2 + \left(\frac{\partial u_2}{\partial x_3} \right)_w^2 \right]^{1/2} \tag{2.42e}$$

OUTER REGION

$$(\varepsilon_m)_o = 0.0168 \int_0^\infty x_3 \left[\left(\frac{\partial u_1}{\partial x_3} \right)^2 + \left(\frac{\partial u_2}{\partial x_3} \right)^2 \right]^{1/2} dx_3 \tag{2.43}$$

Location of inner and outer regions is at point where $(\varepsilon_m)_i = (\varepsilon_m)_o$.

2.7 SUMMARY OF SMALL CROSSFLOW EQUATIONS

Before proceeding with the actual solution of the small crossflow equations it is convenient to non-dimensionalize the equations. This places the equations in a form where variables in the boundary layer code are directly compatible with those in the invisid code developed by Thompkins. This process also eliminates many of the problems associated with formulating a dimensionally consistent set of input data. The non-dimensionalization of the equations is carried out in appendix I. It should be noted that by correctly scaling X_3, the normal coordinate, and U_3, the normal velocity by the square root of the reference Reynolds number the resulting equation set retains the original form. In addition it is convenient to group the Coriolis acceleration terms in each equation into one term. Handling the acceleration terms in this manner makes it possible to also provide a standard two dimensional capability for non-blade applications of the code. The final form is then summarized below.

EQUATION SET 1
CONTINUITY EQUATION

$$\frac{\partial}{\partial x_1}(\rho u_1) + \frac{\partial}{\partial x_3}(\rho u_3) = 0 \qquad (2.44)$$

STREAMWISE MOMENTUM EQUATION

$$\rho u_1 \frac{\partial u_1}{\partial x_1} + \rho u_3 \frac{\partial u_1}{\partial x_3} = \rho_e u_{1e} \frac{\partial u_{1e}}{\partial x_1} + \frac{\partial}{\partial x_3}\left[\mu\left(1 + \frac{\rho \varepsilon_m}{\mu}\right)\frac{\partial u_1}{\partial x_3}\right] + F_1 \tag{2.45a}$$

$$F_1 = -\rho u_1 u_2 k_1 + 2\rho \omega_3 u_2 + \rho \omega^2 R \frac{\partial R}{\partial x_1} - \rho_e \omega^2 R \frac{\partial R}{\partial x_1} \tag{2.45b}$$

ENERGY EQUATION

$$\rho u_1 \frac{\partial H}{\partial x_1} + \rho u_3 \frac{\partial H}{\partial x_3} = \frac{\partial}{\partial x_3}\left[\frac{\mu}{Pr}\left(1 + \frac{Pr}{Pr_T}\frac{\rho \varepsilon_m}{\mu}\right)\frac{\partial H}{\partial x_3} + \mu\left(1 - \frac{1}{Pr}\right) u_1 \frac{\partial u_1}{\partial x_3}\right] + E \tag{2.46a}$$

$$E = \rho \omega^2 R\left[u_1 \frac{\partial R}{\partial x_1} + u_2 \frac{\partial R}{\partial x_2} + u_3 \frac{\partial R}{\partial x_3}\right] \tag{2.46b}$$

EQUATION SET II:
CROSSFLOW MOMENTUM EQUATION

$$\rho u_1 \frac{\partial u_2}{\partial x_1} + \rho u_3 \frac{\partial u_2}{\partial x_3} = \frac{\partial}{\partial x_3}\left[\mu\left(1 + \frac{\rho \varepsilon_m}{\mu}\right)\frac{\partial u_2}{\partial x_3}\right] + F_2 \tag{2.47a}$$

$$F_2 = \rho u_1^2 k_1 - 2\rho \omega_3 u_1 + \rho \omega^2 R \frac{\partial R}{\partial x_2} - \rho_e u_{1e}^2 k_1 + 2\rho_e \omega_3 u_{1e} - \rho_e \omega^2 R \frac{\partial R}{\partial x_2} \tag{2.47b}$$

FLUID PROPERTIES:
EQUATION OF STATE

$$\gamma P = \rho T \tag{2.48}$$

SUTHERLAND'S LAW

$$\mu = T^{3/2}\left[\frac{1+\bar{K}}{T+\bar{K}}\right] \tag{2.49a}$$

$$\bar{K} = S/T_0 \tag{2.49b}$$

BOUNDARY CONDITIONS ALONG STREAMLINE:

$$@\ x_3 = 0 \qquad u_1 = u_2 = 0 \qquad u_3 = u_{3w}(x_1) \tag{2.50a,b}$$

$$T = T_w(x_1) \quad \text{OR} \quad \frac{\partial T}{\partial x_3} = T'(x_1) \tag{2.50c}$$

$$@\ x_3 \to \infty \qquad u_1 \to u_{1e}(x_1) \tag{2.51a}$$

$$u_2 \to 0 \tag{2.51b}$$

$$T \to T_e(x_1) \tag{2.51c}$$

3. NUMERICAL SOLUTION OF SMALL CROSSFLOW EQUATIONS

The small crossflow approximation of the full three dimensional boundary layer equations requires numerical solution of the streamwise equation set, which is in essence a modified form of the standard two dimensional boundary layer equations. Once U_1, U_3 and H are known the crossflow equation is simply an ordinary differential equation. The numerical method used here, often called Keller's Box Method, was first developed by Keller and later applied to boundary layer problems by Cebeci and Keller [14 , 15 , 16 , 17]. Keller's Box Method is much faster and more flexible than the many other methods that exist. In addition, by proper scaling of the equations, similarity solutions are generated with little effort.

The key to the effectiveness of Keller's Box Scheme is expressing each of the governing equations, as a system of first order equations. This is accomplished by defining new unknown functions as normal or X_3 derivatives of the boundary layer variables. Derivatives which appear in each of the other directions are only first order due to the boundary layer approximations already made. The resulting system can then easily be discretized on an arbitrary rectangular mesh using only first order centered-difference quotients and averages at the midpoint of each rectangle to obtain an $O(\delta^2)$ accurate finite-difference equation

set. The resulting system remains highly nonlinear and implicit requiring application of Newton's Method coupled with an efficient block-tridiagonal factorization scheme to solve. The complete process produces an efficient unconditionally stable scheme.

A detailed description of this method applied to two dimensional and axisymetric laminar/turbulent boundary layers is given in Cebeci and Smith [17]. The following sections show the development of this scheme with the addition of the Coriolis accelaration terms to solve the streamwise equation set. Then Keller's box scheme is used to solve the crossflow equation.

3.1 TRANSFORMATION OF EQUATIONS

Before solving the governing equations it is convenient to remove the singularity at $X_1=0$ and scale X_1 and X_3 coordinates by introducing the Levy-Lees transformation as described in Hayes and Probstein [18].

$$d\xi = \rho_e \mu_e u_{1e} dx_1 \qquad d\eta = \left[\frac{\rho u_{1e}}{(2\xi)^{1/2}}\right] dx_3 \qquad (3.1a,b)$$

This coordinate stretching not only removes the leading edge singularity, allowing stagnation point calculations, but also removes the large variation in the boundary layer thickness. For laminar calculations the boundary layer thickness and profile remain essentially constant for similar flows and varies only slightly for nonsimilar flows. Even the extreme turbulent boundary layer growth is substantially reduced although not removed. This scaling then speeds convergence and reduces the need for addition of grid points to capture the boundary layer growth as the computation proceeds.

The continuity equation (2.44) is satisfied identically through introduction of the streamfunction ψ, where

$$\frac{\partial \psi}{\partial x_3} = \rho u_1 \qquad -\frac{\partial \psi}{\partial x_1} = \rho u_3 \qquad (3.2a,b)$$

ψ may be written in terms of a nondimensional streamfunction f a function of the new coordinates ξ, η.

$$\psi(x_1, x_2) = (2\xi)^{1/2} f(\xi, \eta) \qquad (3.3)$$

In terms of this streamfunction the velocities U_1 and U_3

become conveniently, $u_1 = u_{1e} f'$ (3.4)

and $\rho u_3 = -\rho_e \mu_e u_{1e} (2\xi)^{1/2} \left[\frac{f}{2\xi} + \frac{\partial f}{\partial \xi} + f' \left(\frac{\partial \eta}{\partial \xi} \right)_\eta \right]$ (3.5)

(NOTE: Primes denote differentiation with respect to η)

Introducing these transformations into the streamwise equation set, equations (2.44, 2.45, 2.46), yields the following,

STREAMWISE EQUATION SET:
STREAMWISE MOMENTUM

$$[b f''] + f f'' + \beta [C - (f')^2] - D_1 f' w = 2\xi \left[f' \frac{\partial f'}{\partial \xi} - f'' \frac{\partial f}{\partial \xi} \right] + E_1 \quad (3.6)$$

ENERGY

$$[a_1 g' + a_2 f' f'']' + f g' - \beta^* f' g = 2\xi \left[f' \frac{\partial g}{\partial \xi} - g' \frac{\partial f}{\partial \xi} \right] + E_2 \quad (3.7)$$

Where

$$f' = \frac{u_1}{u_{1e}} \qquad g = \frac{H}{H_e} \qquad w = \frac{u_2}{u_{1e}}$$

$$E_1 = -D_2 w + D_3 (1 - C) \qquad E_2 = D_5 f' + D_6 w$$

$$b = C (1 + \varepsilon_m^+) \qquad C = \frac{\rho \mu}{\rho_e \mu_e} \qquad c = \frac{\rho_e}{\rho} \qquad \beta = \frac{2\xi}{u_{1e}} \frac{\partial u_{1e}}{\partial \xi}$$

$$\beta^* = \frac{2\xi}{H_e} \frac{\partial H_e}{\partial \xi} \qquad \varepsilon_m^+ = \frac{\rho \varepsilon_m}{\mu} \qquad a_1 = C \frac{1}{Pr} \left(1 + \varepsilon_m^+ \frac{Pr}{Pr_T} \right)$$

$$a_2 = C \left(1 - \frac{1}{Pr} \right) \frac{u_{1e}^2}{H_e} \qquad D_1 = \frac{2\xi}{\rho_e \mu_e u_{1e}} k_1 \qquad D_2 = \frac{2\xi \omega_3}{\rho_e \mu_e u_{1e}^2}$$

$$D_3 = \frac{2\xi \omega^2 R}{\rho_e \mu_e u_{1e}^3} \frac{\partial R}{\partial x_1} \qquad D_5 = \frac{2\xi \omega^2 R}{\rho_e \mu_e u_{1e} H_e} \frac{\partial R}{\partial x_1}$$

$$D_6 = \frac{2\xi \omega^2 R}{\rho_e \mu_e u_{1e} H_e} \frac{\partial R}{\partial x_2}$$

NOTE: As above, from this point on primes denote derivatives with respect to η , the scaled normal coordinate to the surface.

The simple form of the above equation set comes as no surprise since it was for this reason that the non-dimensional streamfunction of equation (3.3) was defined. It is interesting to find these transformations also work well on the crossflow equation (2.47).

CROSSFLOW EQUATION SET:
CROSSFLOW MOMENTUM

$$[b\,w']' + f w' - \beta f' w = 2\xi\left[f'\frac{\partial w}{\partial \xi} - w'\frac{\partial f}{\partial \xi}\right] + E_3 \tag{3.8}$$

Where

$$E_3 = D_1\left[c - (f')^2\right] + D_2\left[f' - c\right] + D_4\left[1 - c\right]$$

$$D_4 = \frac{2\xi w^2 R}{\rho_e \mu_e u_{1e}^3}\frac{\partial R}{\partial x_2}$$

To complete the transformation of equation, the transformed boundary conditions are,

@ $\eta = 0$

$$f'(\xi,0) = w(\xi,0) = 0 \tag{3.9a,b}$$

$$f(\xi,0) = f_w(\xi) = -\frac{1}{(2\xi)^{1/2}}\int_0^{\xi}\frac{u_{3w}}{u_{1e}\,c_w}\frac{\rho}{\mu_e}\,d\xi \tag{3.9c}$$

$$g(\xi,0) = g_w(\xi) \quad \text{OR} \quad g'(\xi,0) = g'_w(\xi) \tag{3.9d}$$

@ $\eta \to \infty$

$$f'(\xi,\eta) \to 1 \tag{3.10a}$$

$$w(\xi,\eta) \to 0 \tag{3.10b}$$

$$g(\xi,\eta) \to 1 \tag{3.10c}$$

3.2 COMPUTATIONAL GRID

One of the many advantages of Keller's box scheme is the extreme flexability of the grid that may be used. A general grid is shown in fig.(6) where the notation (ξ_n, η_j) is used to denote mesh points.

$$\xi_0 = 0 \qquad \xi_n = \xi_{n-1} + k_n \qquad n = 1, 2, 3 \ldots N \tag{3.11a}$$

$$\eta_0 = 0 \qquad \eta_j = \eta_{j-1} + h_j \qquad j = 1, 2, 3 \ldots J \tag{3.11b}$$

The mesh spacing k_n and h_j are completely arbitrary at this point, a necessary condition for efficient turbulent calculations which require highly packed grids in the wall region.

A geometric grid in the normal direction is used in the actual code. Generation of this mesh requires the first grid spacing h_1, the geometric progression constant K, and the total number of points across the boundary layer J. The grid spacing is then defined as

$$h_j = K h_{j-1} \qquad j = 1, 2, 3, \ldots J . \tag{3.12a}$$

A convenient expression for the location of normal grid points is then

$$\eta_j = h_1 \left[\frac{K^j - 1}{K - 1} \right] . \tag{3.12b}$$

The grid spacing in the ξ direction is left as input.

With the grid defined at each mesh point. Considering an arbitrary flow quantity v, then the notation v_j^n defines v at mesh point (ξ_n, η_j). In addition in the sections that follow the notation for points and flow

quantities midway between grid points will be, (see fig.7)

$$\xi_{n-1/2} = \tfrac{1}{2}(\xi_n + \xi_{n-1}) \qquad \eta_{j-1/2} = \tfrac{1}{2}(\eta_j + \eta_{j-1}) \qquad (3.13a)$$

$$v_j^{n-1/2} = \tfrac{1}{2}(v_j^n + v_j^{n-1}) \qquad v_{j-1/2}^n = \tfrac{1}{2}(v_j^n + v_{j-1}^n) \qquad (3.13b)$$

In the next two sections the process of discretizing the governing equations will be discussed briefly. In this process each of the transformed equations is written as a system of first order equations through definition of some new flow quantities. The finite-difference expressions are then easily formulated in terms of flow quantities defined at the four corners of the sample mesh rectangle of fig.(7) using simple centered-difference quotients and midpoint definitions. The centering of the equation takes place at one of two points also shown in the figure. First each of the first order equations is centered at (ξ^n , $\eta_{j-1/2}$), then only those equations explicitly dependent on ξ the centering is moved to ($\xi^{n-1/2}$, $\eta_{j-1/2}$).

3.3 SOLUTION OF THE STREAMWISE EQUATION SET

The numerical solution of the streamwise equation set, equations (3.6) and (3.7), is accomplished by adding Coriolis acceleration terms into the two dimensional boundary layer scheme presented in some detail in Cebeci and Smith [17]. Instead of proceeding with a fully coupled solution of this set, the solution solves each equation independently, iterating between streamwise momentum equation and energy equation until a converged solution is reached. During the solution of the streamwise momentum equation g is held at it's previous value, which during solution of the energy equation f is taken as the last calculated value. This form of iterative solution is permissable since the two equations are not strongly coupled.

3.3.1 KELLER'S BOX SCHEME FOR STREAMWISE MOMENTUM EQUATION

Introducing two new functions, $U(\xi,\eta)$ and $V(\xi,\eta)$ the streamwise momentum equation (3.6) may be expressed as a system of first order equations.

$$f' = u \tag{3.14a}$$

$$u' = v \tag{3.14b}$$

$$[bv]' + fv + \beta[c - u^2] - D_1 w u = 2\xi\left[u\frac{\partial u}{\partial \xi} - v\frac{\partial f}{\partial \xi}\right] + E_1 \tag{3.14c}$$

Refering back to fig.(7) the equations are discretized by centering equations (3.14a) and (3.14b) at the midpoint of line segment $\overline{P_1 P_2}$, and equation (3.14c) at the mesh rectangle center. Centering yields the following set of finite-difference equations applying for $j = 1, 2, 3 \ldots J$:

$$f_j^n - f_{j-1}^n - h_j u_{j-1/2}^n = 0 \tag{3.15a}$$

$$u_j^n - u_{j-1}^n - h_j v_{j-1/2}^n = 0 \tag{3.15b}$$

$$(bv)_j^n - (bv)_{j-1}^n + h_j (1+\alpha_n)(fv)_{j-1/2}^n + h_j \beta_n c_{j-1/2}^n - h_j (\beta_n + \alpha_n)(u_{j-1/2}^n)^2$$
$$+ h_j \alpha_n (v_{j-1/2}^{n-1} f_{j-1/2}^n - f_{j-1/2}^{n-1} v_{j-1/2}^n) - (D_1)^n w_{j-1/2}^n u_{j-1/2}^n$$
$$= h_j S_{j-1/2}^{n-1} + 2 h_j (E_1)_{j-1/2}^{n-1/2} \tag{3.15c}$$

Where

$$\alpha_n = \frac{2 f^{n-1/2}}{b_n}$$

$$h_j S_{j-1/2}^{n-1} = (bv)_{j-1}^{n-1} - (bv)_j^{n-1} + h_j (\alpha_n + 1)(fv)_{j-1/2}^{n-1} - h_j \beta_{n-1} c_{j-1/2}^{n-1}$$
$$+ h_j (\beta_n - \alpha_n)(u_{j-1/2}^{n-1})^2 + (D_1)^{n-1} w_{j-1/2}^{n-1} u_{j-1/2}^{n-1}$$

The required boundary conditions are:

$$f_0^n = f_w^n \tag{3.16a}$$

$$u_0^n = 0 \tag{3.16b}$$

$$u_J^n = 1 \tag{3.16c}$$

To proceed with solution of this system of equations it is assumed that the complete solution is known at the $(n-1)$ station. The unknowns of this finite-difference system are (f_j^n, u_j^n, v_j^n) for $j = 0, 1, 2 \ldots J$.

A system of (3J) equations plus three boundary conditions in (3J + 3) unknowns. Unfortunately the system is still highly nonlinear.

Newton's Method is now used by introducing iterates $(f_j^{(i)}, u_j^{(i)}, v_j^{(i)})$ with initial values.

$$f_0^{(0)} = f_w \qquad u_0^{(0)} = 0 \qquad v_0^{(0)} = v_0^{n-1}$$

$$f_j^{(0)} = f_j^{n-1} \qquad u_j^{(0)} = u_j^{n-1} \qquad v_j^{(0)} = v_j^{n-1} \qquad j = 1, 2, 3 \ldots J-1$$

$$f_J^{(0)} = f_J^{n-1} \qquad u_J^{(0)} = 1 \qquad v_J^{(0)} = v_J^{n-1}$$

(NOTE: The superscript (o) for iterate count should not be confused with (n) which has been dropped from this point on, with no loss of clarity.)

The system of equations are now linearized by introduction of higher order iterates and dropping terms of order (δ^2).

$$f_j^{(i+1)} = f_j^{(i)} + \delta f_j^{(i)} \qquad u_j^{(i+1)} = u_j^{(i)} + \delta u_j^{(i)}$$

$$v_j^{(i+1)} = v_j^{(i)} + \delta v_j^{(i)}$$

Cebeci points out that linearization of the finite-difference equation done here, as opposed to linearization of differential equation before discretizing, can be far more accurate and efficient. It should also be pointed out that there are many possible ways of expressing the product terms linearly. In this light there is not one but many possible expressions for the final linearized set even if the procedure is strictly followed, but as Keller points out ref.[16] each possible form is equivalent and all have the same efficiency and convergence. The final

choice of form is based simply on ease of coding and personal preference. Carrying throught the linearization yields the following set of linear equations in ($\delta f_j^{(i)}$, $\delta u_j^{(i)}$, $\delta v_j^{(i)}$):

$$\delta f_j^{(i)} - \delta f_{j-1}^{(i)} - (h_j/2)(\delta u_j^{(i)} + \delta u_{j-1}^{(i)}) = r_j^{(i)} \qquad (3.17a)$$

$$\delta u_j^{(i)} - \delta u_{j-1}^{(i)} - (h_j/2)(\delta v_j^{(i)} + \delta v_{j-1}^{(i)}) = t_j^{(i)} \qquad (3.17b)$$

$$\theta_j^{(i)} \delta f_j^{(i)} + \phi_j^{(i)} \delta v_j^{(i)} + \psi_j^{(i)} \delta u_j^{(i)} - \bar{\theta}_j^{(i)} \delta f_{j-1}^{(i)} - \bar{\phi}_j^{(i)} \delta v_{j-1}^{(i)} - \bar{\psi}_j^{(i)} \delta u_{j-1}^{(i)} = s_j^{(i)} \qquad (3.17c)$$

for $j = 1, 2, 3 \ldots J$

where

$$\theta_j^{(i)} = h_j/2 \left[(1+\alpha_n) v_{j-1}^{(i)} + \alpha_n v_{j-1/2}^{n-1} \right] \qquad \bar{\theta}_j^{(i)} = -\theta_j^{(i)}$$

$$\psi_j^{(i)} = -h_j (\beta_n + \alpha_n) u_{j-1/2}^{(i)} - D_1 w_{j-1/2} \qquad \bar{\psi}_j^{(i)} = -\psi_j^{(i)}$$

$$\phi_j^{(i)} = b_j + (h_j/2)\left[(1+\alpha_n) f_{j-1/2}^{(i)} - \alpha_n f_{j-1/2}^{n-1} \right] \qquad \phi_j^{(i)} = 2 b_{j-1/2} - \phi_j^{(i)}$$

$$r_j^{(i)} = f_{j-1}^{(i)} - f_j^{(i)} + h_j u_{j-1/2}^{(i)}$$

$$t_j^{(i)} = u_{j-1}^{(i)} - u_j^{(i)} + h_j v_{j-1}^{(i)}$$

$$s_j^{(i)} = (bv)_{j-1}^{(i)} - (bv)_j^{(i)} - h_j (1+\alpha_n)(fv)_{j-1/2}^{(i)} + D_1 w_{j-1/2}$$
$$- h_j \alpha_n \left(v_{j-1/2}^{n-1} f_{j-1/2}^{(i)} f_{j-1/2}^{n-1} v_{j-1/2}^{(i)} \right) + h_j (\beta_n + \alpha_n)(u_{j-1/2}^{(i)})^2$$
$$- h_j \beta_n c_{j-1/2} + h_j S_{j-1/2}^{n-1} - 2 h_j (E_1)_{j-1/2}^{n-1/2}$$

The boundary conditions without iteration are:

$$\delta f_0^{(i)} = 0 \qquad \delta u_0^{(i)} = 0 \qquad \delta u_J^{(i)} = 0$$

$$i = 1, 2, 3 \ldots \infty \qquad \text{(3.18 a,b,c)}$$

The above system of equations are still implicit but can be easily rewritten in block tridiagonal form of (3 x 3) blocks which then may be solved by standard matrix factorization techniques.

In practice since the system when written in block tri-diagonal form contains a large number of zero block elements, the factorization is carried through by hand. This specializes the factorization scheme to a system of recurrence relations, reducing the number of machine operations required per iteration of Newton's method. This results in an extremely fast efficient code.

A final word on the convergence of Newton's method applied to the streamwise momentum equation. The convergence can be shown numerically to be nearly quadratic in nature. In effect this means well converged solutions require only 2-4 iterations.

3.3.2 KELLER'S BOX SCHEME FOR THE ENERGY EQUATION

The energy equation (3.7) is expressed as a first order system by defining the new function $G(\xi, \eta)$,

$$g' = G \qquad \text{(3.19a)}$$

$$[a_1 G + a_2 uv]' + fG - \beta^n u g = 2\xi\left[u\frac{\partial g}{\partial \xi} - G\frac{\partial f}{\partial \xi}\right] - E_2 \qquad (3.19b)$$

Then centering in the same manner as section 3.3.1 yields the following finite-difference equation set for j = 1,2,3...J:

$$g_j - g_{j-1} - h_j G_{j-1/2} = r_j \qquad (3.20a)$$

$$\theta_j g_j + \phi_j G_j - \bar{\theta}_j g_{j-1} - \bar{\phi} G_{j-1} = t_j \qquad (3.20b)$$

Where

$$\theta_j = -\alpha_n h_j u_{j-1/2}^{n-1/2}$$

$$\phi_j = (a_1)_j^n + (h_j/2)\left[f_{j-1/2} + \alpha_n (f_{j-1/2} - f_{j-1/2}^{n-1})\right]$$

$$\bar{\theta}_j = -\theta_j \qquad \bar{\phi}_j = -\phi_j$$

$$r_j = 0 \qquad t_j = S_{j-1/2}^{n-1} - 2h_j (E_2)_{j-1/2}^{n-1/2}$$

$$S_{j-1/2}^{n-1} = -\left[(a_1 G)_j^{n-1} - (a_1 G)_{j-1}^{n-1} + 2\left\{(a_2 uv)_j^{n-1/2} - (a_2 uv)_{j-1}^{n-1/2}\right\}\right.$$
$$+ h_j\left\{f_{j-1/2}^{n-1} + \alpha_n (f_{j-1/2}^{n} - f_{j-1/2}^{n-1})\right\} G_{j-1/2}^{n-1}$$
$$\left. + h_j\left\{-\beta^{n-1} u_{j-1/2}^{n-1} + 2\alpha_n u_{j-1/2}^{n-1/2}\right\} g_{j-1/2}^{n-1}\right]$$

In addition the boundary conditions on this set are:

$$g_0 = g_w \quad \text{OR} \quad G_0 = g'_w \qquad (3.21a)$$

$$g_J = 1 \qquad (3.21b)$$

In the case of the energy equation, the finite-difference equation set is already linear in g and G. It can therefore be immediately expressed in block tri-diagonal

form of 2 x 2 blocks. The factorization is also carried through to reduce the system to the efficient set of recursions.

3.3.3 SUMMARY OF STREAMWISE EQUATION SET SOLUTION SCHEME

The solution scheme presented constitutes the standard two-dimensional laminar/turbulent compressible boundary layer solution developed by Keller and Cebeci if the Coriolis acceleration terms are dropped, by setting D_1, E_1 and E_2 to zero. With these terms the solution is the first approximation to the solution of the streamwise equation set. A general flow chart of this solution is shown in fig.(8). Starting with a known solution at station ξ^{n-1}, all flow quantities for the current station are intitialized to the previous station values. The force terms are calculated. The eddy viscosity and fluid properties are calculated. Iteration of the streamwise momentum equation proceeds until convergence. Then the energy equation is solved. At this point the eddy viscosity and fluid properties are recalculated. The momentum and energy equation are solved. Convergence of the complete streamwise equation set is based on the total change in wall shear between loops. When this drops below a certain value the solution proceeds to either the next station in the two dimensional case or the crossflow equation

solution in the small crossflow equation set.

3.4 SOLUTION OF THE CROSSFLOW EQUATION

Once f and U are known the crossflow equation becomes an ordinary differential equation. Keller's box scheme is efficiently used in a solution which is very similar to the solution of the energy equation of section 3.3.2. Introducing a new function $W(\xi, \eta)$, equation (3.8) is expressed as a system of first order equations:

$$w' = W \tag{3.22a}$$

$$[bW]' + fW - \beta u w = 2\xi\left[u\frac{\partial w}{\partial \xi} - W\frac{\partial f}{\partial \xi}\right] + E_3 \tag{3.22b}$$

where w and W are unknown. Refering to fig.(7) the equations are centered appropriately on the mesh rectangle to yield the finite-difference expression of the crossflow equation for $j = 1, 2, 3 \ldots J$

$$w_j - w_{j-1} - h_j W_{j-1/2} = r_j \tag{3.23a}$$

$$\theta_j w_j + \phi_j W_j - \bar{\theta}_j w_{j-1} - \bar{\phi}_j W_j = t_j \tag{3.23b}$$

Where

$$\theta_j = -(h_j/2)\left[2\alpha_n u_{j-1/2}^{n-1/2} + \beta_n u_{j-1/2}\right]$$

$$\phi_j = b_j + (h_j/2)\left[(1+\alpha_n) f_{j-1/2} - \alpha_n f_{j-1/2}^{n-1}\right]$$

$$\bar{\theta}_j = -\theta_j \qquad \bar{\phi}_j = 2b_{j-1/2} - \phi_j$$

$$r_j = 0$$

$$t_j = S_{j-1/2}^{n-1} - 2h_j (E_3)_{j-1/2}^{n-1/2}$$

$$S_{j-1/2}^{n-1} = (bw)_j^{n-1} - (b_j w)_{j-1}^{n-1} - h_j[(1+\alpha_n) f_{j-1/2}^{n-1} + \alpha_n f_{j-1/2}] W_{j-1/2}^{n-1} + h_j [\beta_{n-1} u_{j-1/2}^{n-1} - 2\alpha_n u_{j-1/2}^{n-1/2}] w_{j-1/2}^{n-1}$$

In addition the boundary conditions are:

$$w_0 = 0 \tag{3.24a}$$

$$w_J = 0 \tag{3.24b}$$

This linear system of (2J) equations plus two boundary conditions in (2J + 2) unknowns can be expressed in standard block tri-diagonal matrix of (2x2) blocks. The solution of w_j and W_j is then found through block factorization, similar to the energy equation, and expressed finally in the form of recursion relations.

3.5 SUMMARY OF COMPLETE SMALL CROSSFLOW SOLUTION SCHEME

Beginning with a known solution at station $(n-1)$ the complete solution of the small crossflow equations is shown in fig.(9). All flow quantities for the current station are intitialized to the previous station. The fluid properties, eddy viscosity, and Coriolis forces are calculated. Then as described in section 3.3.3 the streamwise equation is solved completing one iteration of the total solution. From this point the fluid properties are calculated, streamwise equation set solved, and crossflow equation solved. This last sweep is repeated until convergence of the total equation set is found. As with the other loops convergence is set on the overall change in wall shear following below some set level. After convergence the solution scheme proceeds to the next station.

3.6 GENERATION OF STARTING SOLUTION

As previously mentioned the coordinate scalings were chosen to remove the singularity at $\xi = 0$. There then exists the possibility of generating a similarity or in particular a stagnation point solution to the governing equations. Care was taken in the formulation of the finite-difference equation form so those terms with ξ dependence could easily be dropped, providing the governing equations for a stagnation point solution. If reference is made to equations (3.6),(3.7),(3.8), when the ξ dependence is removed the solution reduces to a flat plate stagnation point equation set.

In the finite-difference equations the ξ dependence is removed by setting α_n and $S_{j-1/2}^{n-1}$ equal to zero. It should also be noted that the force terms are also zero since D_1 through D_4 are zero. Finally the leading edge flow is laminar so $\varepsilon_m^+ = 0$. With the force terms being zero the only solution of the crossflow equation is the crossflow velocity is identically zero. Only the streamwise equation set remains to be solved. Since it is in a linearized form an initial guess for the velocity and enthalpy profiles must be provided to start the solution. There are an infinite number of possible guesses, the only requirement being the profiles must be consistent.

In the present code a linear velocity profile satisfying the boundary conditions is used:

$$f^{(o)} = \eta^2/2\eta_\infty \qquad u^{(o)} = \eta/\eta_\infty$$

$$v^{(o)} = 1/\eta_\infty \qquad (3.25\ a,b,c)$$

The static enthalpy profile for adiabatic flows is determined by $h = H_e - \frac{1}{2} u^2 u_{1e}^2$ (3.26)

For those cases with specified wall temperature

$$g = g_w + (g_w - 1)\,\eta/\eta_\infty\,(\eta/\eta_\infty - 2)$$

is convenient. (3.27)

With these intial profiles the starting solution is generated as shown in fig.(10).

4.0 TWO DIMENSIONAL TEST CASES

Throughout the formulation of the numerical solution of the small crossflow equations, care was taken to provide for calculation of standard two dimensional laminar/turbulent compressible boundary layers. In fact the small crossflow solution scheme is really an extension of the basic two dimensional calculations. It is therefore of value to show, if only briefly, the kind of accuracy that can be obtained by the two dimensional calculation.

The first case considered is for laminar compressible flow over a flat plate for varying temperature ratio's and Mach numbers. Table (4.1) compares the present computed value of the average skin-friction coefficient with those computed by Cebeci, by Smith and Clutter, and by Van Driest as presented in Cebeci and Smith [19]. The actual form presented is $\bar{c}_f R_{e_x}$ where the average skin friction coefficient $\bar{c}_f$ is defined in terms of the local coefficient c_f by the following,

$$\bar{c}_f = \left(\int_0^{R_{e_x}} c_f \, d R_{e_x} \right) \Big/ R_{e_x} \tag{4.1}$$

The table shows that even for extremely coarse grids one can expect good results over a wide range of Mach numbers and temperature ratio T_e/T_w. The calculations here were done for $h_1 = .4$ at constant spacing to $\eta_\infty = 6.0$ and also for a geometric grid of $h_1 = 0.001$, $K = 1.2$ and $\eta_\infty = 6.0$.

Table 4.1

Summary of Skin Friction Coefficients for Laminar Compressible Flate Plate Flow

M_e	$\frac{T_w}{T_e}$	$N(h_1)$		N	Smith-Clotter	Van Driest
		Present	Cebeci	Variable Grid Present		
0.01	0.25	1.3632	1.3613	1.3662	1.366	1.356
0.01	1.00	1.3325	1.3324	1.3348	1.328	1.328
0.01	2.00	1.2753	1.2761	1.2767	1.270	1.268
0.01	adiab.	1.3325	1.3324	1.3348	1.328	1.328
6.00	0.25	1.2522	0.4458	1.2543	1.228	1.250
6.00	1.00	1.2164	0.4320	1.2171	1.191	1.215
6.00	2.00	1.1746	0.4912	1.1746	1.150	1.168
6.00	adiab.		0.7004	1.0368	1.015	1.028

Note: Pr=0.75 h_1=0.2 η_∞=6.0 N= $\bar{C}_f \, Re_x^{1/2}$

Cebeci has tested this numerical scheme for turbulent compressible boundary layer calculations with heat and mass transfer for a wide range of Mach numbers. A small portion of these cases are presented in ref.[20], where it is noted that a majority of available experimental data is restricted to zero pressure gradient flow. The following are a few simple cases to illustrate the performance of the two dimensional turbulence model and complete numerical scheme. Each of these cases was run by starting with a compressible laminar solution at $X_1 = 0$ and then specifying full turbulence at the next station, X = 0.001 ft. . The computation then proceeds downstream until the experimental R_{θ} or R_{e_x} is reached.

The first case of an adiabatic flat plate is shown in fig.(11) in the form of Mach number and velocity profiles. The experimental data is by Coles for $M_e = 1.982$ and $R_{\theta} = 8570$. The skin friction was measured by floating element to be $C_{f_{exp}} = 0.00202$ compared to a calculated value of $C_{f_{cal}} = 0.001988$ showing good agreement.

A second example for the adiabatic flat plate performed by Matting for $M_e = 2.95$ and $R_{e_x} = 31 \times 10^6$ is shown in fig.(12). The skin friction measured by floating element was $C_{f_{exp}} = 0.00129$ compared to a computed value of $C_{f_{cal}} = 0.00132$.

5.0 SMALL CROSSFLOW CALCULATION TEST CASES

Unfortunately at this time there exists very little experimental data or even numerical solutions for three dimensional boundary layers on general rotating blades. This is the direct result of the extreme difficulty of making experimental boundary layer measurements on rotating blades and, since these boundary layers are three dimensional, the governing equations are so complex exact solutions are rare.

There have been two cases for which the solution of three dimensional boundary layers on rotating blades have been found. Both cases are for simpler laminar incompressible boundary layers on zero thickness unloaded blades for which similarity type or series type solutions exist. Since the code used is for compressible flow the Mach number was chosen in these cases as much less than 1.0 so compressibility no longer effects the solutions.

5.1 FOGARTY SOLUTION FOR FLAT PLATE BLADE

The first case is for a rotating flat plate of chord c, as shown in fig.(13). Fogarty, ref.[1], was able to find a similarity type solution for the small crossflow equations in laminar incompressible form which applies for large R/c stations far out from hub on the blade. The invisid flow field for this case in terms of intrinsic coordinate system is

$$u_{1e} = \omega R \qquad u_{2e} = 0 \,. \tag{5.1}$$

where the streamlines or lines of constant X_2 are circular arcs of radius R. This case is important since the three dimensionality of the flow is the result of the centrifugal force due to rotation. Fogarty presented the solution of this flow for the limiting case of $R \gg X_1$, or the angle $\theta = x_1/R$ as $\theta \to 0$. This limiting case is presented in the similarity form found by Fogarty, fig.(14), ETA is a dimensionless distance from the plate defined as

$$\text{ETA} = x_3 \left(\rho_e u_{1e} / \mu_e x_1\right)^{1/2}$$

the U_1 and U_2 velocities are also scaled as

$$u_1/u_{1e}\cos\theta \quad \text{AND} \quad u_2/u_{1e}\sin\theta \,. \tag{5.2a,b}$$

The agreement is very good.

This case also illustrates the importance of the curvature term containing K_1. Here $K_1 = 1/R$, R being the

perpendicular distance from the axis of rotation, would appear to be unimportant for the case of $R >> X_1$, but since all the terms in the crossflow momentum equation are $O(c/R)$ this term is not negligible. This becomes obvious when the term is dropped as shown in fig.(15). Without the term the solution is nearly three times what it should be. The effect of this curvature is often important in predicting correct crossflows since, even though the radius of curvature is large, relative to other terms in the crossflow momentum equation it cannot be dropped.

5.2 NON-LOADED HELICAL BLADE IN A UNIFORM STREAM

Miyake and Fujita, ref.[3], were able to generate three dimensional laminar incompressible boundary layer solutions for non-loaded helical blades in a uniform stream as shown in fig.(16). This is an outstanding accomplishment since the solutions were found using a perturbation technique to obtain a series solution composed of two groups of similar functions. This case is important since the three dimensionality of the boundary layer is the result of both centrifugal forces and also the twist of the blade which generate Coriolis forces.

The test case is for a uniform upstream velocity u_{FS}, with a blade rotating at angular velocity ω. The blade, as shown in fig.(16), is twisted with the center of twist at the blade leading edge, so the angle of attack becomes zero all along the leading edge. The blade is assumed infinitely long with the effect of the hub and tip casing not taken into account. The equations that describe the surface are

$$\xi_1 = r\cos\phi \tag{5.3a}$$

$$\xi_2 = r\sin\phi \tag{5.3b}$$

$$\xi_3 = z \tag{5.3c}$$

$$\tan\phi = u_{FS}/\omega z \tag{5.3d}$$

The invisid streamlines for this case are the intersection of the blade surface and circular cylinders whose center

is the ξ_2 axis as determined by the following equation set:

$$\xi_1 = x \cos\phi \tag{5.4a}$$

$$\xi_2 = x \sin\phi \tag{5.4b}$$

$$\xi_3 = z \tag{5.4c}$$

$$(\xi_1)^2 + (\xi_3)^2 = R \tag{5.4d}$$

$$\tan\phi = u_{FS}/\omega z \tag{5.4e}$$

Finally along a given streamline defined by a given R the invisid velocity is

$$u_{1e} = \left[u_{FS}^2 + (\omega R)^2 \right]^{1/2} \tag{5.5}$$

Figure (17a & b) compare streamwise and crossflow boundary layer profiles with those generated by Miyake and Fujita. The profiles are both on the same streamline defined by leading edge angle $\phi_o = \tan^{-1}(0.2)$, fig.(17a) for $\frac{x_1}{R} = 0.2$ and fig.(17b) for $\frac{x_1}{R} = 0.3$ (Recall, X_1 is the distance down the streamline from the leading edge and R is the radius of the streamline). The computational results prove to be in very good agreement with those computed by Miyake and Fujita.

To illustrate the development of streamwise and crossflow velocity profiles, fig.(18), presents the velocity profiles for three stations down the streamline. It is interesting to note that the first station, $\frac{x_1}{R} = 0$, corresponds to Blasius flow (Blasius streamwise profile and zero crossflow).

In the limits as R goes to infinity or more correctly as ϕ_o goes to zero this solution goes to the boundary

layer solution described in section 5.2 of the rotating flat plate blade. The effect of the curvature term containing K_1, although not as simple as the case in section 5.2 is equally important for all helical blade calculations.

6.0 TRANSONIC COMPRESSOR BLADE

Presented in this chapter are some computed boundary layer results for a NASA low-aspect-ratio rotor blade. This blade [see fig.(19)] is used in the first stage of a NASA two-stage transonic compressor, designed for the energy efficiency engine program. The blade sections shown previously in fig.(4) were taken from this blade. The invisid input data was calculated by the invisid solution by Thompkins [10]. In addition to the well defined invisid data, a large amount of time and space resolved experimental measurements behind the rotor have been completed for this compressor in the MIT Blowdown Compressor Facility. These experimental measurements, though useful in giving blade wake information, are not suitable for direct comparisons to the boundary layer data presented here since the boundary layer is no longer attached to the blade.

The boundary layer development on both pressure and suction sides of this blade were calculated using the small crossflow solution. The invisid pressure distributions are presented in fig.(20) for the pressure side and fig.(21) for the suction side. The corresponding edge Mach number distribution for pressure and suction side in fig.(22) and (23) respectively. It has been assumed that for the Mach numbers shown the boundary layer will be turbulent over a majority of the blade. Since very little is

known about the transition to turbulence on blades of this type no attempt has been made to correctly model the region of transition. Instead the turbulence has been defined by the three dimensional model of equation set (2.42) and (2.43) assuming the flow to by fully turbulent at the first point off the leading edge of the blade.

The small crossflow boundary layer solution along each of the streamlines shown in fig.(24) for the pressure side and fig.(25) for the suction side was calculated using the solution scheme described in section (3.5). The streamlines shown are numbered from 2 at the hub through 17 at the tip region. The boundary layer solution was calculated at 21 stations down each streamline. In the figures which follow N = 1 corresponds to the leading edge solution while N = 21 corresponds to the trailing edge. The following selected set of streamlines have been chosen from the complete set of 16 streamlines since they characterize the flow on both surfaces of the blade: streamlines 2 and 3 in the hub region, streamlines 9 and 10 near midspan, and streamlines 16 and 17 in the tip region. The small crossflow solution along these streamlines is presented in the form of streamwise velocity profiles down each streamline, figures (26) through (37), and crossflow velocity profiles down each streamline, figures (38) through (49), where the velocities in each figure have been scaled in terms of the

local invisid edge velocity u_{ie}. ETA is a scaled normal distance defined by equation (3.16).

6.1 DEVELOPMENT OF STREAMWISE VELOCITY PROFILES

In general it was found that while the pressure side boundary layer remains attached (a requirement for a numerical solution to be found) the suction side separated somewhere between station N = 14 and N = 18 on each of the 16 streamlines. In this sense figures (26) and (27) are typical of the turbulent boundary layers calculated on the pressure and suction side of the blade. These two pictures very clearly illustrate the large effect of turbulence on the profile shape as the solution marches from the laminar similarity solution generated at station 1. The turbulence causes a rapid thickening of the boundary layer with a greatly increased wall shear the result of entrainment of high energy fluid into the wall region. This entrainment of fluid greatly increases the boundary layers resistance to separation allowing attached flow to exist in much higher adverse pressure gradient regions than possible for laminar flow. The solution failed to converge at station N = 18 which implies separation occurs somewhere between station 17 and station 18. The onset of separation is not obvious from the last profile, station 17. Although no attempt has been made to resolve this region, it is possible to do so by simply decreasing the step size in X_1 until solution can be calculated. In this manner, if desired, the separation onset can be

resolved. Some insight in the cause of this separation can be found by refering back to the pressure distribution of fig.(21). In the figure the concentration of pressure contours along the aft portion of the blade indicate a strong adverse pressure gradient. In the hub region this adverse pressure gradient exists over nearly half the blade. Although not exceedingly large here the adverse gradient does exist for some distance down the streamline suggesting the possiblility of separation which does infact occur at station N = 18. As this adverse pressure gradient region is followed from hub to tip it should be noted that the region becomes much smaller while the gradient grows stronger leading finally to a shock in the tip region. As expected the separation found on each suction side streamline occurs in the growing adverse pressure gradient region. The streamwise velocity profiles of the next streamline (streamline 3) are shown in figures (28) and (29), pressure side and suction side respectively. These figures are similar in nature to those of streamline 2.

Proceeding to the midspan streamlines 9 and 10, figures (30) and (32) show a drop in the wall shear between stations 10 and 14 on the pressure side caused by an increasing adverse pressure gradient in this region. Refering to the pressure side pressure distribution figure (20), this adverse pressure gradient develops into

a weak shock as the tip region is approached. Figures (31) and (33) clearly indicate the onset of separation on the suction side near station 17. It is interesting to note that reverse flow is actually calculated in fig.(31) near the wall.

Finally typical streamwise velocity profiles in the tip region of the blade are presented in figures (34), (35), (36), and (37). In this region the weak shock on the pressure side imposes an adverse pressure gradient that nearly separates the streamwise velocity profiles as in fig. (34) and (36); but since, the flow is turbulent it does not separate and the boundary layer profiles soon return to their previous form. The suction side, figures (35) and (37), show separation similar to the other streamlines shown.

6.2 DEVELOPMENT OF CROSSFLOW VELOCITY PROFILE

Before discussing the particular profiles calculated for this blade it is helpful to consider the centrifugal and Coriolis force terms which cause these crossflows. In vector form they are

$$\text{Centrifugal force} = -\rho\,\vec{\Omega}\times(\vec{\Omega}\times\vec{R}) \tag{6.1}$$

$$\text{Coriolis force} = -\rho\,(\vec{\Omega}\times\vec{u}) \tag{6.2}$$

The direction of the centrifugal force is always radially outward which tend to cause positive crossflows. In contrast the radial component of the Coriolis force can be either positive (outward) or negative depending on whether the flow velocity component in the theta direction relative to the blade is positive or negative. If the theta velocity component is negative, which is the general case, the radial component of the Coriolis force is positive or radially outward. Negative crossflows are possible when this force component changes sign caused by a change of sign of the theta velocity component. In general for most points on the blade the total radial force is positive driving the crossflows radially outward.

If we now consider the crossflow profiles presented in figures (38) and (39) for the pressure and suction sides of streamline number 2, while the crossflow

velocities initially grow as expected, near the trailing edge the profile is driven back to zero. This reduction of the crossflow velocity is the direct result of the negative Coriolis term in the trailing edge region as discussed above. This same effect is visible in figures (40) and (41) for streamline 3 to a lesser degree. These two streamlines are important in that they clearly illustrate that the Coriolis forces can and do cause negative crossflows in certain regions of blades. It must be kept in mind that since these two streamlines are near the rotor hub, an area where the small crossflow approximation has questionable validity, the results are more important in an instructive sense then for correctly predicting the flow.

As we move farther from the hub the small crossflow approximation becomes more accurate. The profiles for streamlines 9 and 10, shown in figure (42), (43), (44), and (45) are representative of the true crossflow profiles of this region of the blade. These figures show that for both the pressure and suction sides of the blade the boundary layers are far from being two dimensional. Since over the length of the streamline both centrifugal and Coriolis forces are positive the crossflow velocities grow down the length of the streamline.

The crossflow profiles in the tip region of the

blade are shown in figures (46), (47), (48) and (49). As with those profiles in the midspan region the crossflows in the tip region grow to very large values. Since in this region the boundary layer is likely to be dominated by the influences of the tip casing these profiles must be interpreted with caution.

6.3 RADIAL CONVECTION OF LOSSES

Experimental measurements of the flow behind the NASA low-aspect-ratio rotor have been performed in the MIT Blowdown Facility and evaluated by Ng ref.[21]. A plot of measured compressor efficiently as a function of radius, see fig. (50), shows very low efficiencies in the tip region of the blade. This drop in efficiency has been found to be common in almost all compressor designs to date. These high losses are not predicted by present invisid compressor solutions which suggested the cause is related to the blade boundary layer which is not accounted for in the invisid calculation. One possible conclusion is that the radial flow within the boundary layer is convecting low energy fluid into the tip region where it mixes out with the invisid flow to cause the high loss region. Although the small crossflow solution is not accurate in the tip region it does provide an indication of the radial flows possible. As a first approximation of the convected flow into the tip region the crossflow velocity across the streamline 17 on both pressure and suction side is integrated across the boundary down each streamline. Even though large turning takes place in this region the total radial flow in the boundary is a surprising small 0.03% of the total massflow through the stage. Assuming this low energy fluid is then mixed

out in the outer 30% of the flow, the total flow of the tip region, the total pressure loss maybe estimated using Influence Coefficients as described in Shapiro ref.[22]. Since the percentage of mixed fluid is so small a total pressure loss of 0.09% is as expected. Even if this result is off by an order of magnitude the loss is still insignificant compared to those measured. The convected losses are not the source of low efficiency. It appears that a significant tip pressure loss can be generated by convection of low energy fluid only when the flow separates.

7.0 SUMMARY

The small crossflow laminar/turbulent boundary layer solution which has been presented provides insight into the nature of boundary layers on rotating blades. Extreme care must be taken in interpreting these solutions, particularly in the hub and tip regions of the blade, since the small crossflow approximation is not as stronge as the standard boundary layer approximations. The flows are clearly three dimensional in nature which explains the failure of past attempts to predict separation and losses using standard two dimensional airfoil boundary layer calculations.

The incompressible test cases presented in section 5, are of value since they illustrate the effect of Coriolis forces on the boundary layer. These forces in the helical blade case actually strengthen the boundary layer resistance to separation. The same effect can be expected for transonic compressor blades, although for the NASA low-aspect-ratio blade of section 6.0 this effect is hidden by the large influence of turbulence on the profile development. It has also been found that when the intrinsic coordinate system is used the curvature term containing K_1 is important for prediction of a correct solution.

Although the modeling of turbulence is not emphasized in this thesis the difference between use of a two dimensional or three dimensional model has a profound effect on the resulting solution. This follows from the fact that the crossflow velocity, which cannot be neglected, plays an important part in the prediction of correct turbulence levels.

Finally it should be noted that prediction of sizable crossflow velocities for the NASA low-aspect-ratio rotor means very large turning of the flow from the invisid streamline direction takes place in the wall region of the boundary layer. This occurs over a majority of the blade, but since the overall boundary layer thickness remains relatively small, the net radial flow within the boundary layer is small. This suggests that losses cannot be convected into the tip region of the blade from other sections by the radial flow in the boundary layer.

The results of this solution scheme show that to accurately predict transonic compressor blade boundary layers in the future will require a full three dimensional solution scheme. Implementation of such a scheme is dependent on the accurate definition of the flow in the hub and tip regions, which is not possible at this time. A large amount of work is also needed in the area of turbulence modeling for internal flows. In parallel with

this effort must come advances in experimental techniques to measure the flow within blade passages so numerical schemes may be evaluated.

For the present time there exists the possibility of extending our understanding of these flow by attempting an interaction scheme between the small crossflow solution and the invisid solution.

If the difficulties in full three dimensional boundary layer calculations cannot be overcome, the application of thin shear layer calculations, where the entire flow field is solved directly, may be possible.

REFERENCES

[1] L.E. Fogarty, "The Laminar Boundary Layer On a Rotating Blade," Journal of Aeronautical Sciences, Vol. 18 No. 4, April 1951, pp. 247-252.

[2] H.S. Tan, "On Laminar Boundary Layer Over a Rotating Blade," Journal of Aeronautical Sciences, Vol. 20, July 1953, pp. 780-781.

[3] Y. Miyake and S. Fujita, "A Laminar Boundary Layer on a Rotating Three-Dimensional Blade," Journal of Fluid Mechanics, Vol. 65, Part 3, 1974, pp. 481-498.

[4] J. H. Horlock and J. Wordsworth, " The Three-Dimensional Laminar Boundary Layer on a Rotating Helical Blade," Journal of Fluid Mechanics, Vol. 23, Part 2, 1965, pp. 305-314.

[5] T. Cebeci, K. Kaups, and J.A. Ramsey, "A General Method for Calculating Three-Dimensional Compressible Laminar and Turbulent Boundary Layers on Arbitrary Wings," NASA CR-2777, 1977.

[6] A. Mager, "Three-Dimensional Laminar Boundary Layers," High Speed Aerodynamics and Jet Propulsion, Vol. 4, Theory of Laminar Flows, Section C, Princeton University Press, New Jersey, 1964, pp. 286-394.

[7] A. D. Michal, "Matrix and Tensor Calculus," Wiley, 1947, pp. 103,121.

[8] L. Howarth, "The Boundary Layer in Three-Dimensional Flow, Part I," Phil. Mag., Vol. 42, 1951, pp. 239-243.

[9] C.W. Kitchens, Jr, R. Sedney, and N. Gerber, "The Role of Zone of Dependence Concept in Three-Dimensional Boundary-Layer Calculations," AIAA 2nd Computational Fluid Dynamics Conference Proceeding, Hartford, Ct., June 1975, pp.102-112.

[10] G. Haymann-Haber and W.T. Thompkins Jr., "Comparison of Experemental and Computational Shock Structure in a Transonic Compressor Rotor," Trans. ASME Journal of Engineering for Power, Paper No. 80-GT-81, December 1979.

[11] H. Schlichting, "Boundary-Layer Theory," McGraw-Hill Book Company, New York, 6th Edition, 1968, pp.312-313.

[12] T. Cebeci and A.M.O. Smith, "Analysis of Turbulent Boundary Layers," Academic Press, New York, 1974, pp. 211-257.

[13] G. L. Mellor and H.J. Herring, "Simple Eddy Viscosity Relations for Three-Dimensional Turbulent Boundary Layers," AIAA Journal, Vol. 15 No. 6, June 1977.

[14] H. B. Keller and T. Cebeci, " Accurate Numerical Methods for Boundary-Layer Flows-I. Two-Dimensional Laminar flows," Lecture Notes in Physics, Vol. 8, Proceedings of the Second International Conference on Numerical Methods in Fluid Dynamics, 1971.

[15] H. B. Keller and T. Cebeci, "Accurate Numerical Methods for Boundary-Layer Flows-II. Two Dimensional Turbulent Flows," AIAA Journal, Vol. 10, September 1972, pp. 1193-1199.

[16] H. B. Keller, "Some Computational Problems in Boundary-Layer Flows," Lecture Notes in Physics, Vol. 35, Proceedings of the Fourth International Conference on Numerical Methods in Fluid Dynamics, June 1974, pp. 1-21.

[17] T. Cebeci and A.M.O. Smith, "Analysis of Turbulent Boundary Layers," Academic Press, New York, 1974, pp. 258-297.

[18] W. D. Hayes and R. F. Probstein, "Hypersonic Flow Theory," Academic Press, New York, 1959.

[19] T. Cebeci and A. M. O. Smith, "Analysis of Turbulent Boundary Layers," Academic Press, New York, 1974, pp. 327-328.

[20] T. Cebeci and A. M. O. Smith, "Analysis of Turbulent Boundary Layers," Academic Press, New York, 1974, pp. 359-361

[21] W. F. Ng, "Detailed Time Resolved Measurements and Analysis of Unsteady Flow in a Transonic Compressor," M.S. Thesis, MIT, September 1980.

[22] A. H. Shapiro, "The Dynamics and Thermodynamics of Compressible Fluid Flow," Vol. 1, John Wiley & Sons, Inc., New York, 1953, pp. 230-232.

Appendix I: NON-DIMENSIONALIZATION OF THE GOVERNING EQUATIONS

The following non-dimensionalization is done only as a matter of convenience to eliminate many of the problems associated with formulating a dimensionally consistent set of input. Of the many forms of non-dimensionalization possible, the scheme used here was chosen since it is the same as used in the invisid solution of Thompkins. No data transformation is then required when inputing the invisid compressor solutions. The non-dimensionalization is done in terms of the five stagnation reference properties, r_0, ρ_0, μ_0, a_0, and T_0. Where $a_0=\sqrt{\gamma R T_0}$. Taking barred properties as dimensional, the following non-dimensional properties are defined,

$$u_1 = \bar{u}_1/a_0 \qquad u_2 = \bar{u}_2/a_0 \qquad u_3 = \frac{\bar{u}_3}{a_0}\sqrt{Re_0}$$

$$x_1 = \bar{x}_1/r_0 \qquad x_2 = \bar{x}_2/r_0 \qquad x_3 = \frac{\bar{x}_3}{r_0}\sqrt{Re_0}$$

$$\mu = \bar{\mu}/\mu_0 \qquad H = \bar{H}/a_0^2 \qquad \varepsilon_m = \frac{\bar{\varepsilon}_m \rho_0}{\mu_0}$$

$$T = \bar{T}/T_0 \qquad \rho = \bar{\rho}/\rho_0 \qquad P = \bar{P}/\rho_0 a_0^2$$

Where $$Re_0 = \frac{\rho_0 a_0 r_0}{\mu_0} \quad .$$

U_3 and X_3 have been scaled by the square root of the reference Reynolds number so the resulting non-dimensional equations have the same form as the dimensional equations. The resulting transformed equations are listed in section 2.7.

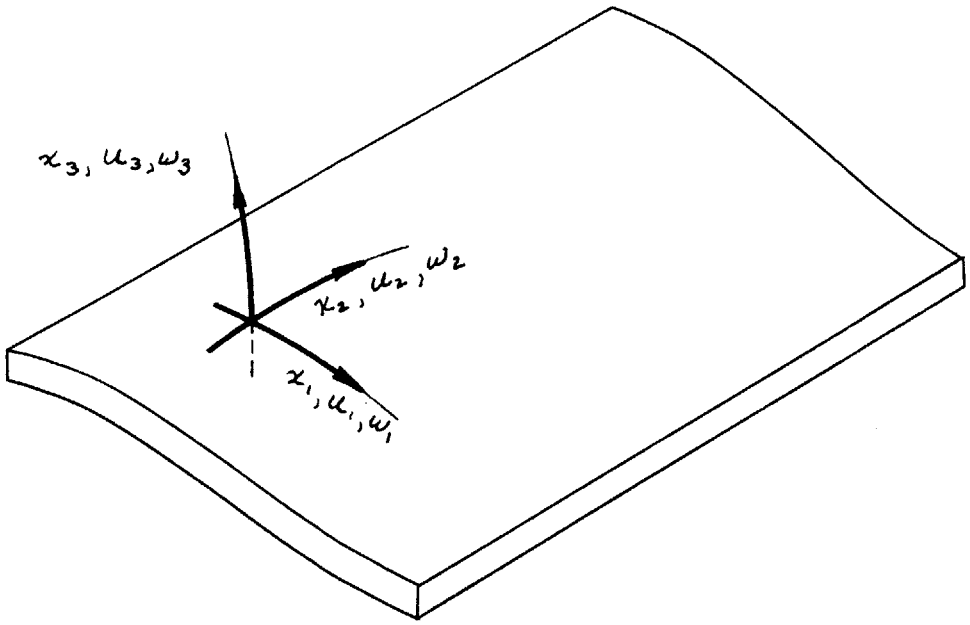

Figure 1. Orthogonal curvalinear coordinate system.

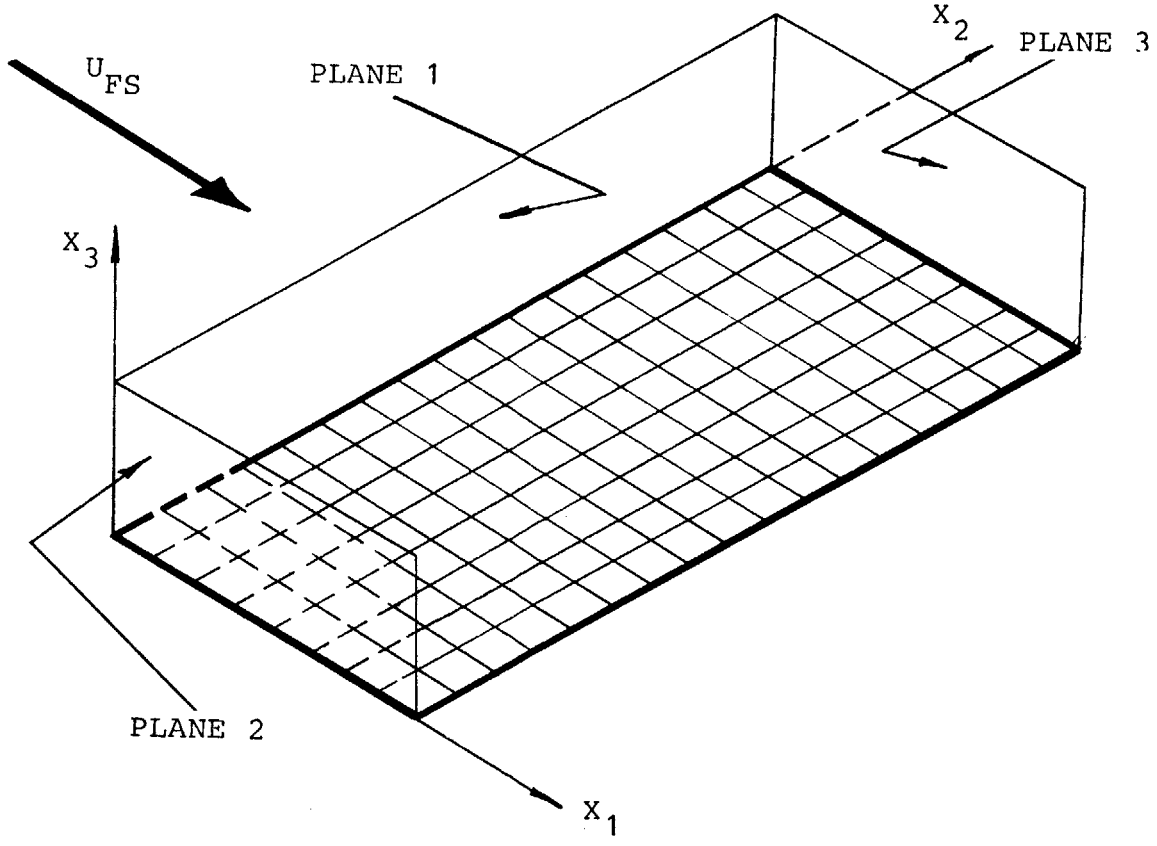

Figure 2. Simple flat plate blade showing three required initial planes of data.

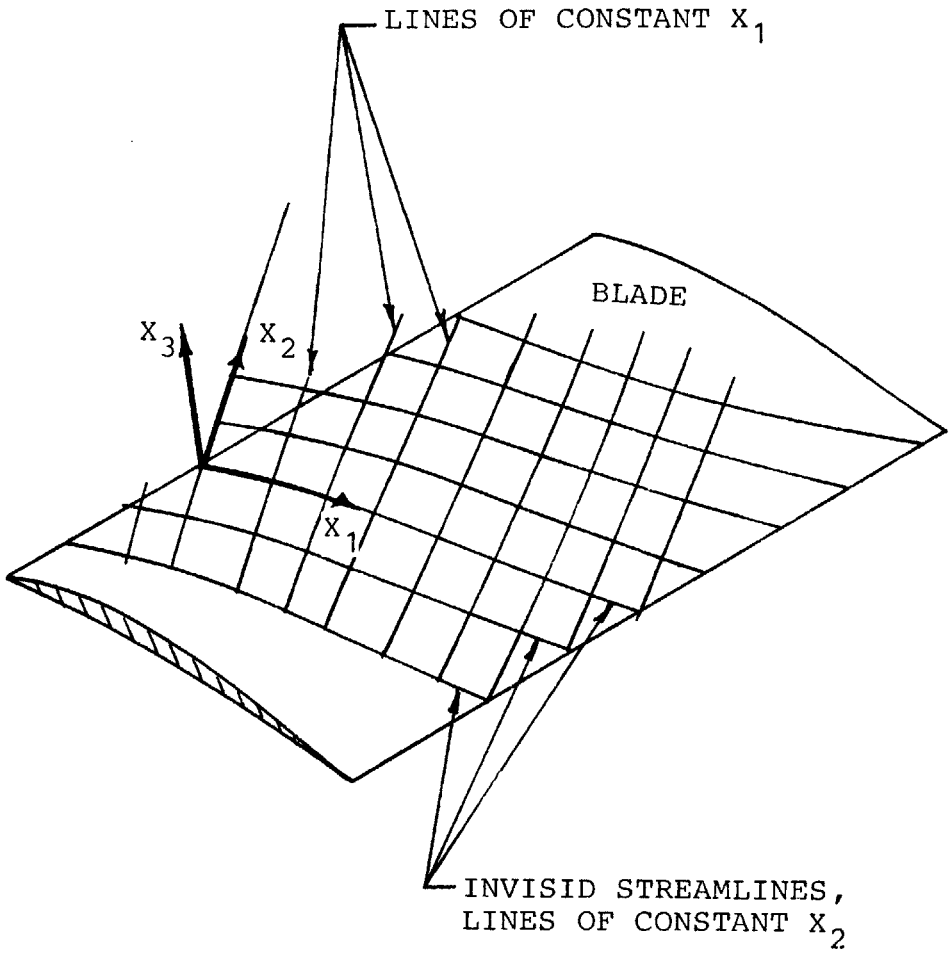

Figure 3. Intrinsic coordinate system.

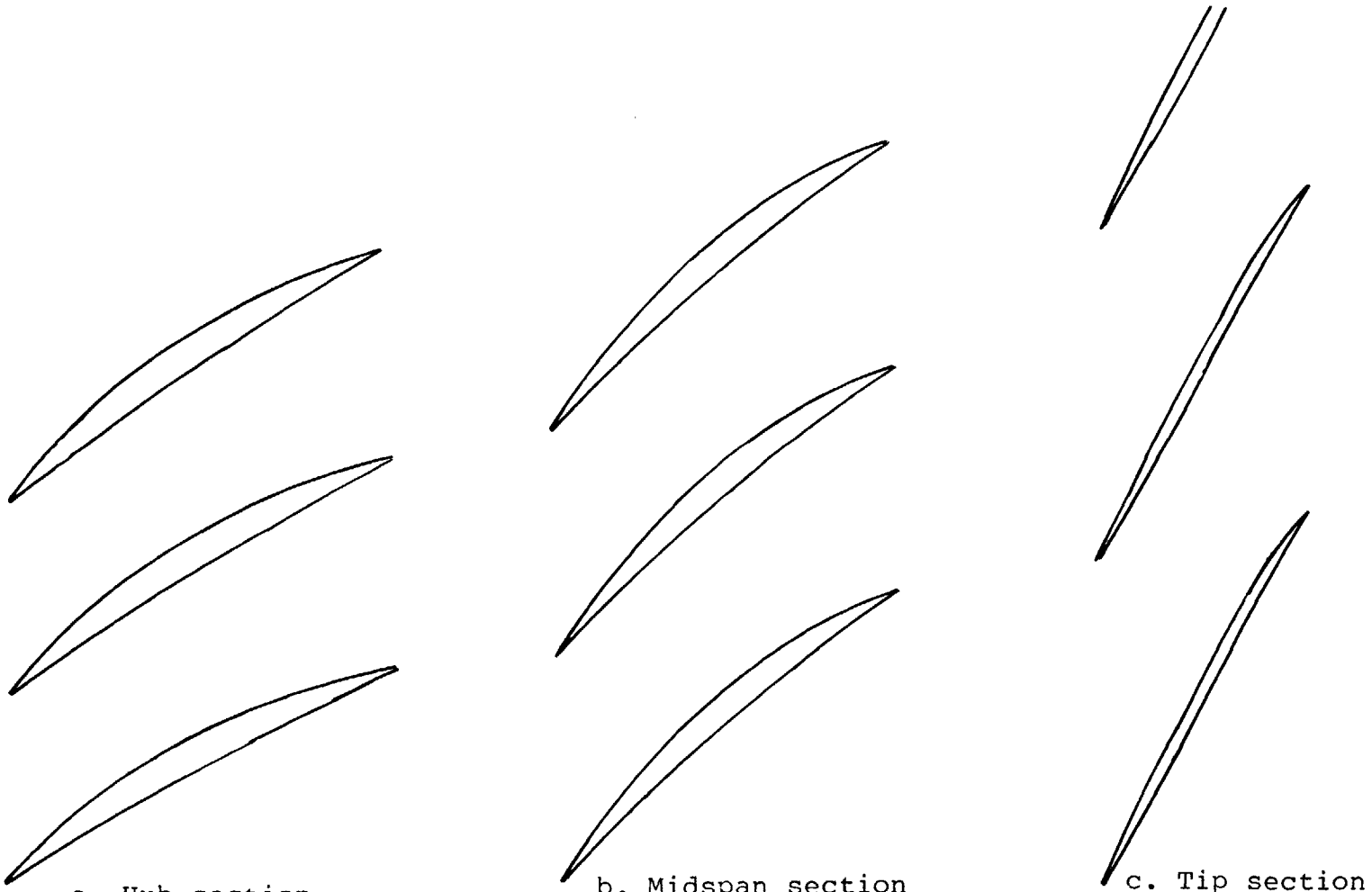

Figure 4. Typical blade sections of NASA low-aspect-ratio rotor.

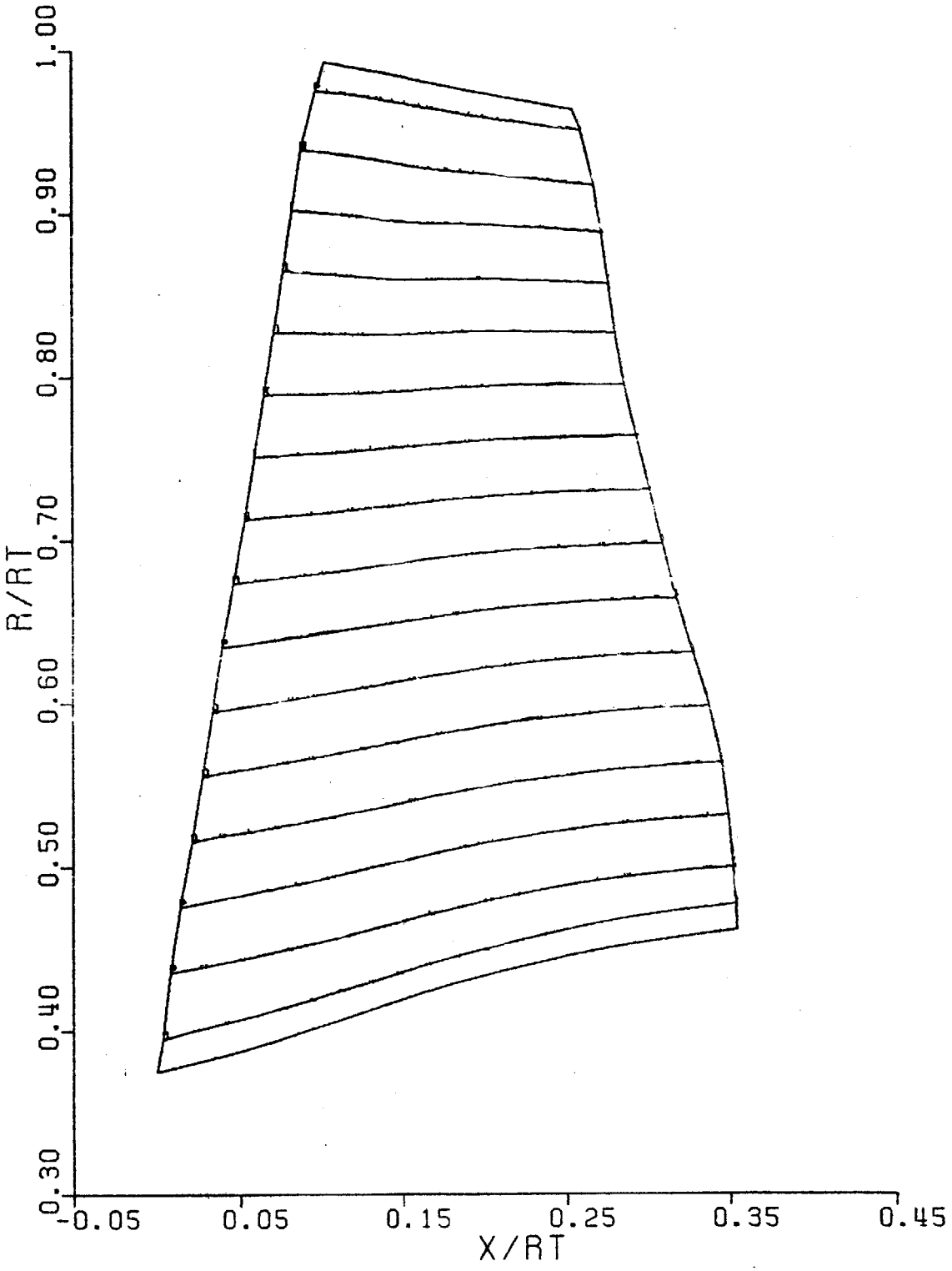

Figure 5. Invisid streamlines for pressure side of the NASA low-aspect-ratio rotor.

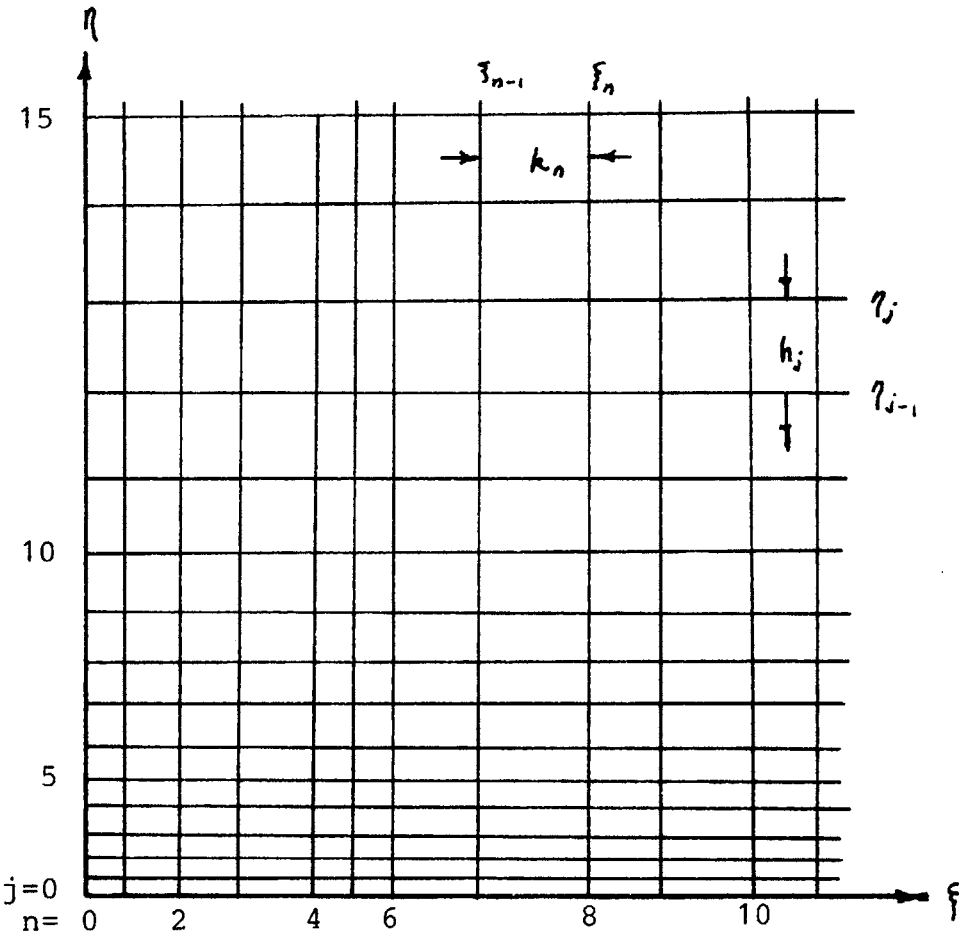

Figure 6. General finite-difference grid.

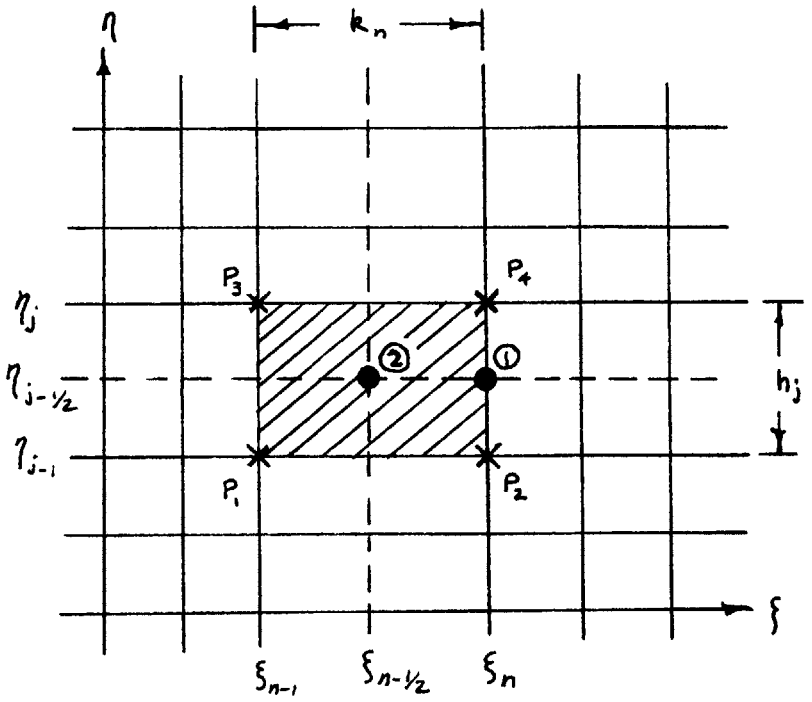

Note: Equations independent of ξ are centered at 1.
Equations dependent on ξ are centered at 2.

Figure 7. Sample mesh rectangle.

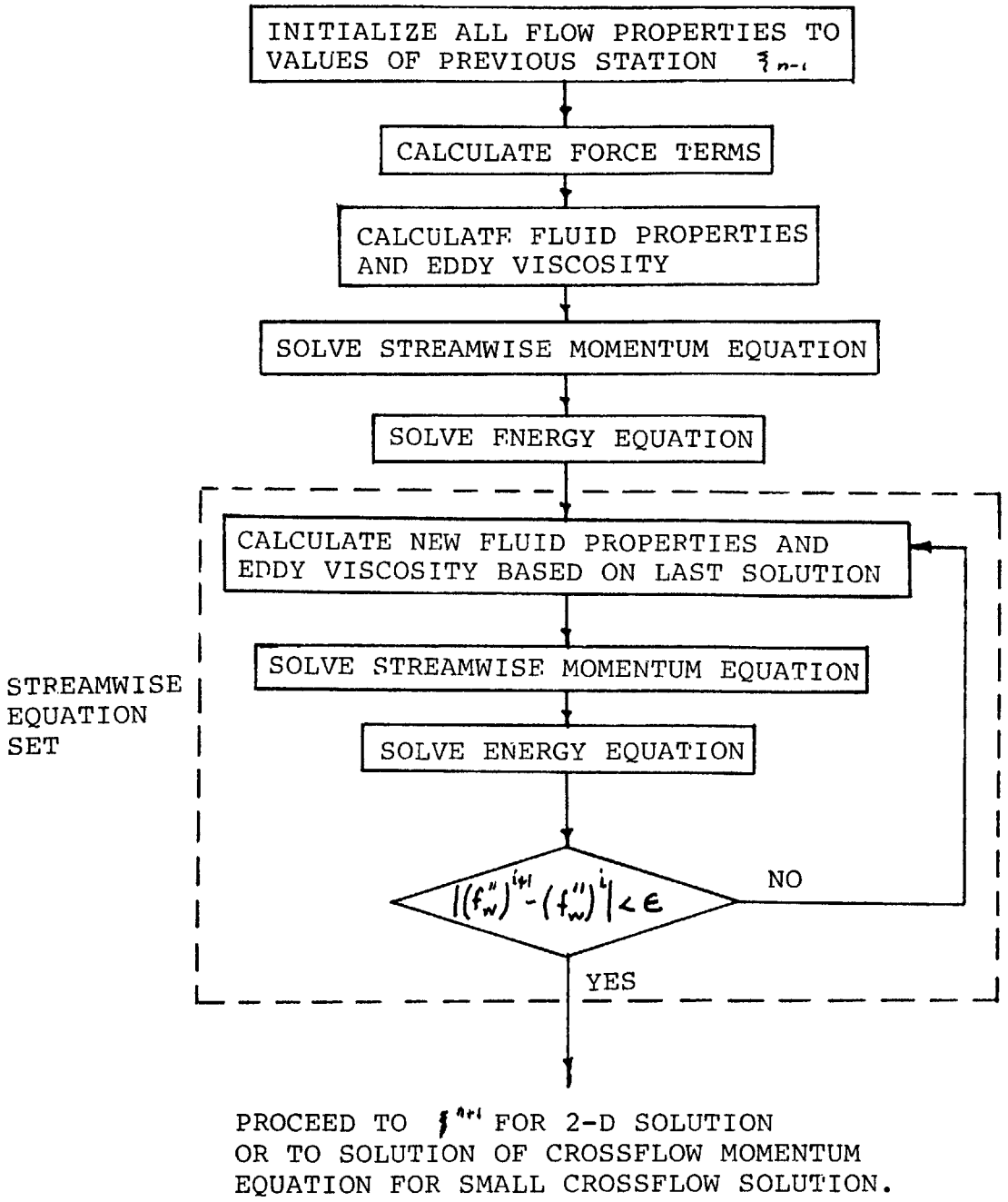

Figure 8. Flow chart for solution of the streamwise equation set.

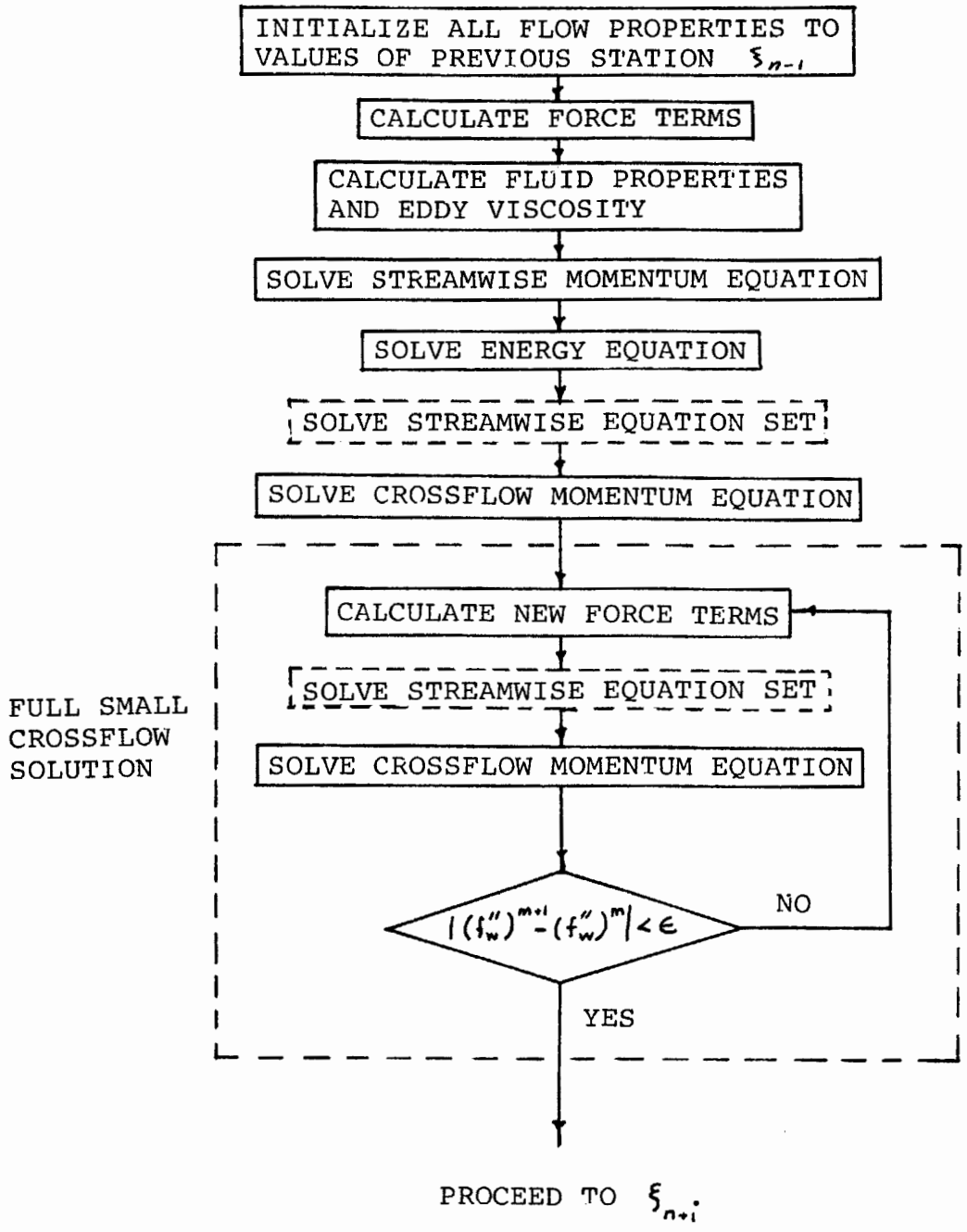

Figure 9. Flow chart for complete small crossflow solution scheme.

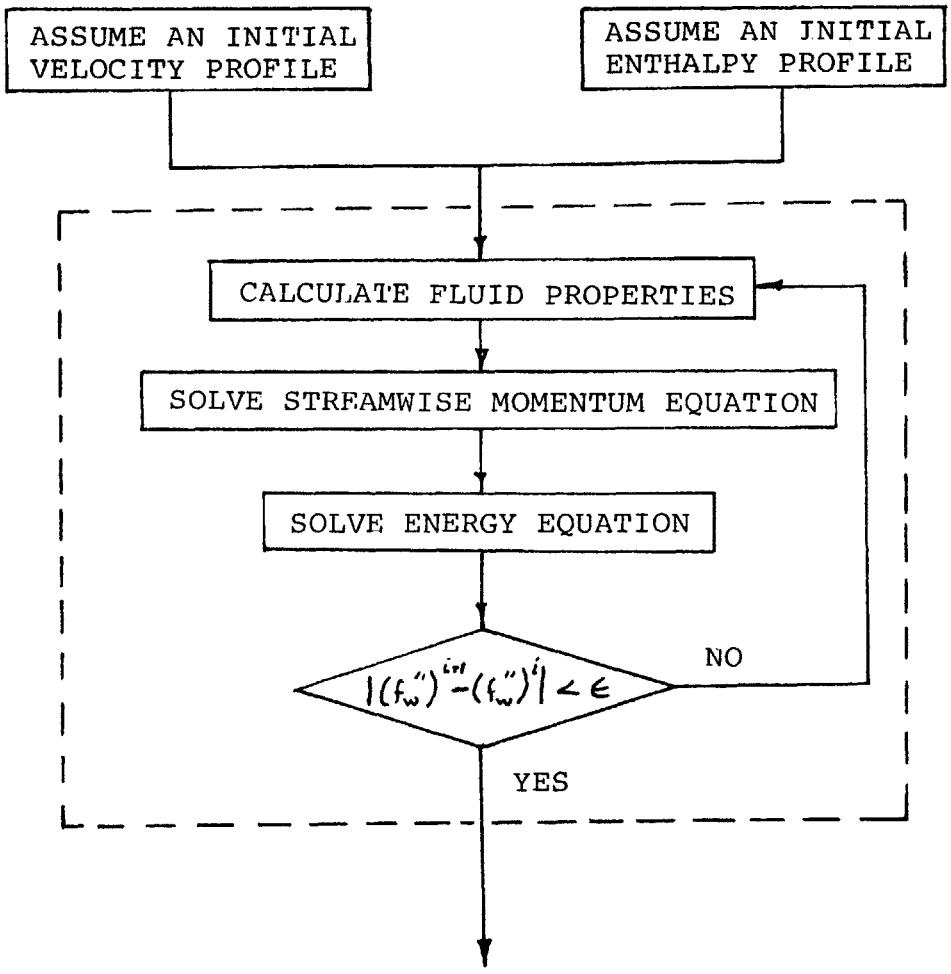

Figure 10. Flow chart starting solution.

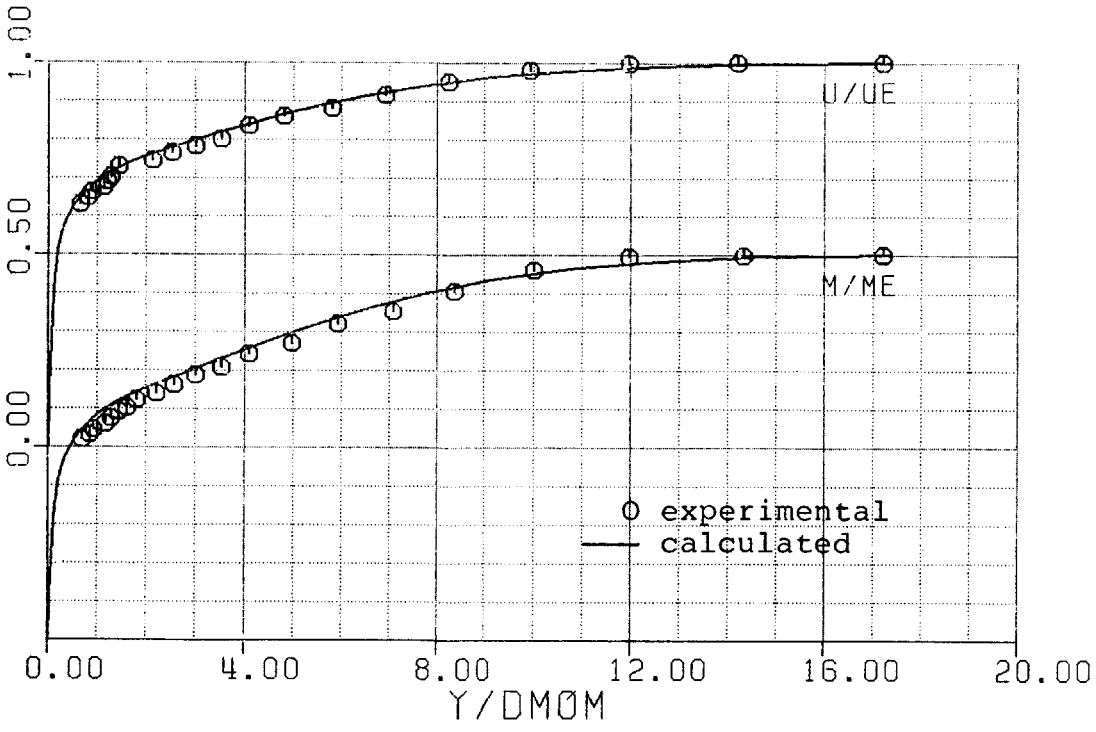

Figure 11. Comparison with experimental results for adiabatic flat plate. Data of Coles (1953) Test 3 D.

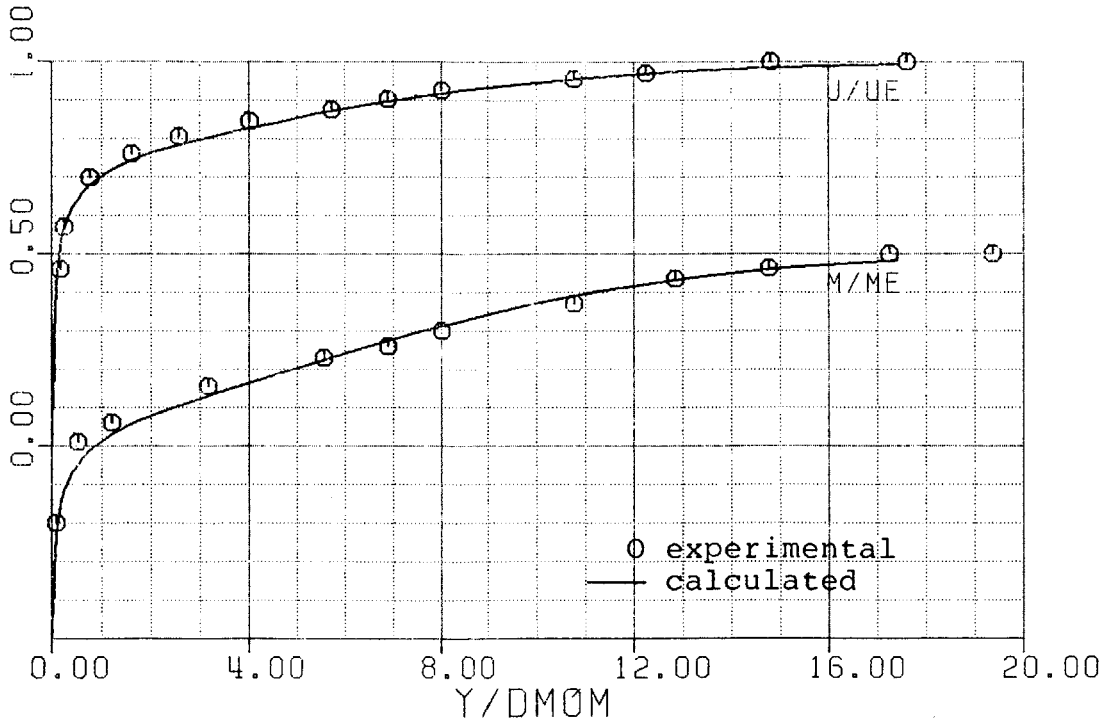

Figure 12. Comparison with experimental results for adiabatic flat plate. Data of Matting (1961).

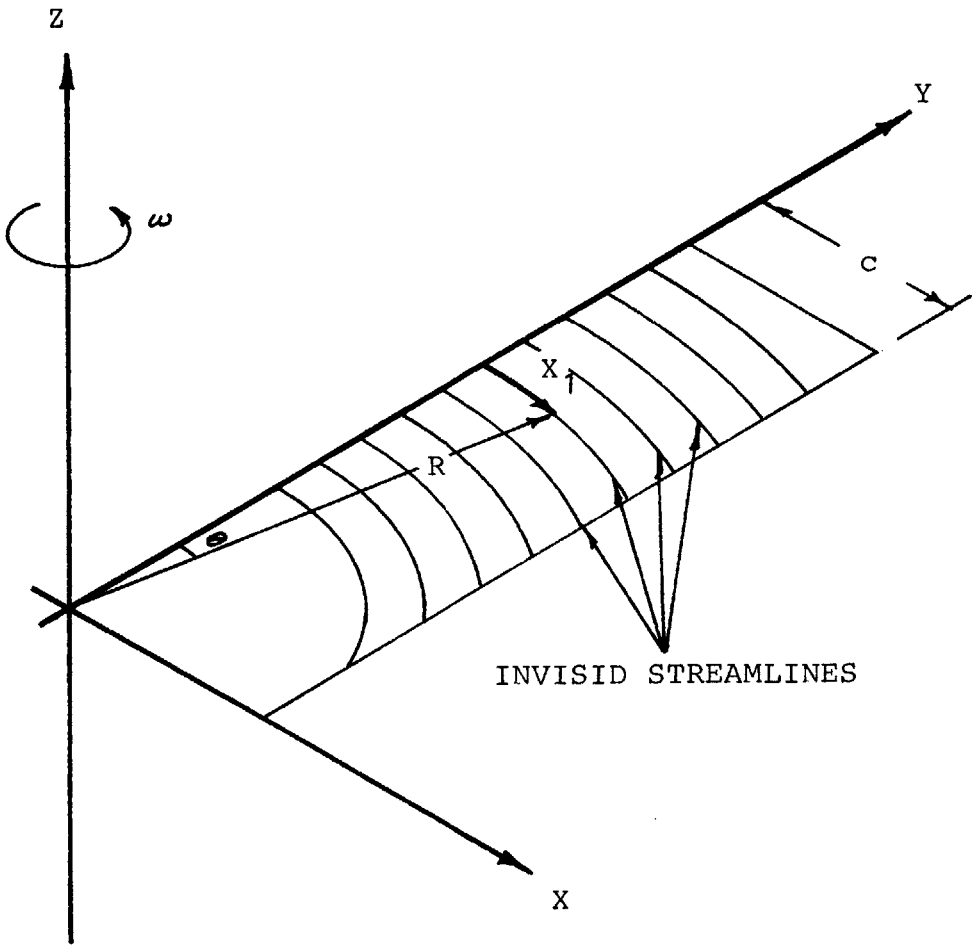

Figure 13. Flat plate blade.

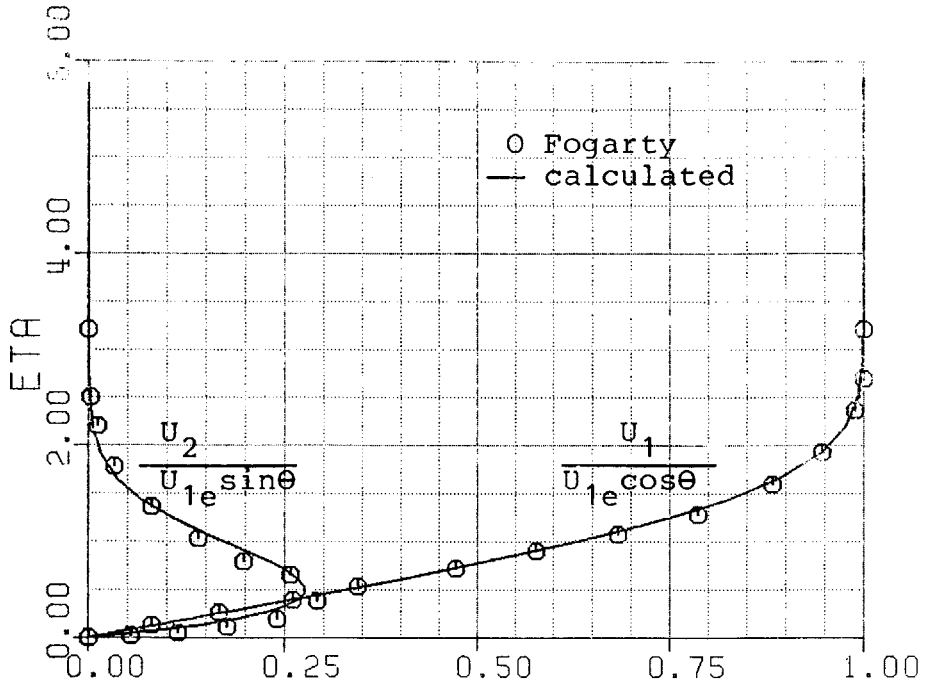

Figure 14. Comparison with Fogarty for flat plate blade, $R \gg X_1$.

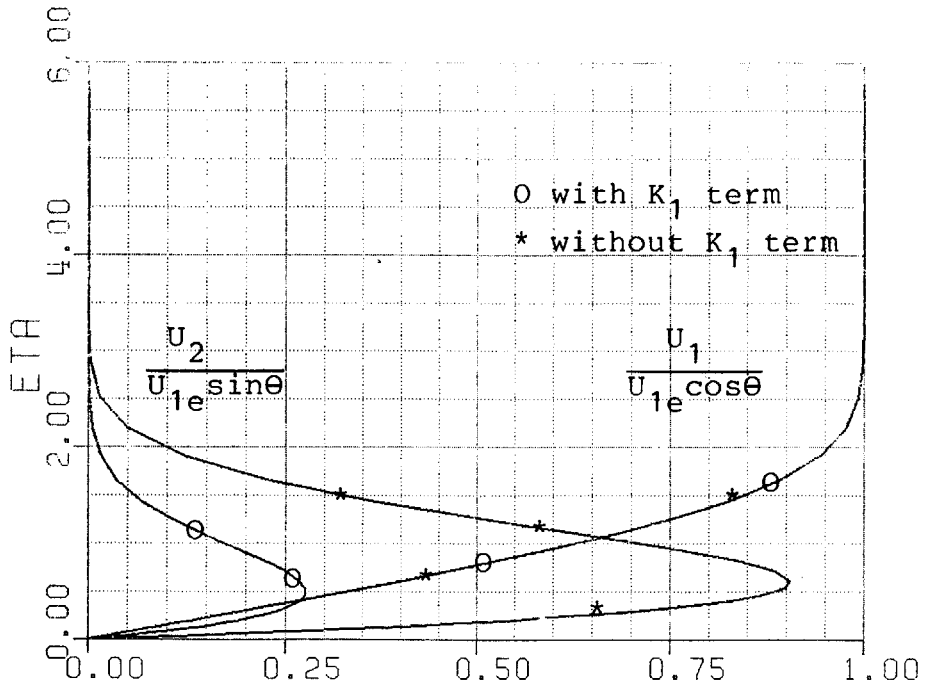

Figure 15. Effect of curvature term on flat plate blade.

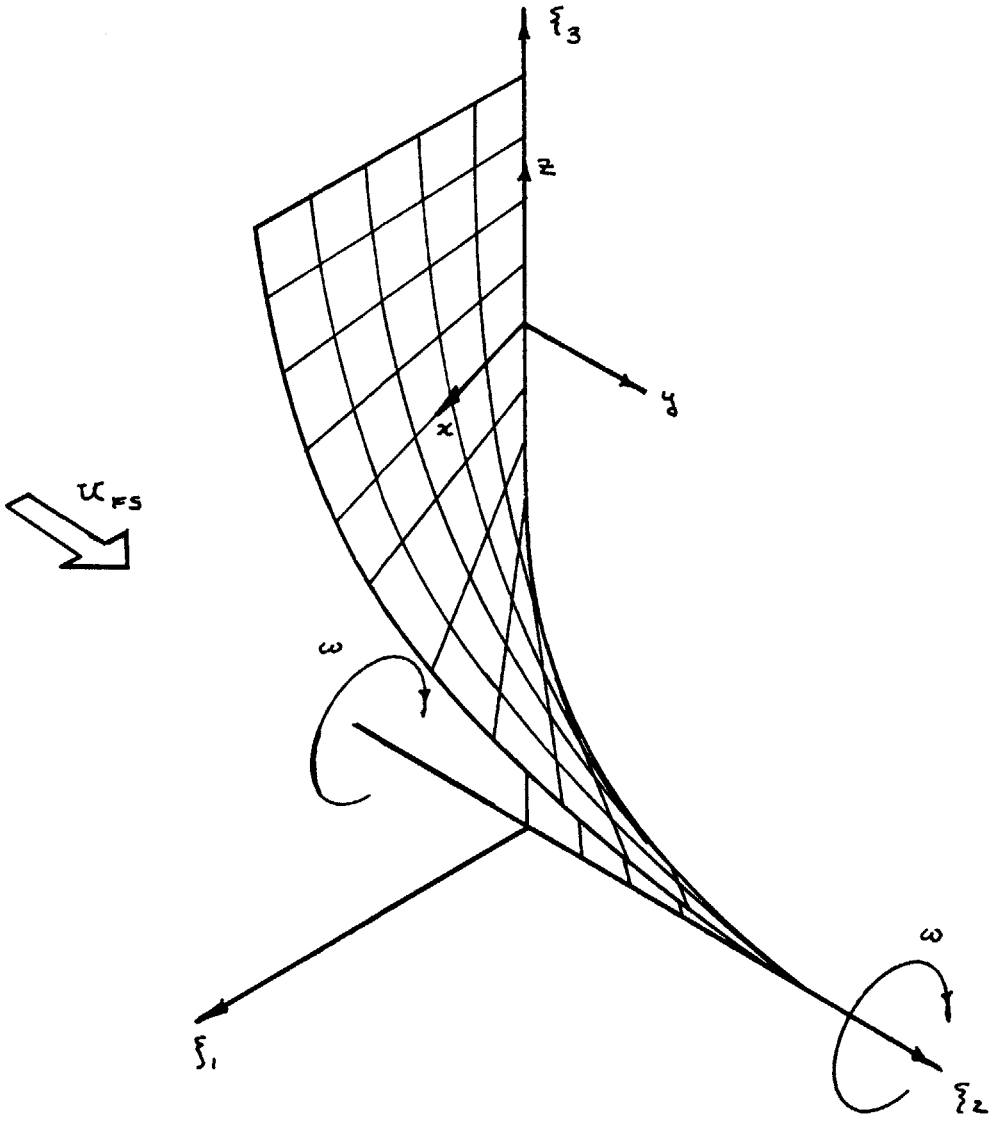

Figure 16. Helical blade.

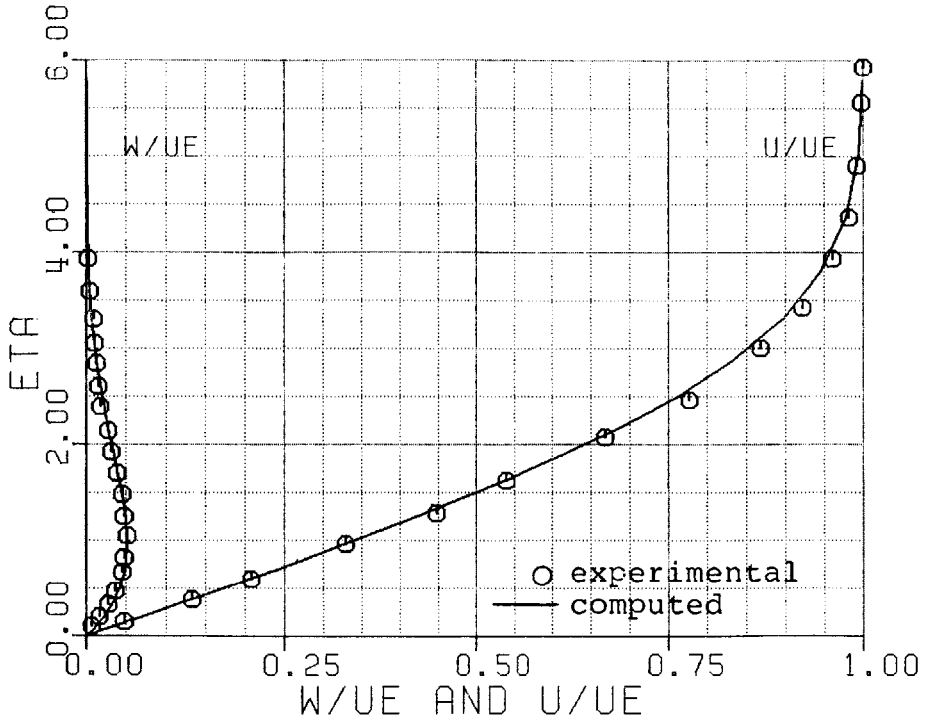

a.

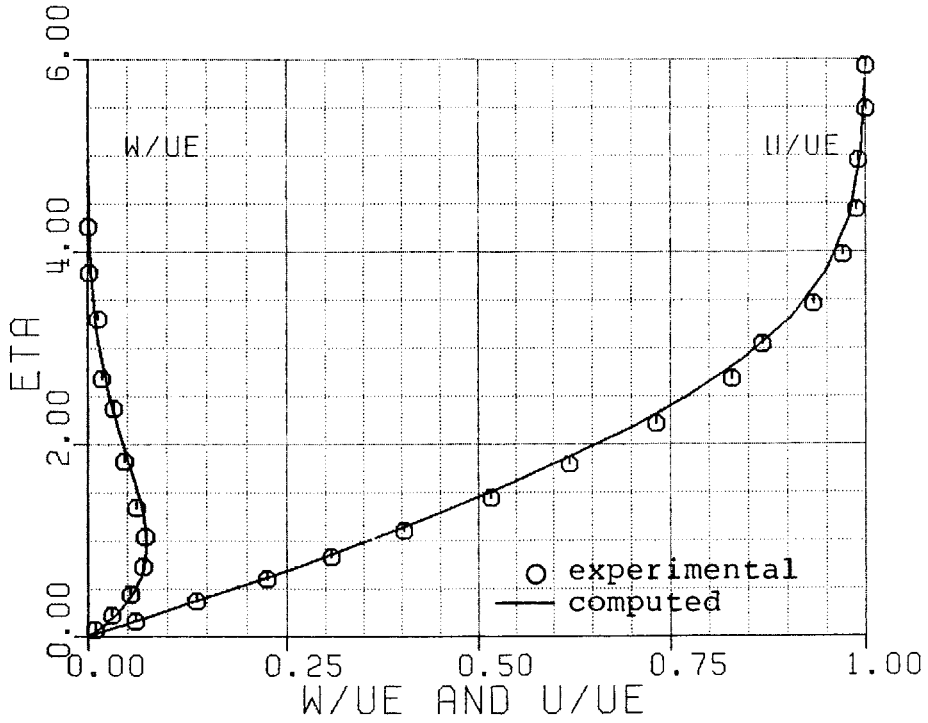

b.

Figure 17. Comparison of calculated helical blade solutions with those of Miyake and Fujita.

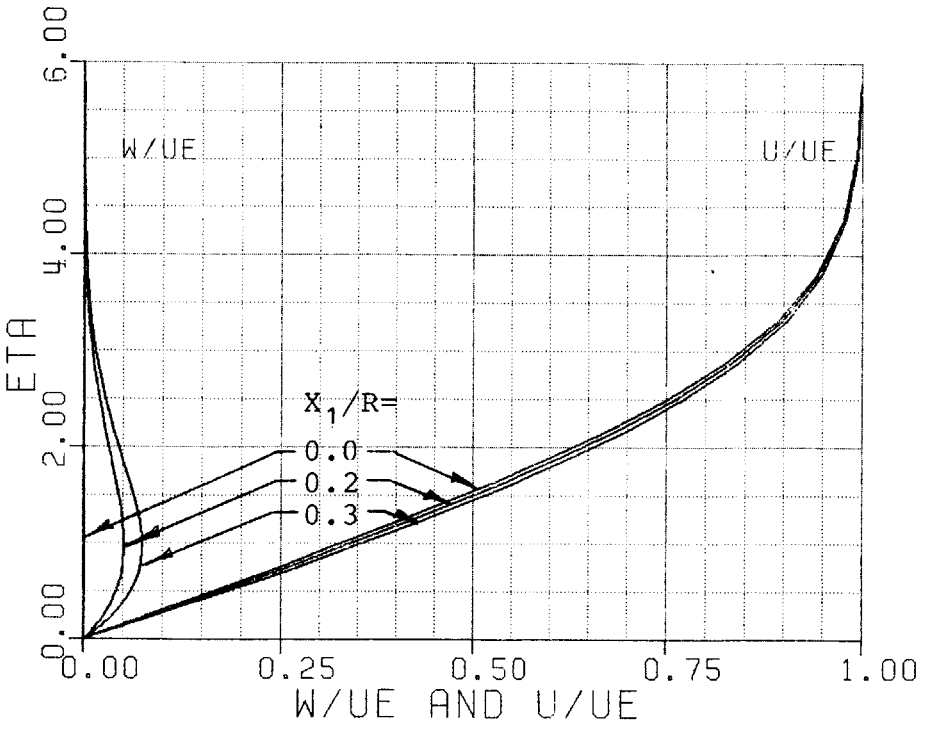

Figure 18. Variation of velocity profiles with distance down the streamline where $\phi_0 = \tan^{-1}(0.2)$.

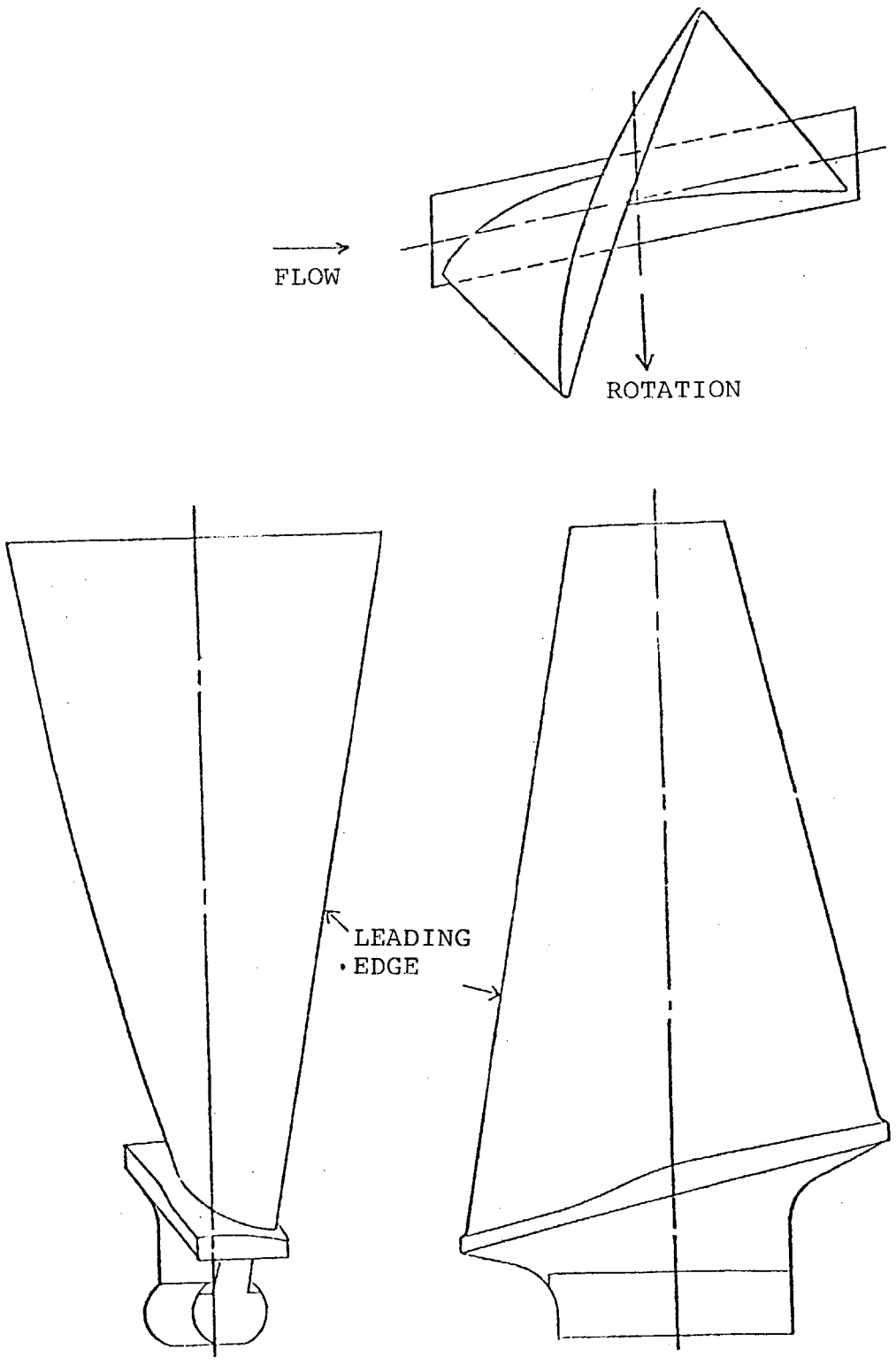

Figure 19. NASA low-aspect-ratio blade.

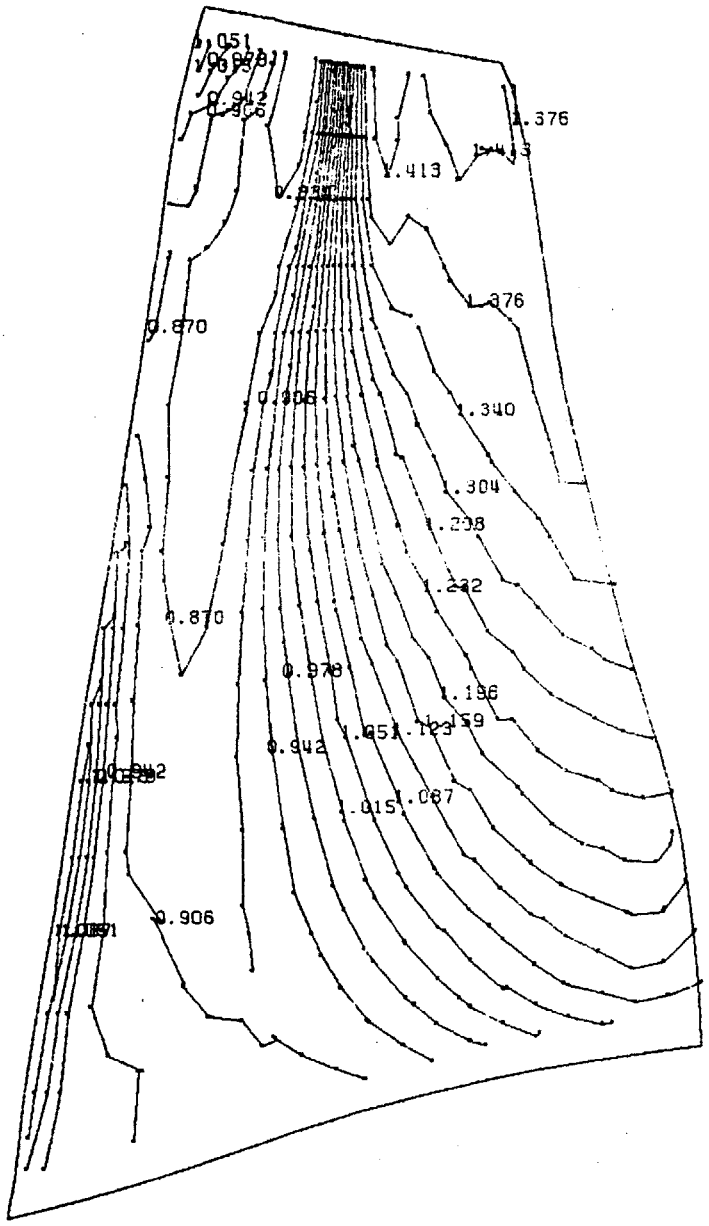

Figure 20. NASA low-aspect-ratio rotor invisid pressure contours, pressure side.

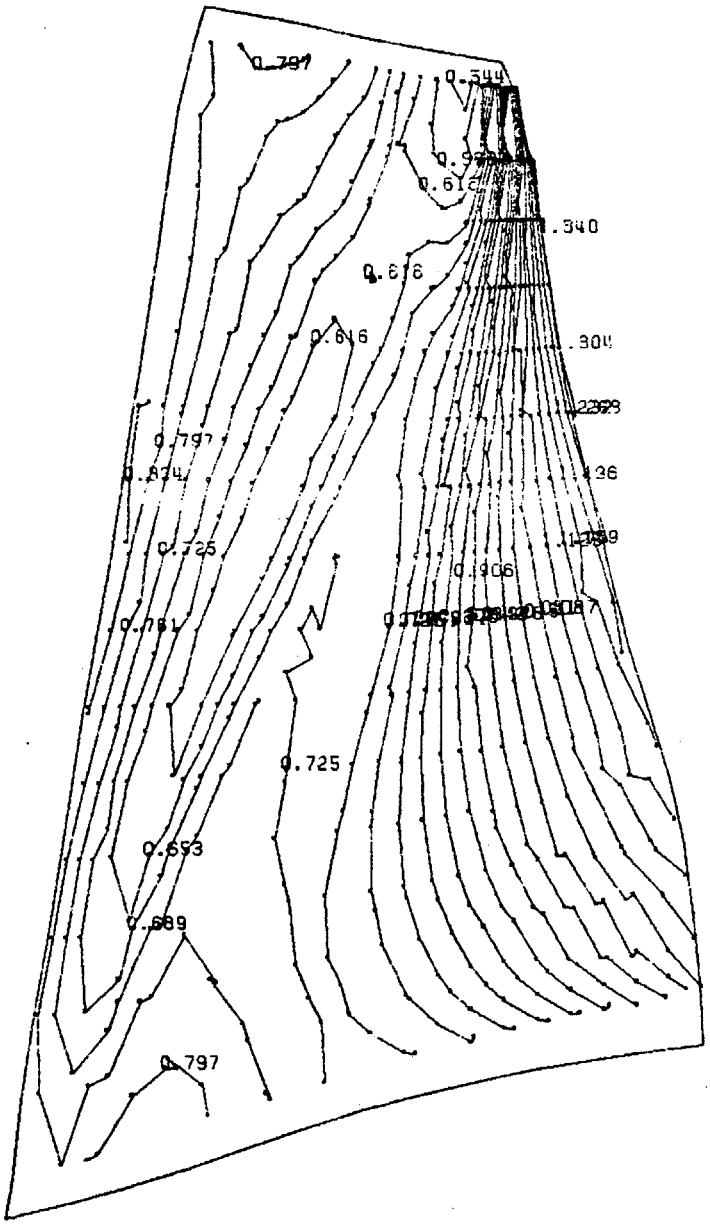

Figure 21. NASA low-aspect-ratio rotor invisid pressure contours, suction side.

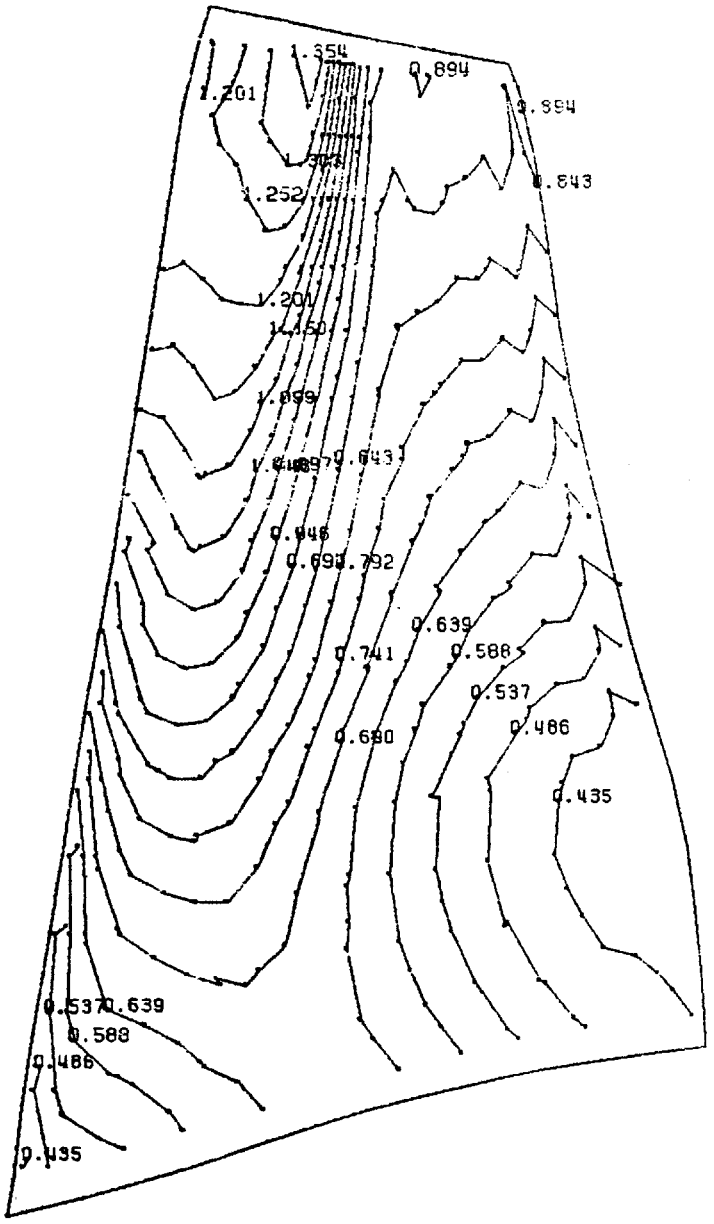

Figure 22. NASA low-aspect-ratio rotor invisid Mach number contours, pressure side.

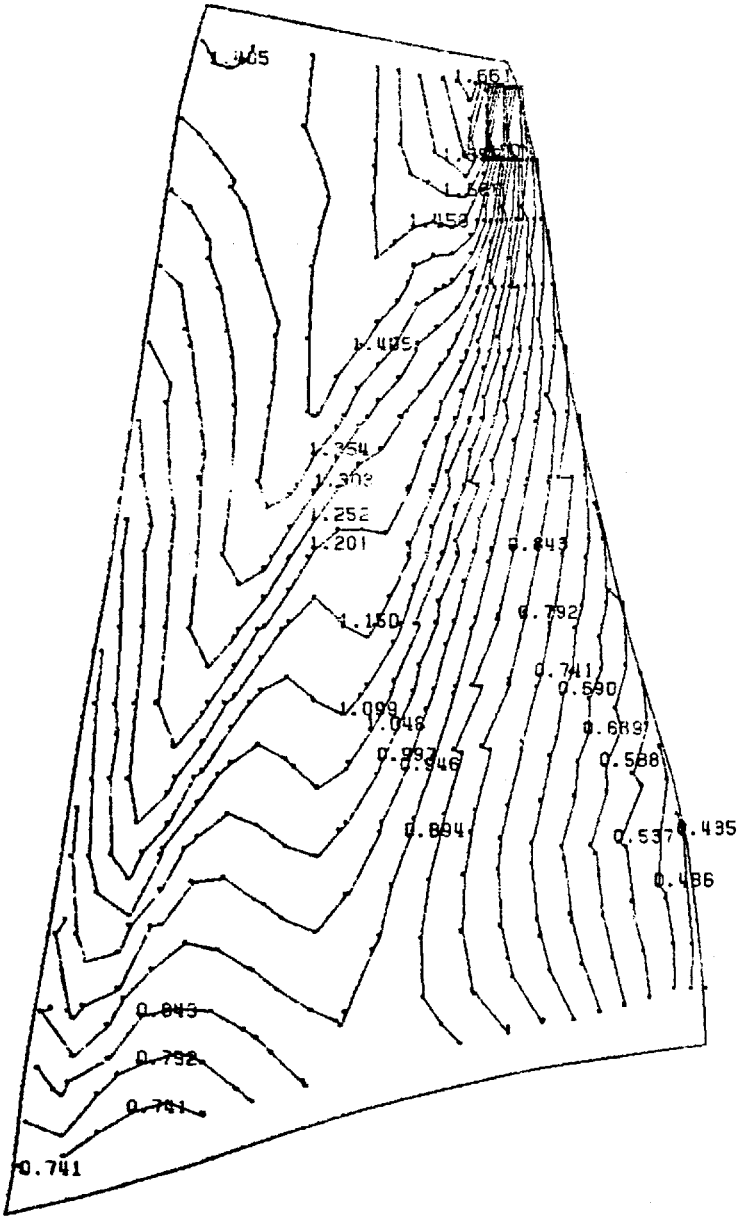

Figure 23. NASA low-aspect-ratio rotor invisid Mach number contours, suction side.

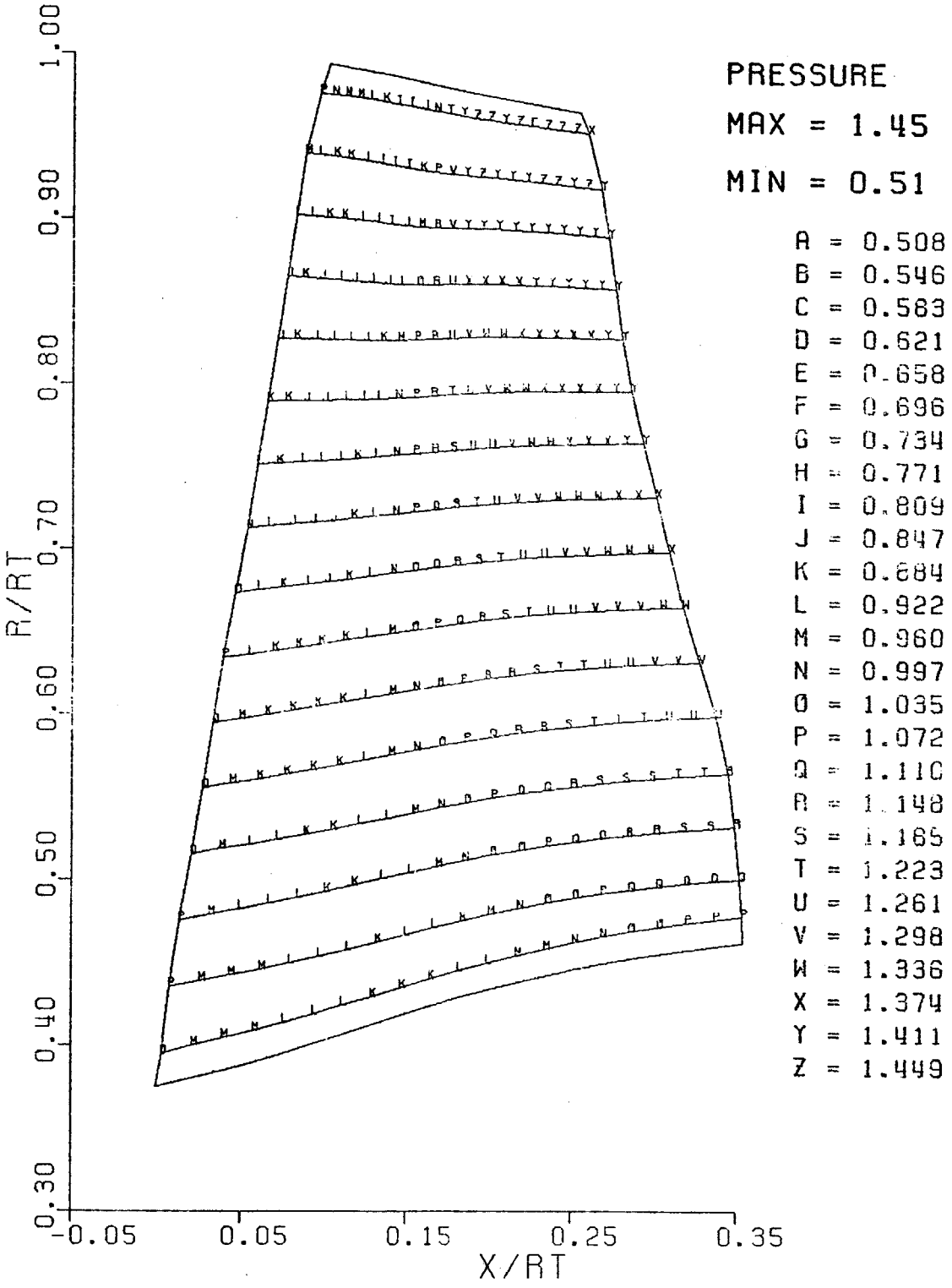

Figure 24. NASA low-aspect-ratio rotor invisid surface streamlines, pressure side.

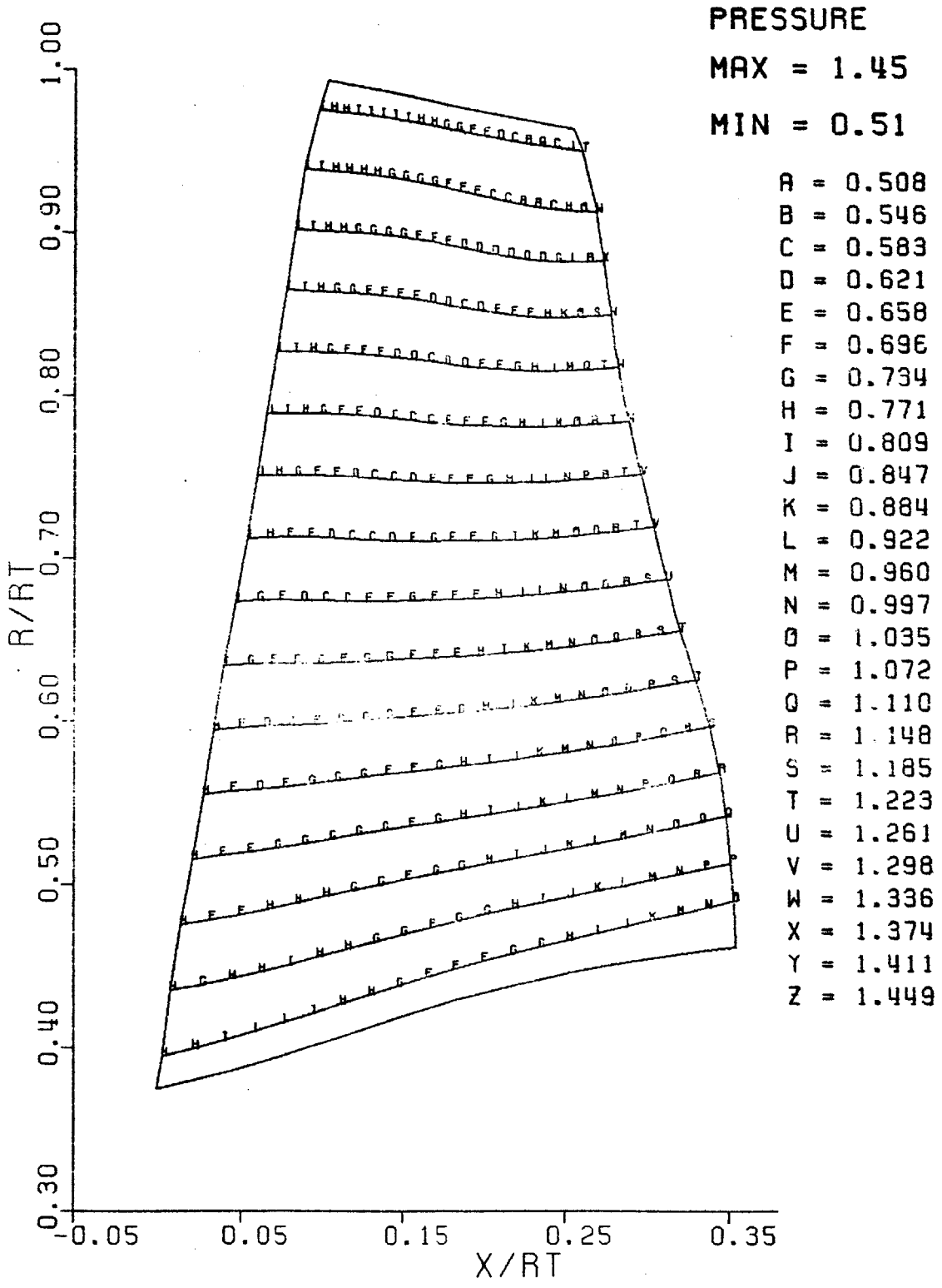

Figure 25. NASA low-aspect-ratio rotor invisid surface streamlines, suction side.

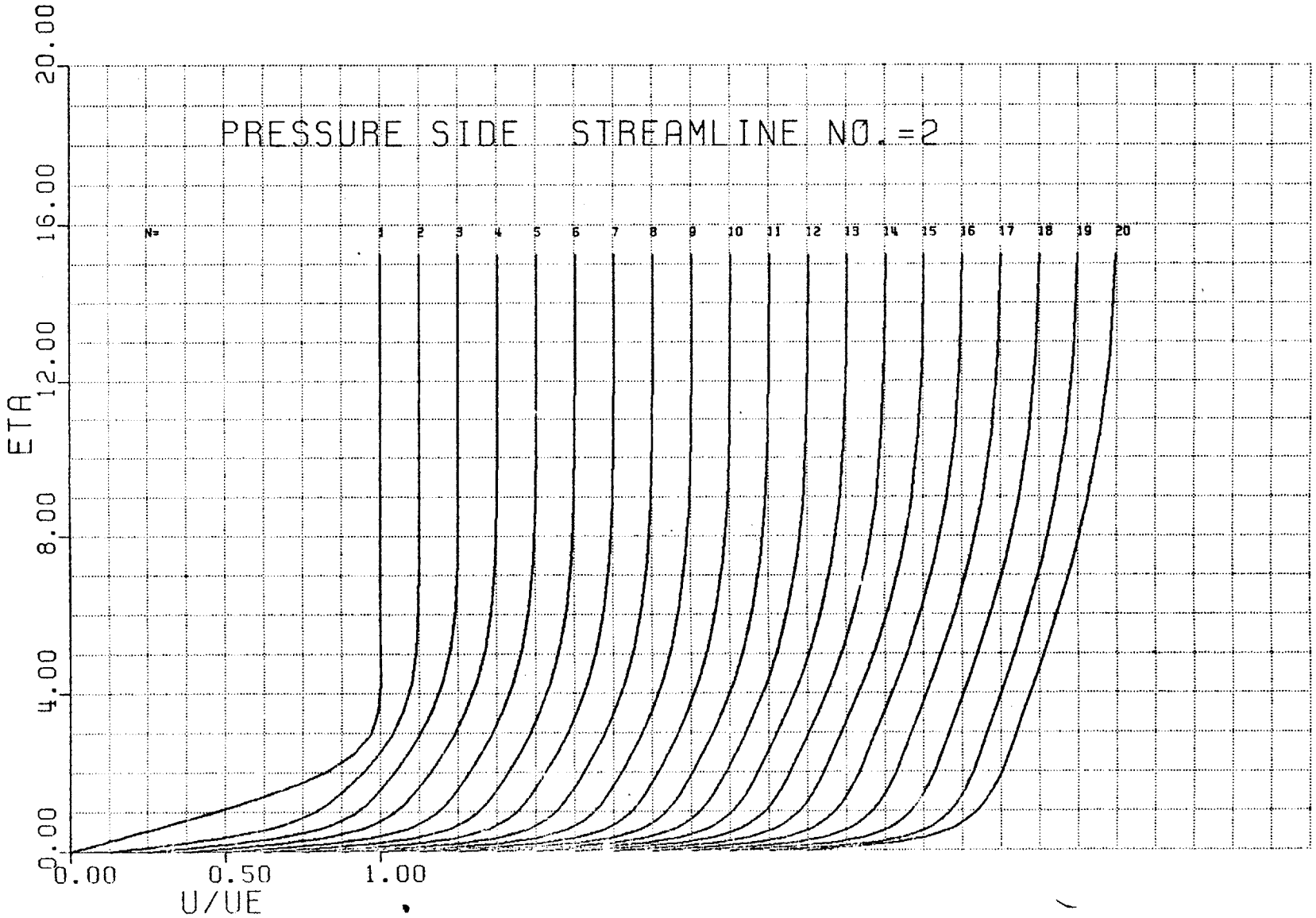

Figure 26. Streamwise velocity profile development, Streamline 2, Pressure side.

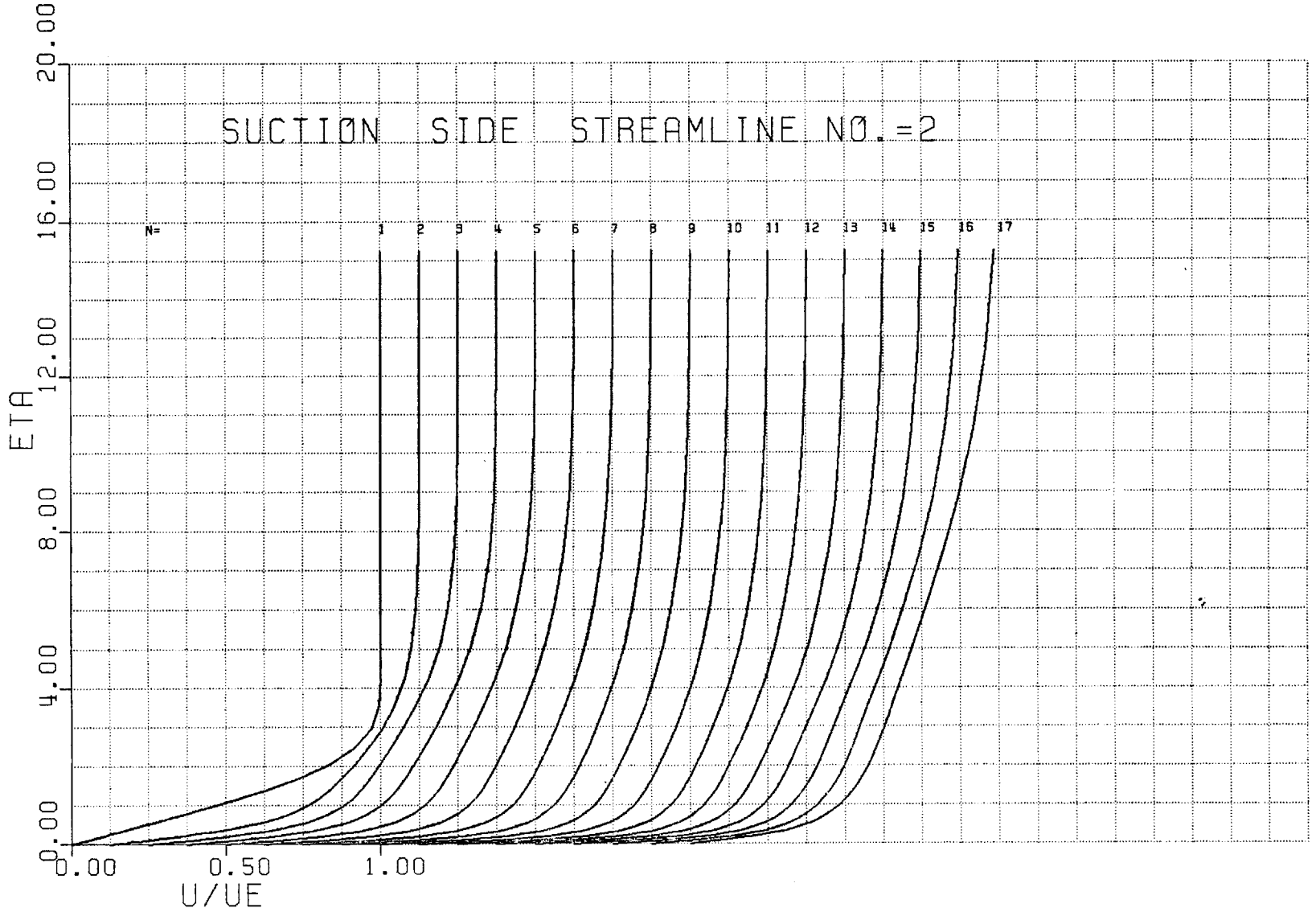

Figure 27. Streamwise velocity profile development, Streamline 2, Suction side.

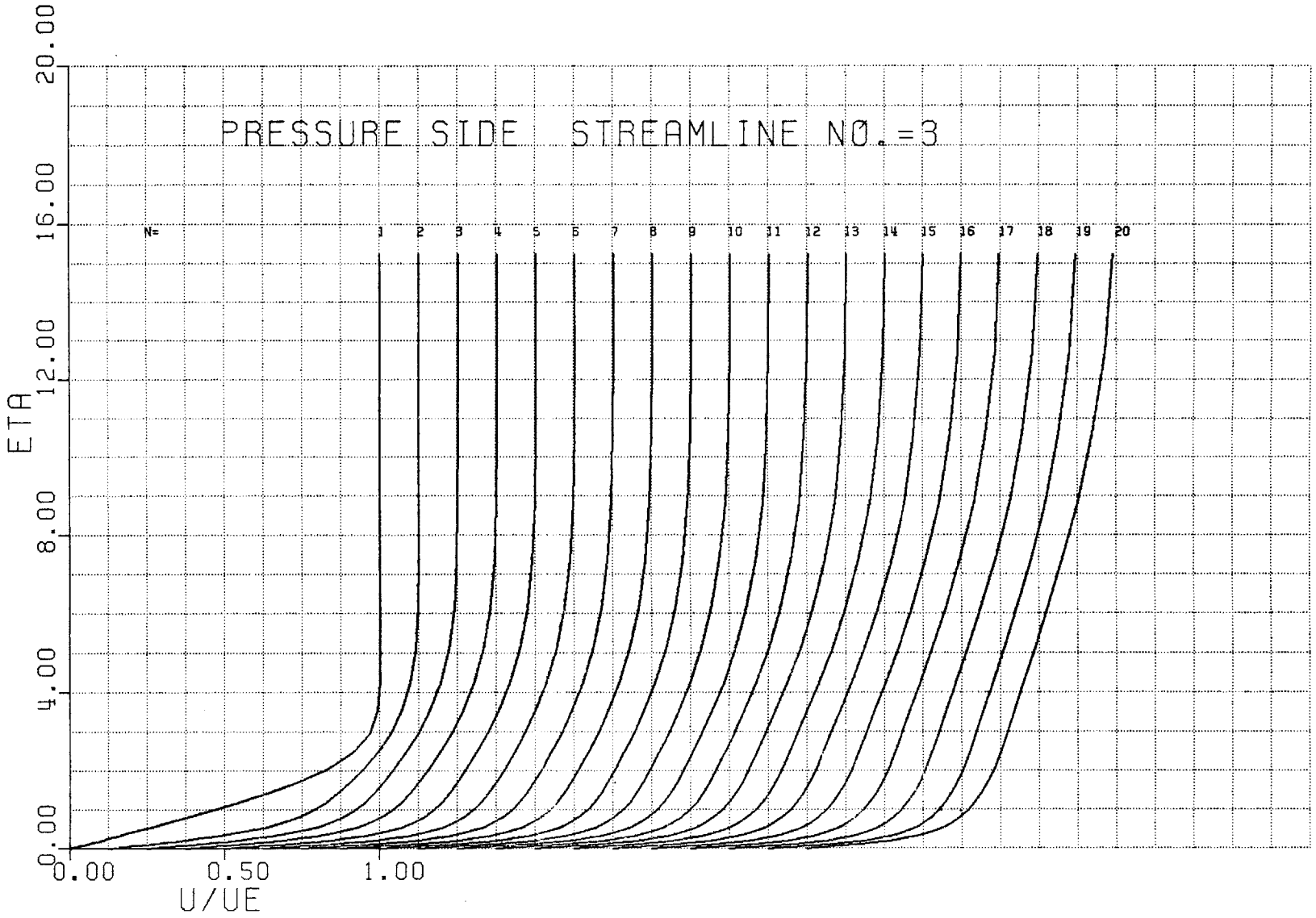

Figure 28. Streamwise velocity profile development, Streamline 3, Pressure side.

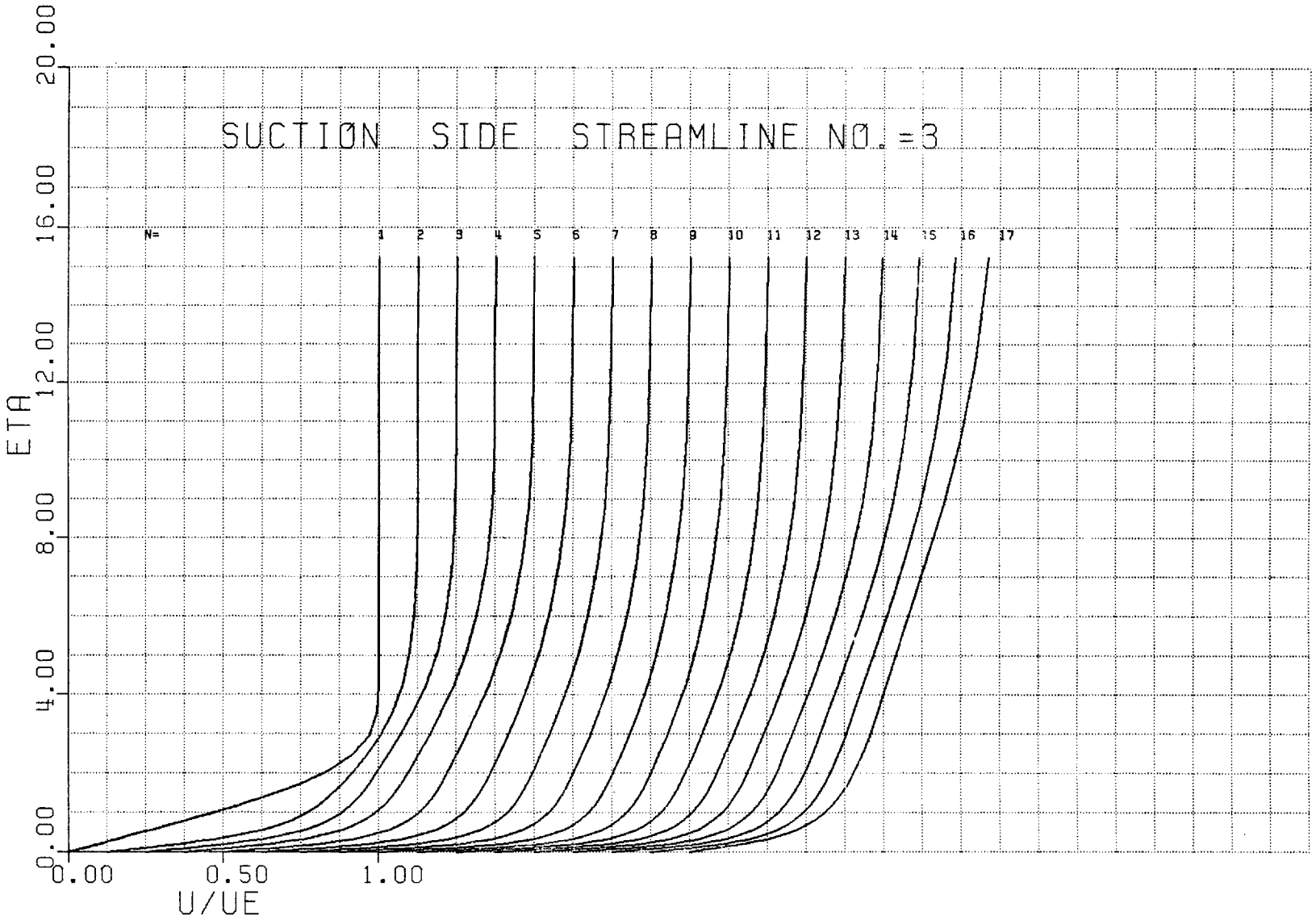

Figure 29. Streamwise velocity profile development, Streamline 3, Suction side.

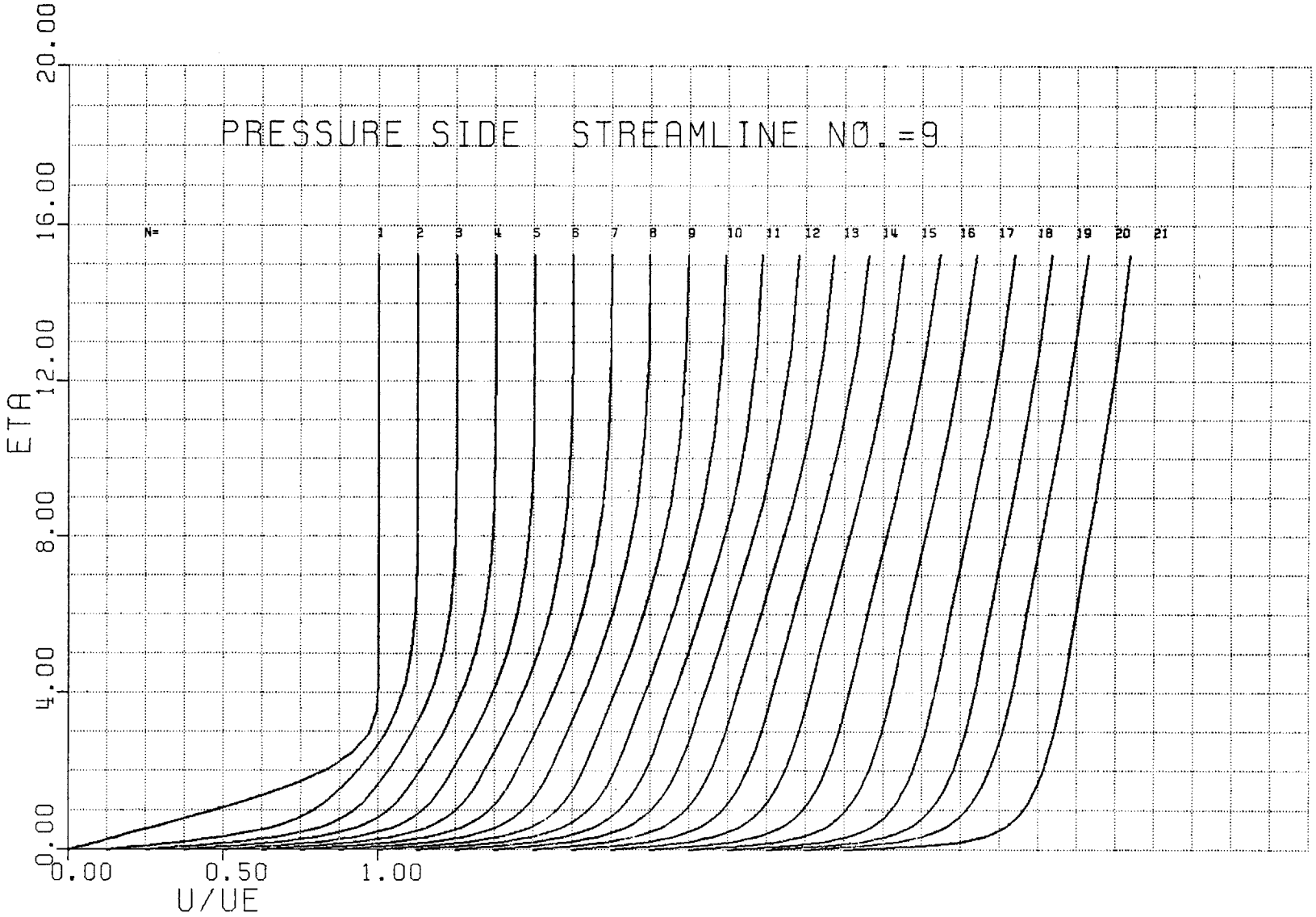

Figure 30. Streamwise velocity profile development, Streamline 9, Pressure side.

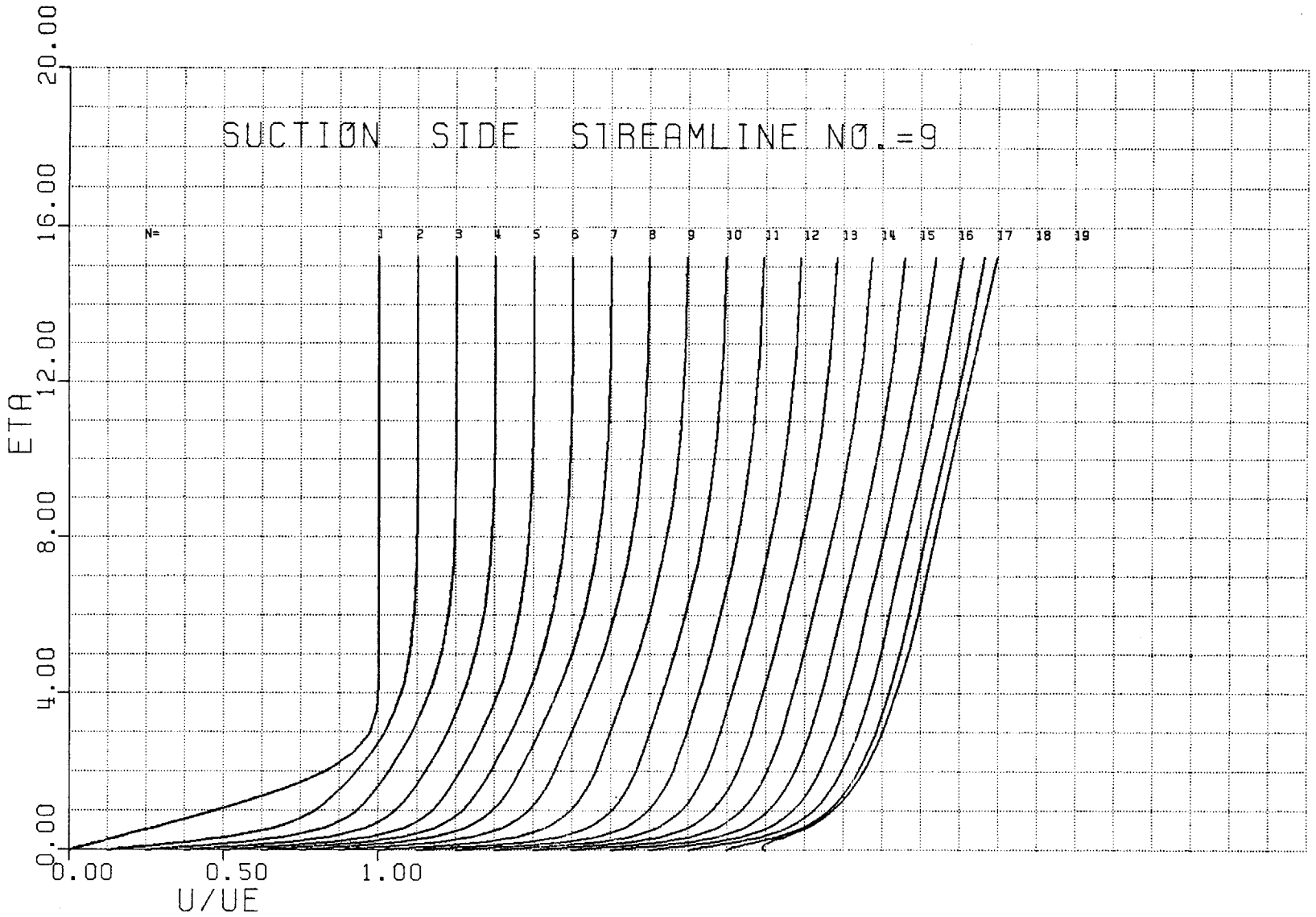

Figure 31. Streamwise velocity profile development, Streamline 9, Suction side.

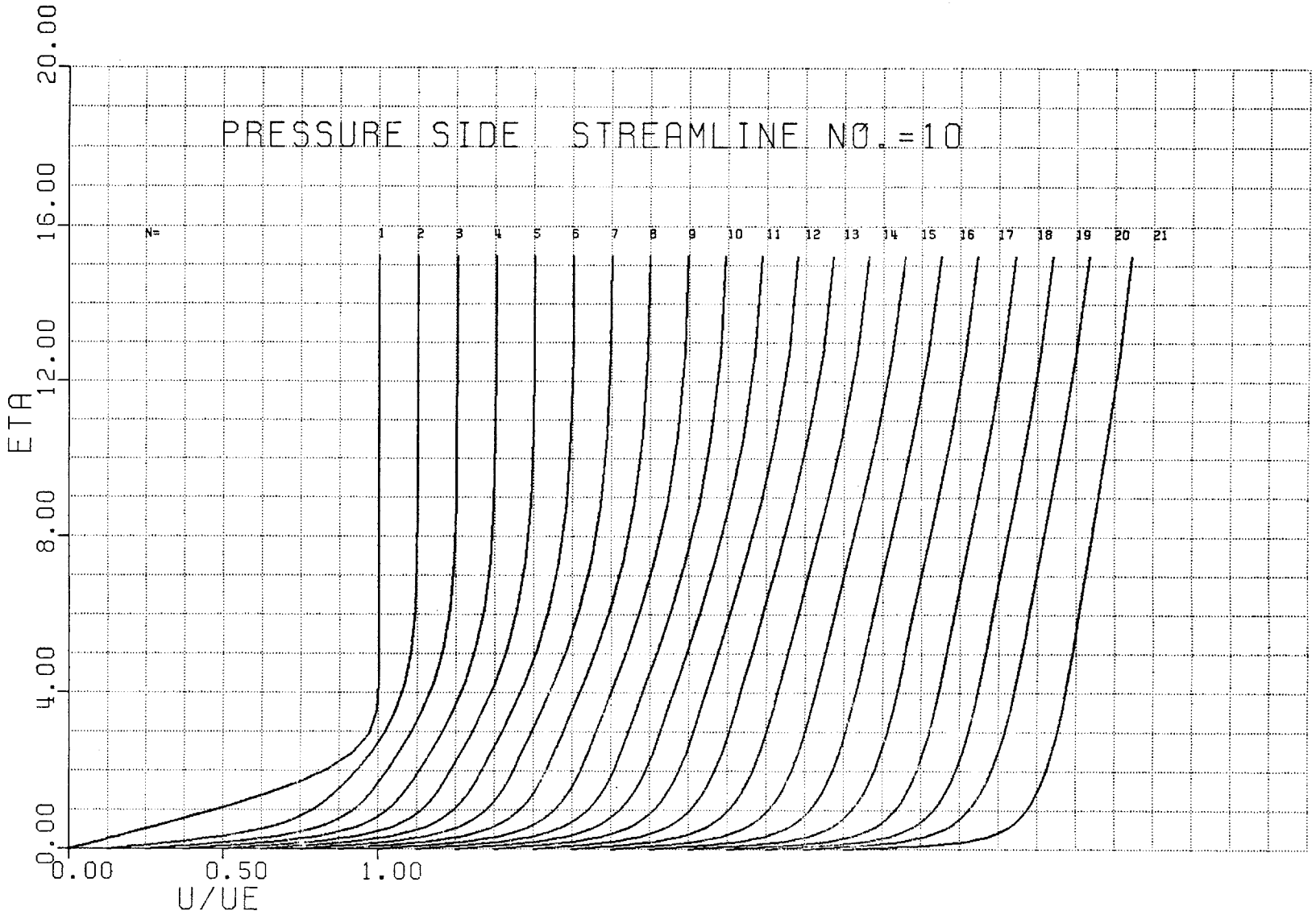

Figure 32. Streamwise velocity profile development, Streamline 10, Pressure side.

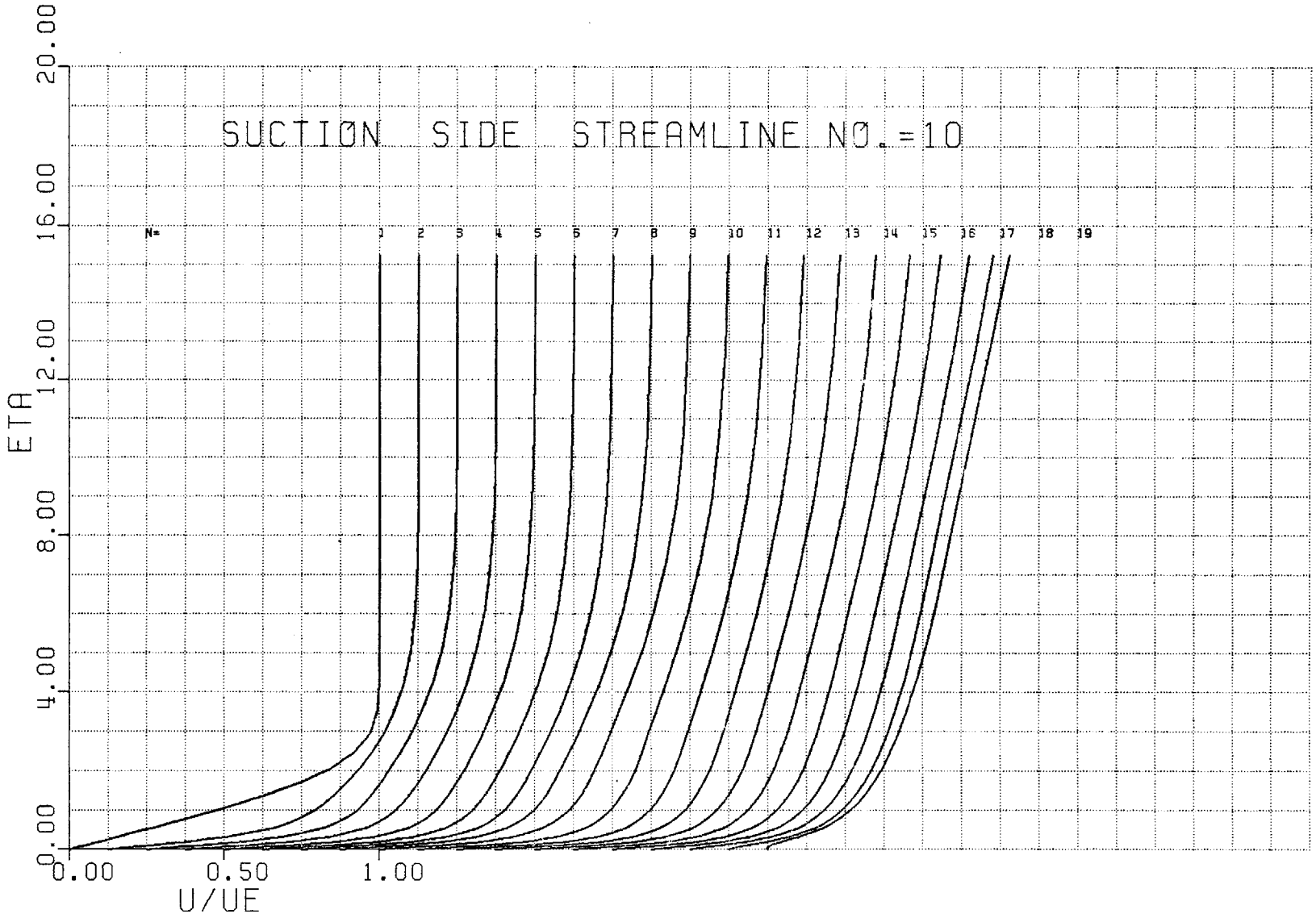

Figure 33. Streamwise velocity profile development, Streamline 10, Suction side.

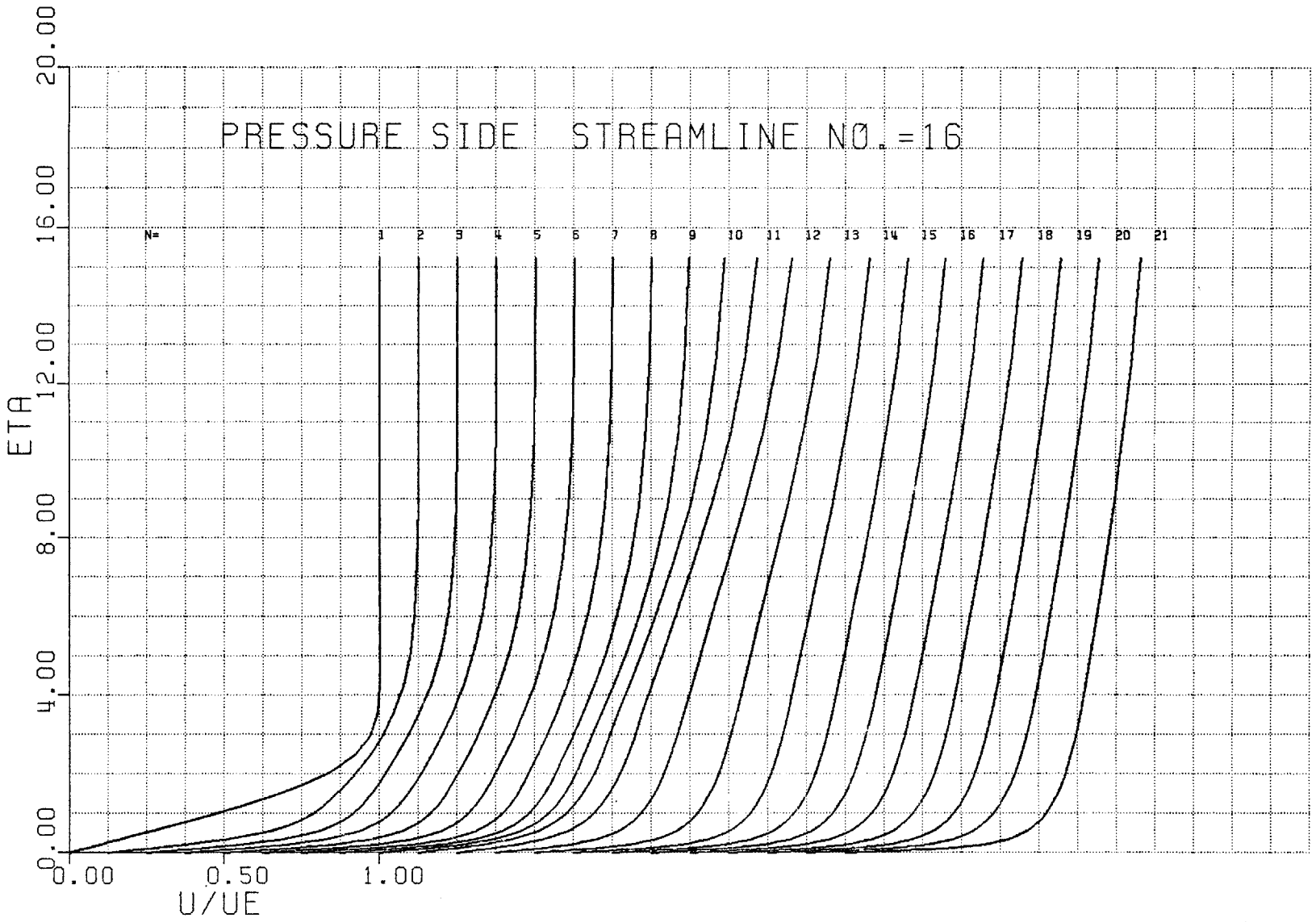

Figure 34. Streamwise velocity profile development, Streamline 16, Pressure side.

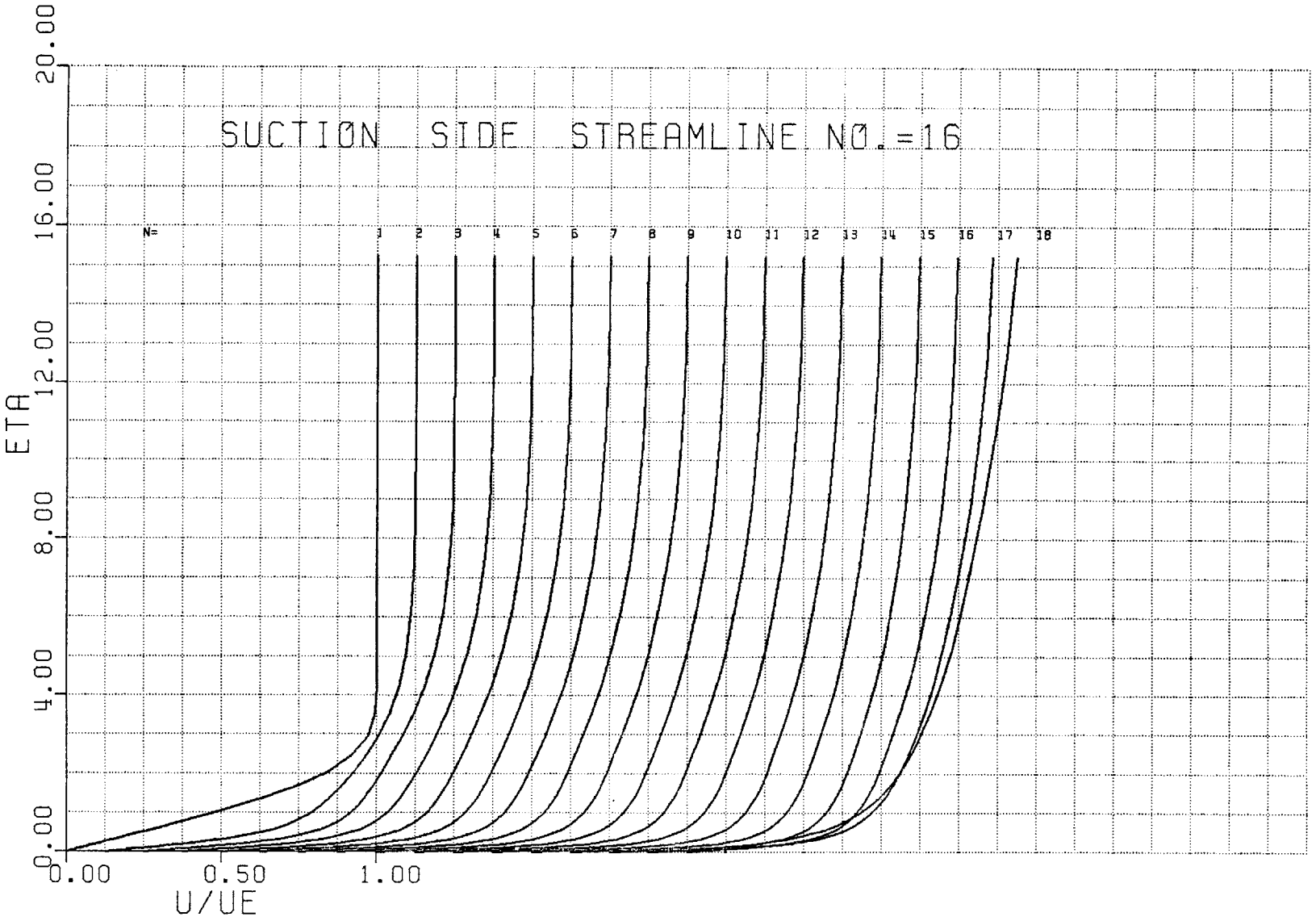

Figure 35. Streamwise velocity profile development, Streamline 16, Suction side.

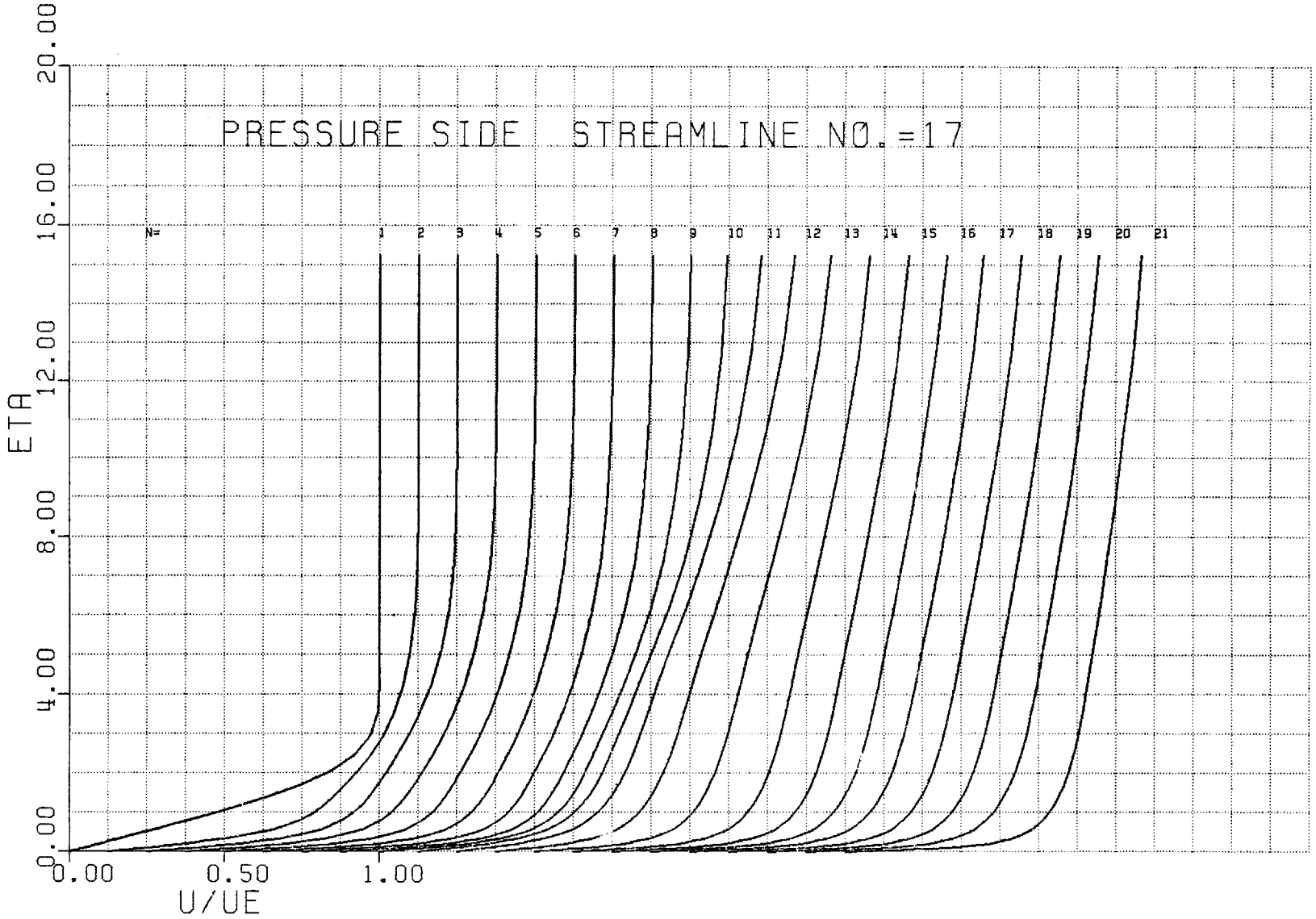

Figure 36. Streamwise velocity profile development, Streamline 17, Pressure side.

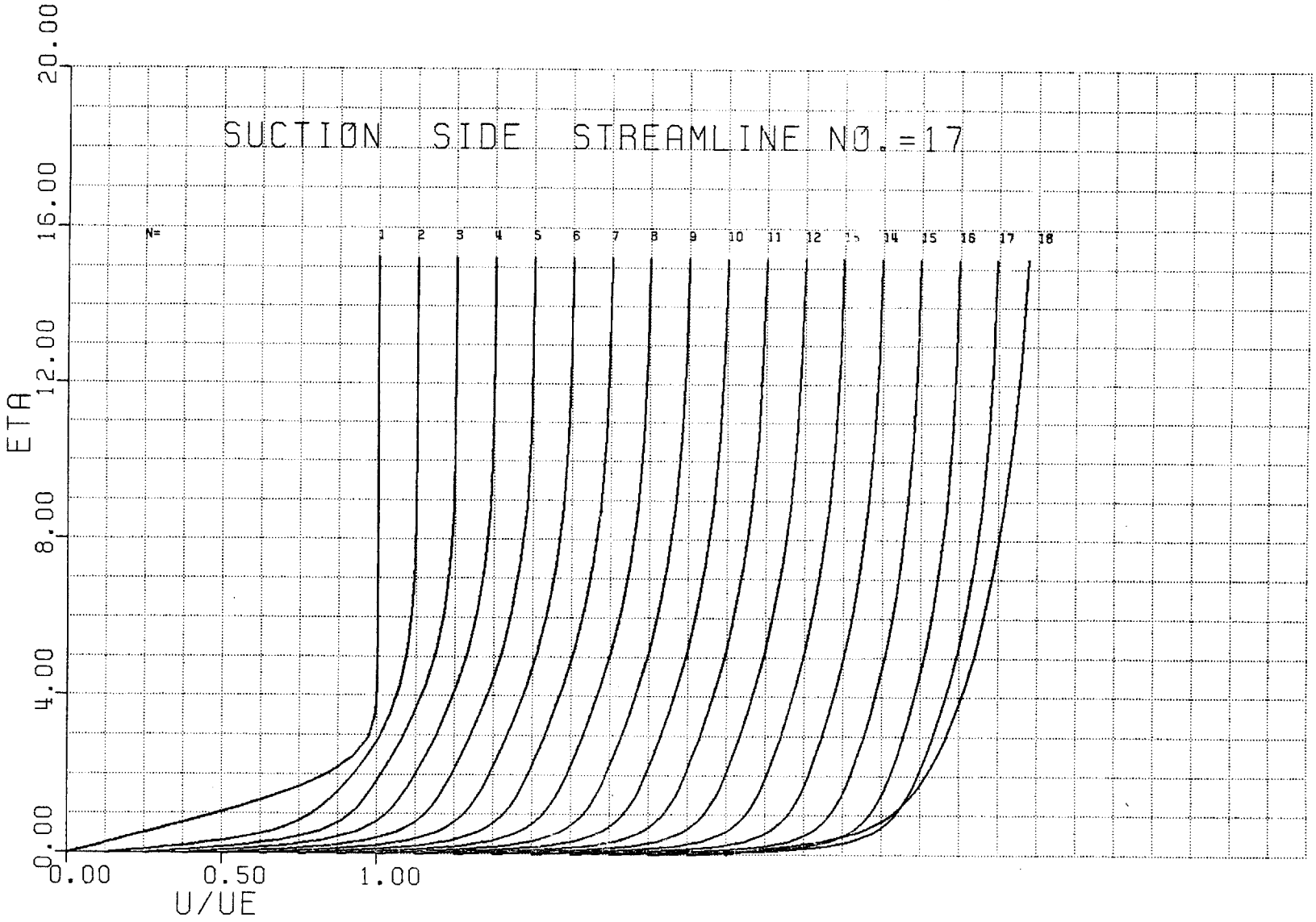

Figure 37. Streamwise velocity profile development, Streamline 17, Suction side.

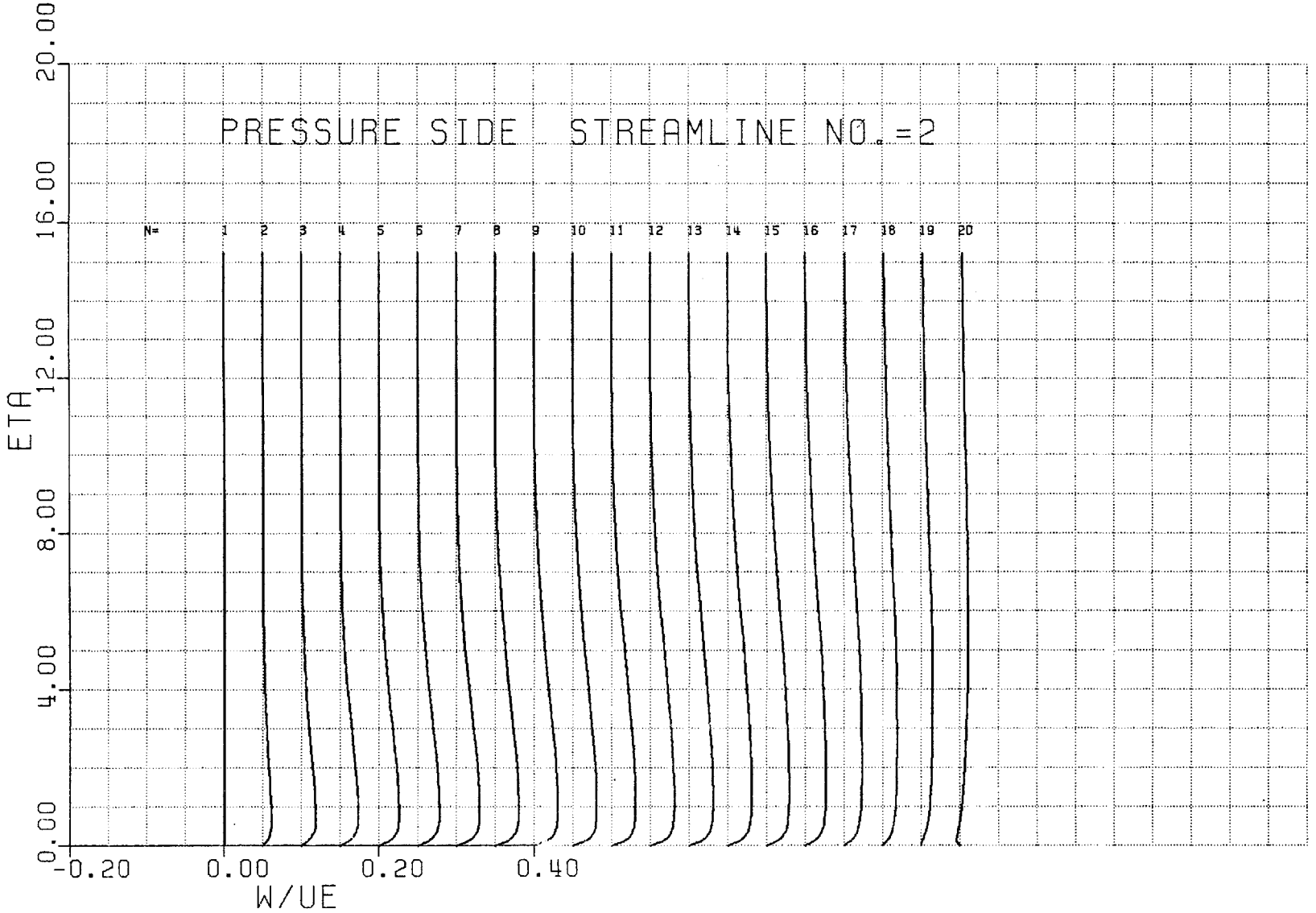

Figure 38. Crossflow velocity profile development, Streamline 2, Pressure side.

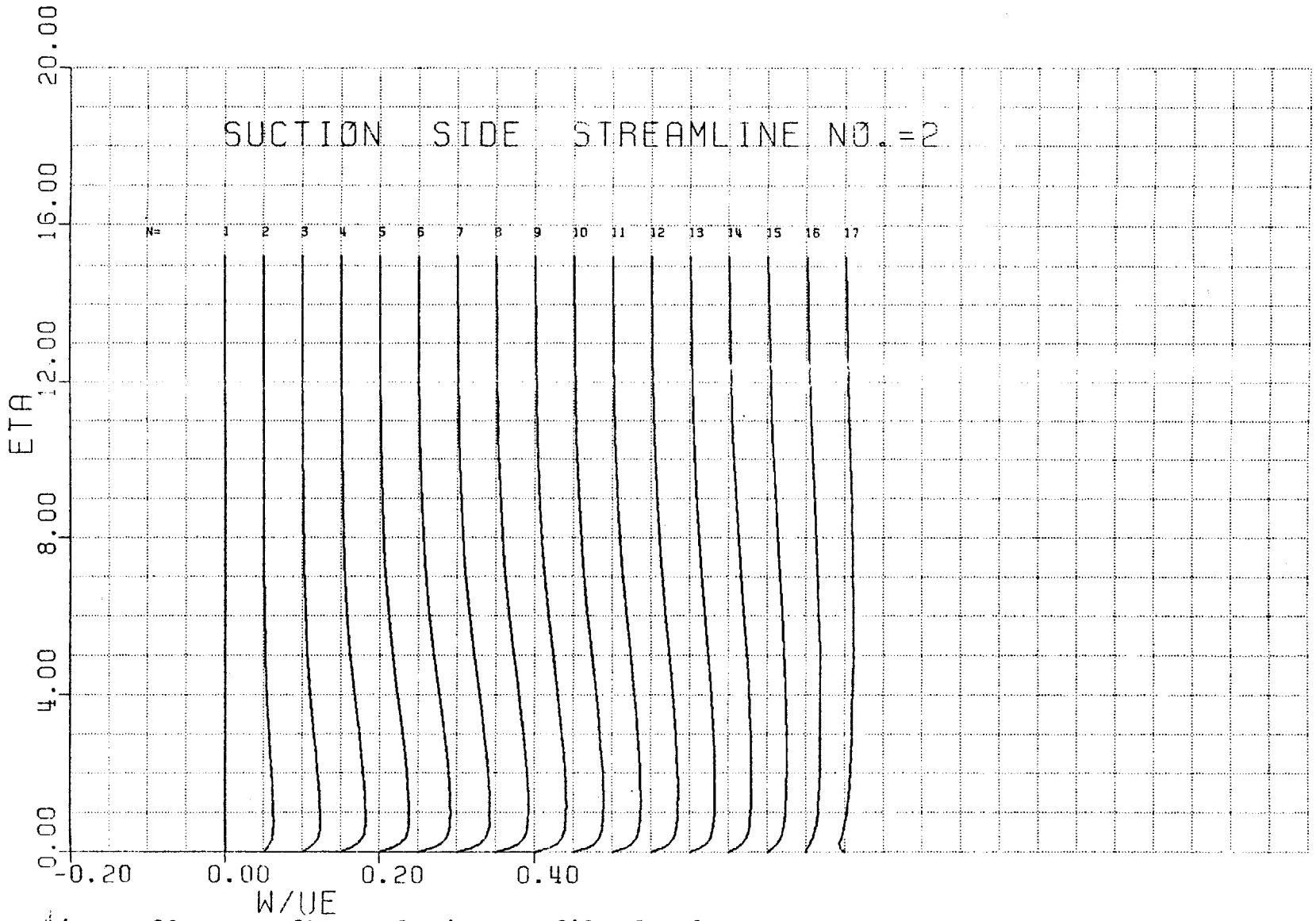

Figure 39. Crossflow velocity profile development, Streamline 2, Suction side.

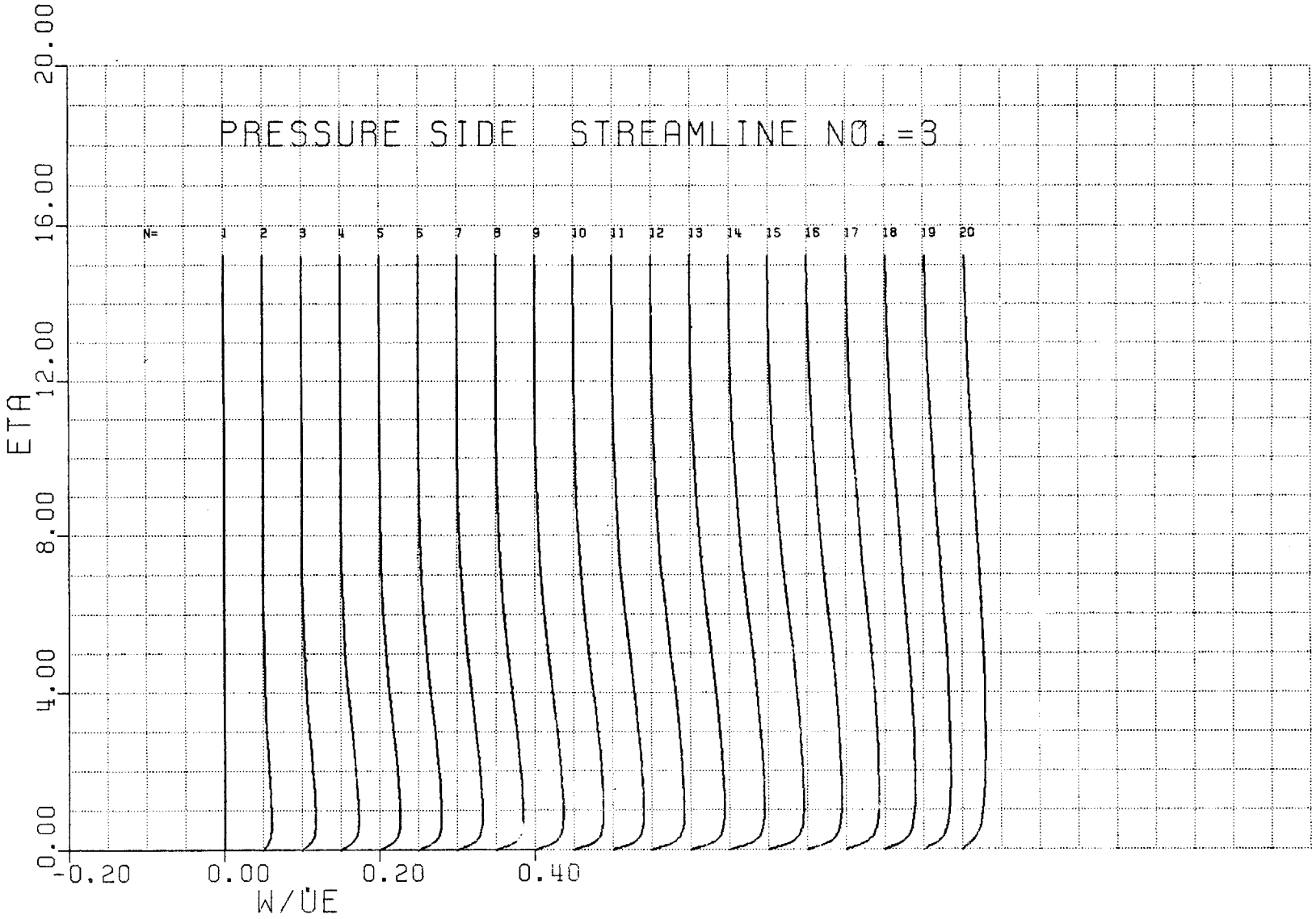

Figure 40. Crossflow velocity profile development, Streamline 3, Pressure side.

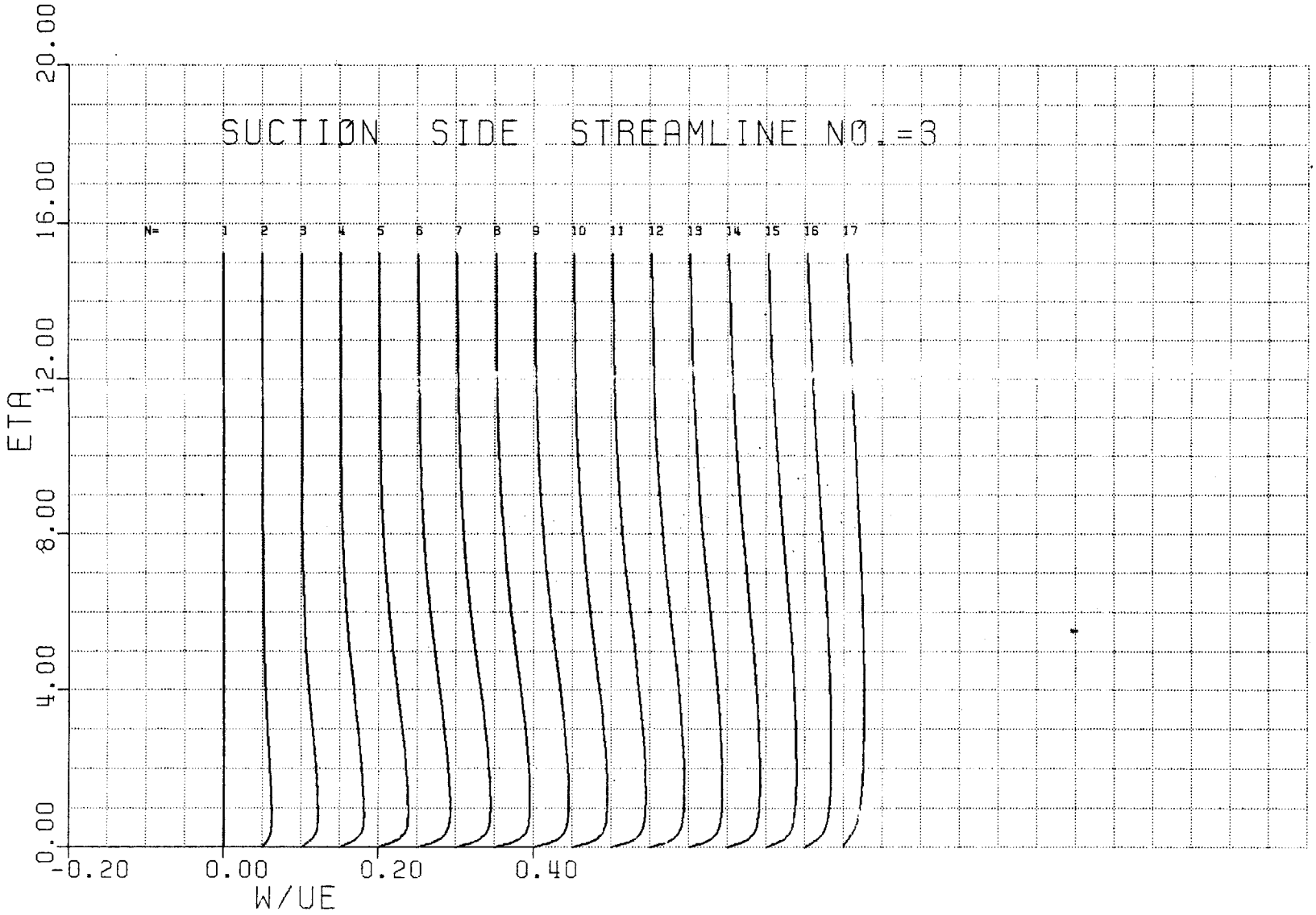

Figure 41. Crossflow velocity profile development, Streamline 3, Suction side.

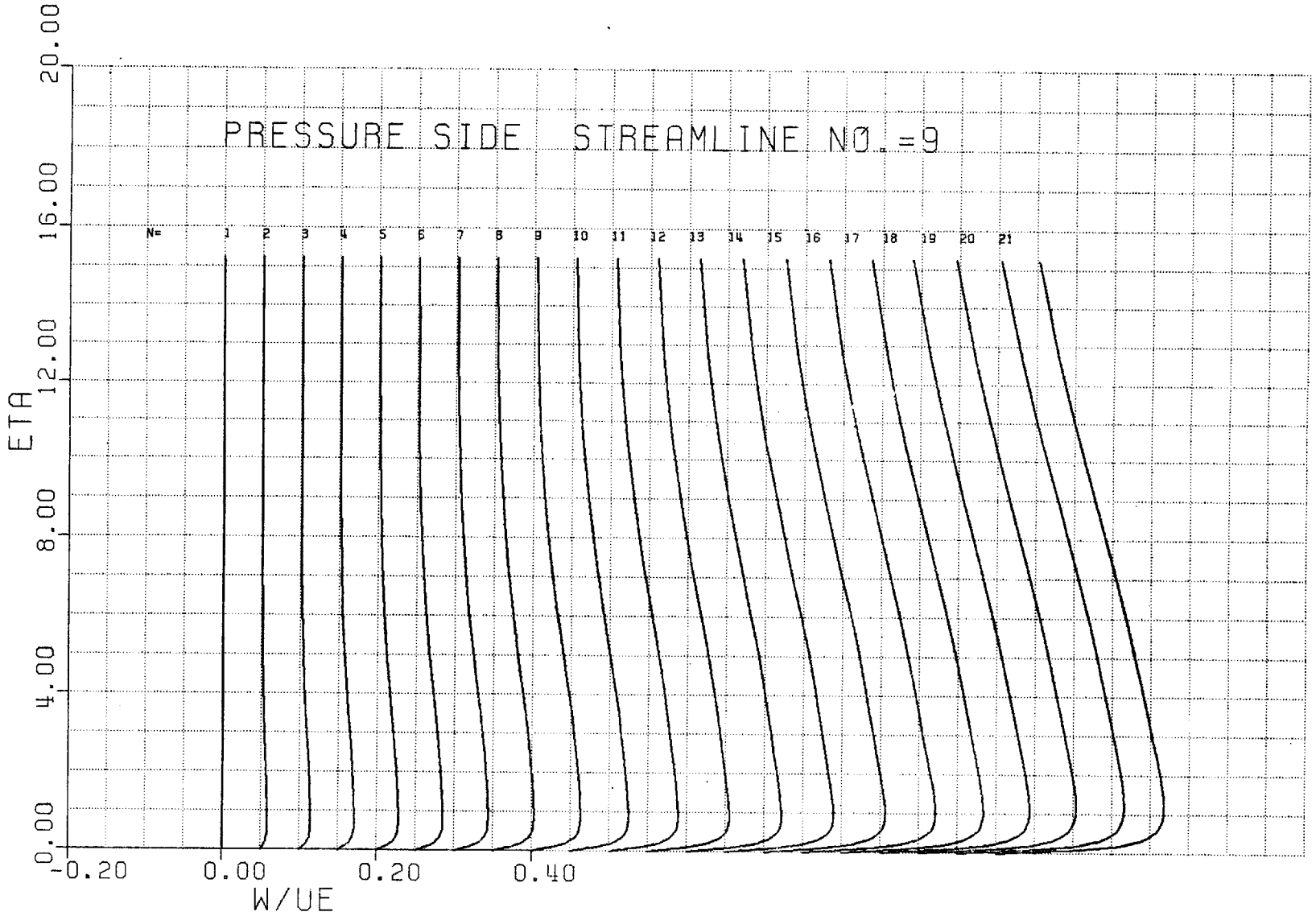

Figure 42. Crossflow velocity profile development, Streamline 9, Pressure side.

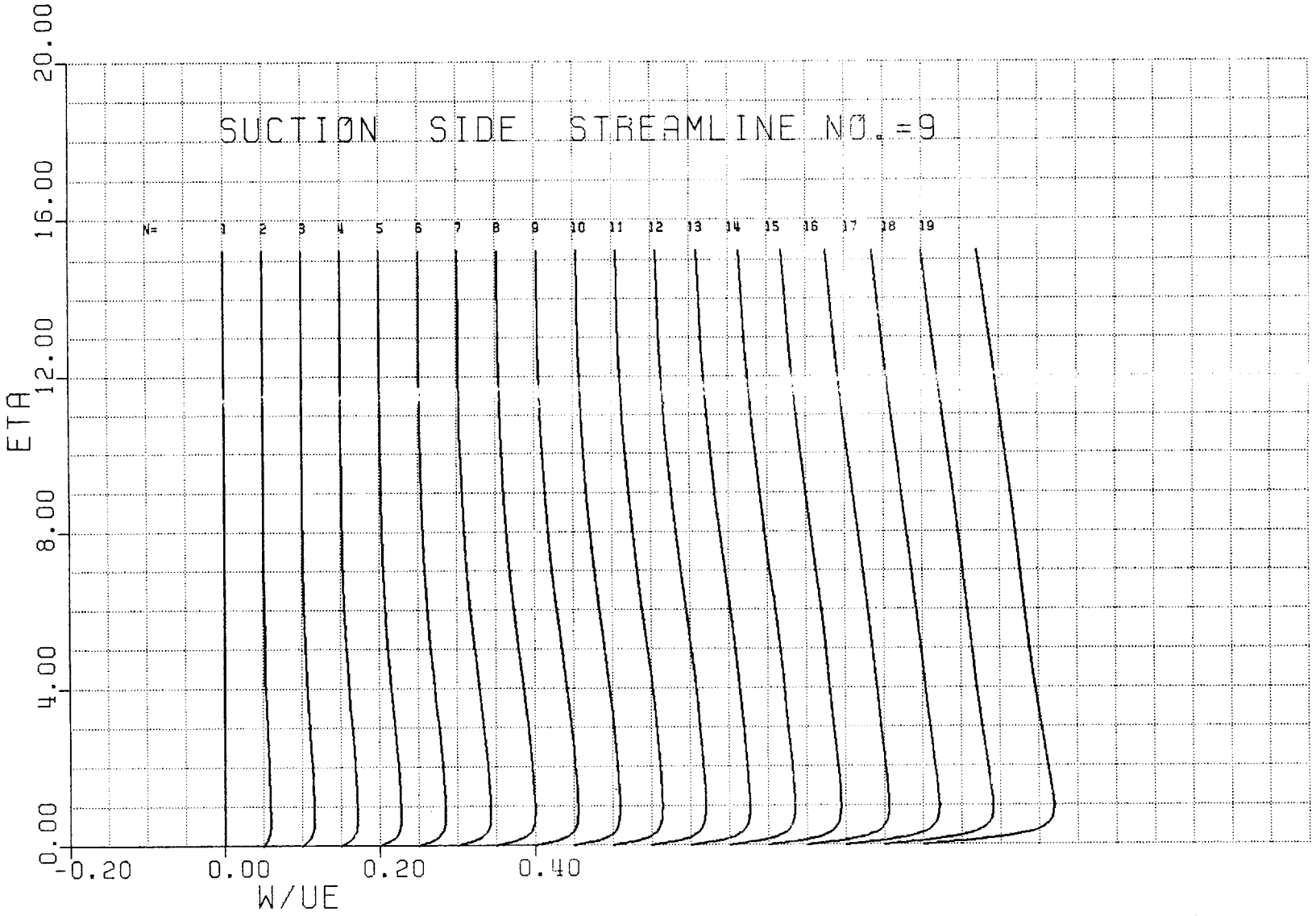

Figure 43. Crossflow velocity profile development, Streamline 9, Suction side.

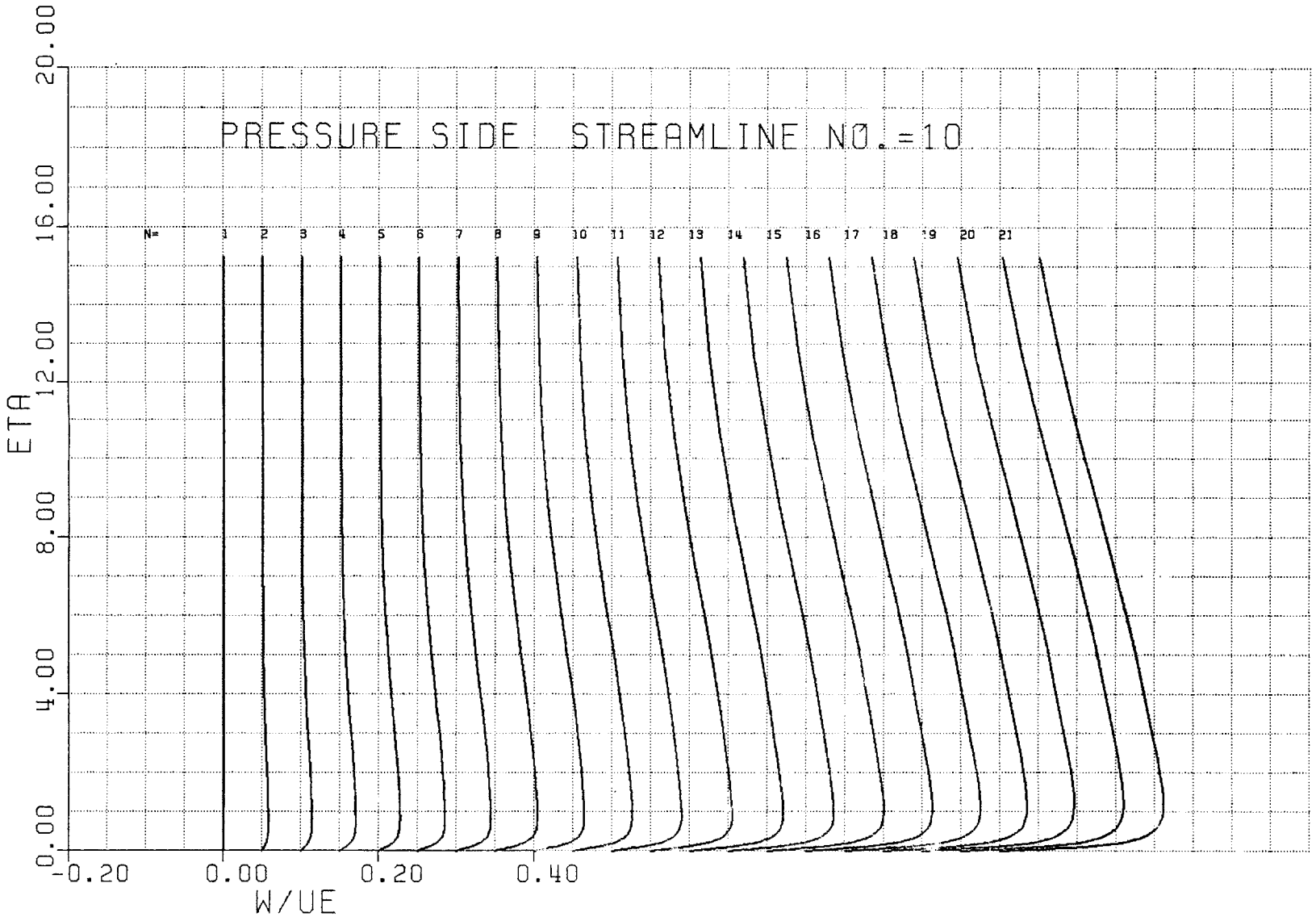

Figure 44. Crossflow velocity profile development, Streamline 10, Pressure side.

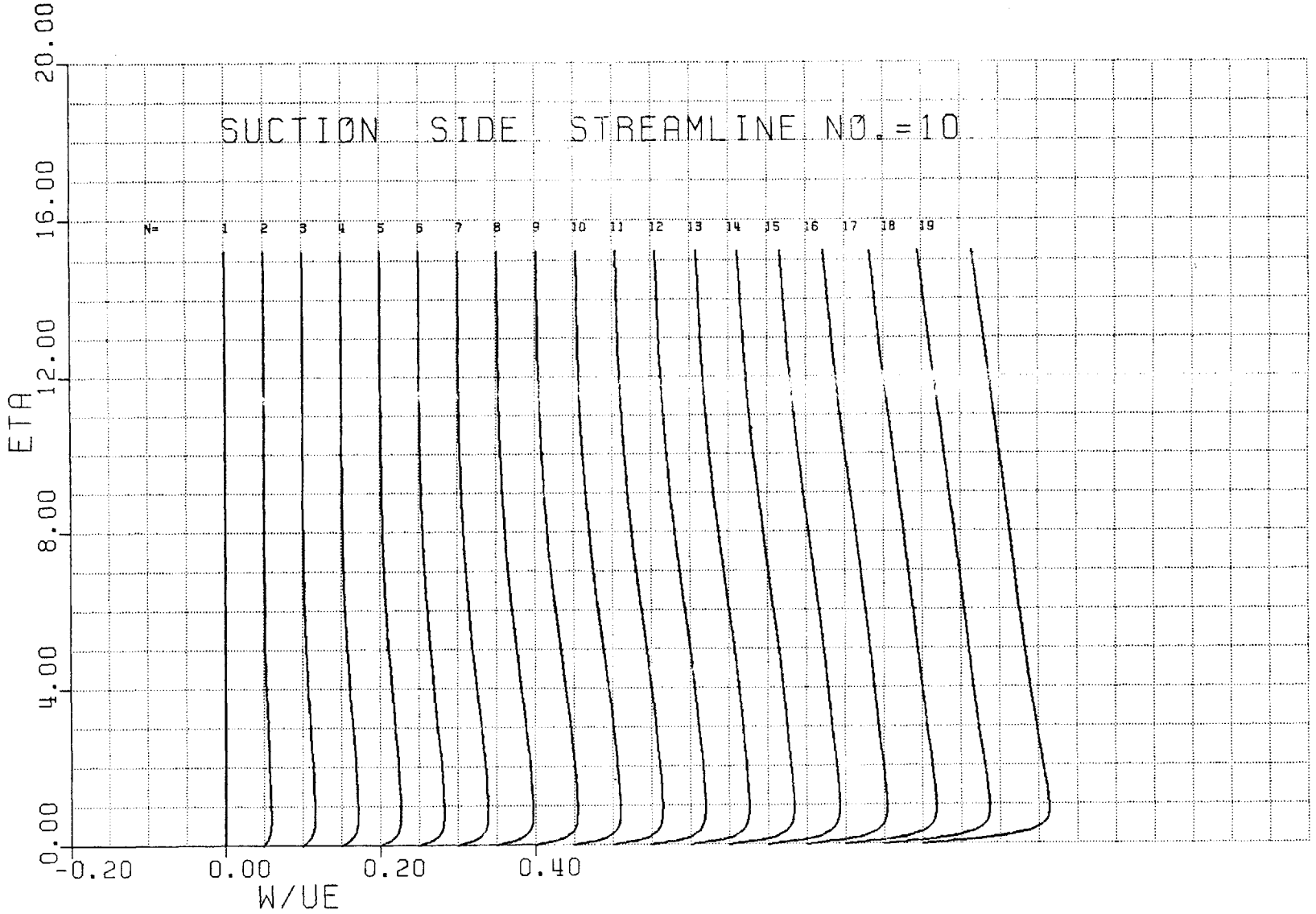

Figure 45. Crossflow velocity profile development, Streamline 10, Suction side.

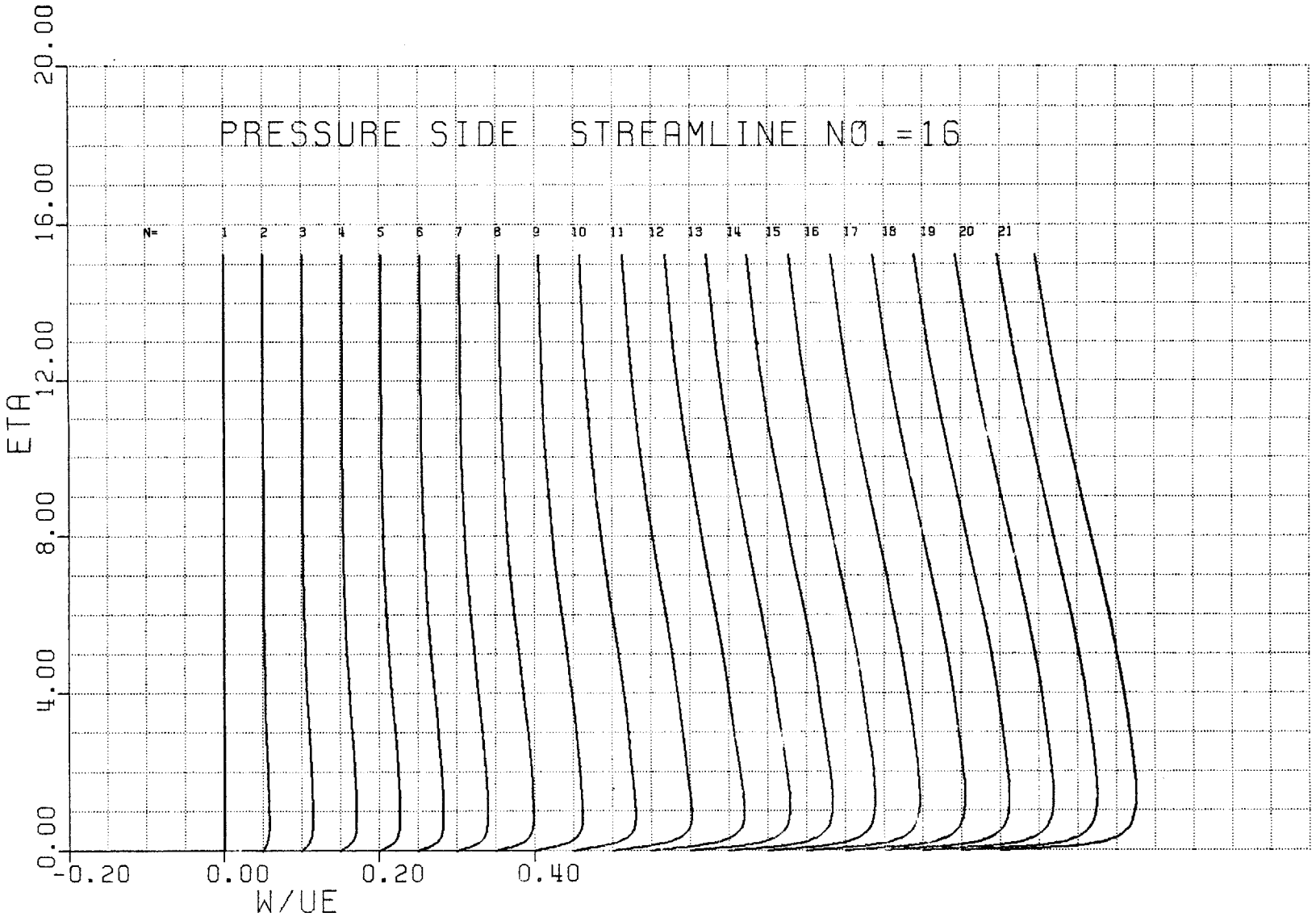

Figure 46. Crossflow velocity profile development, Streamline 16, Pressure side.

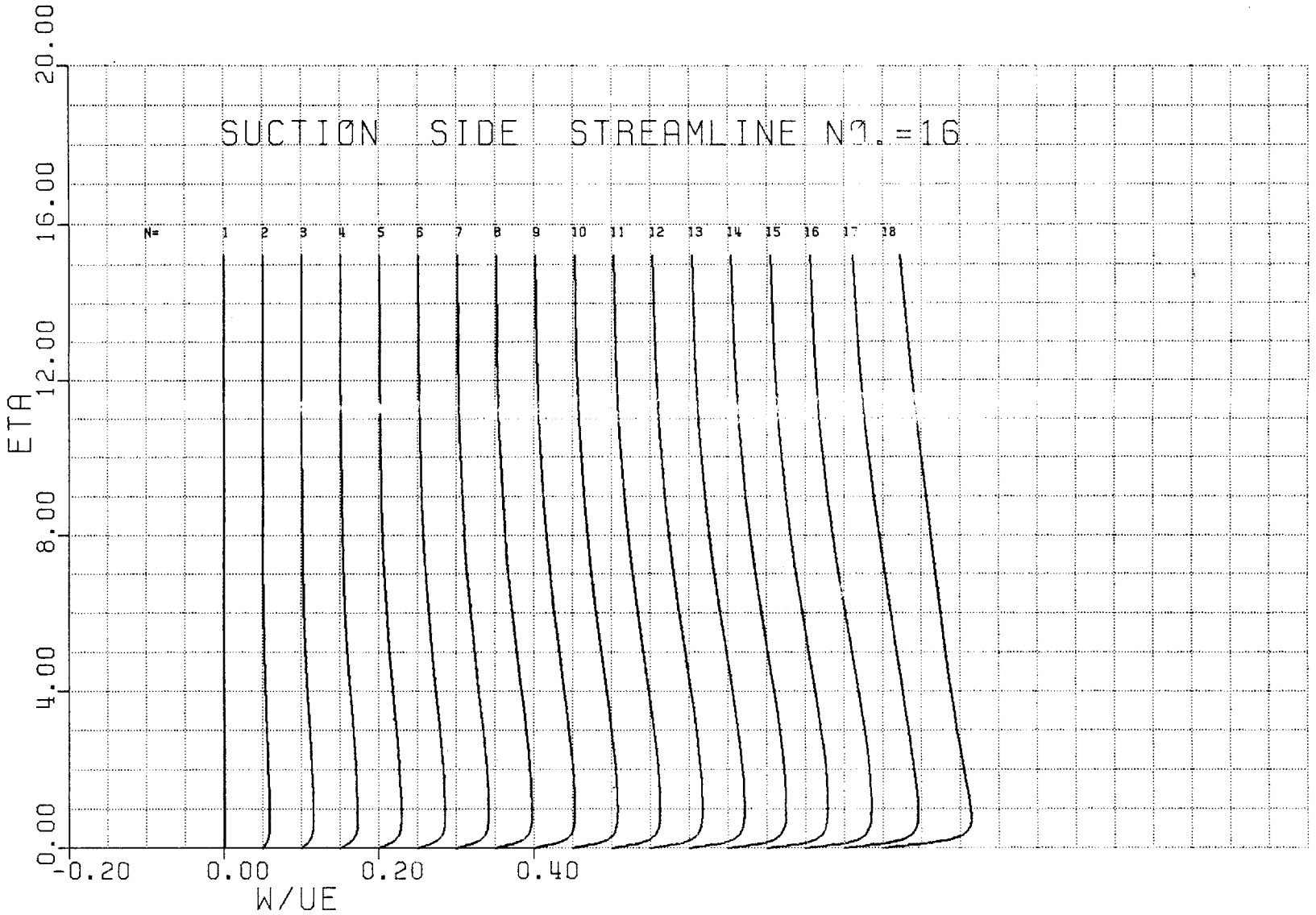

Figure 47. Crossflow velocity profile development, Streamline 16, Suction side.

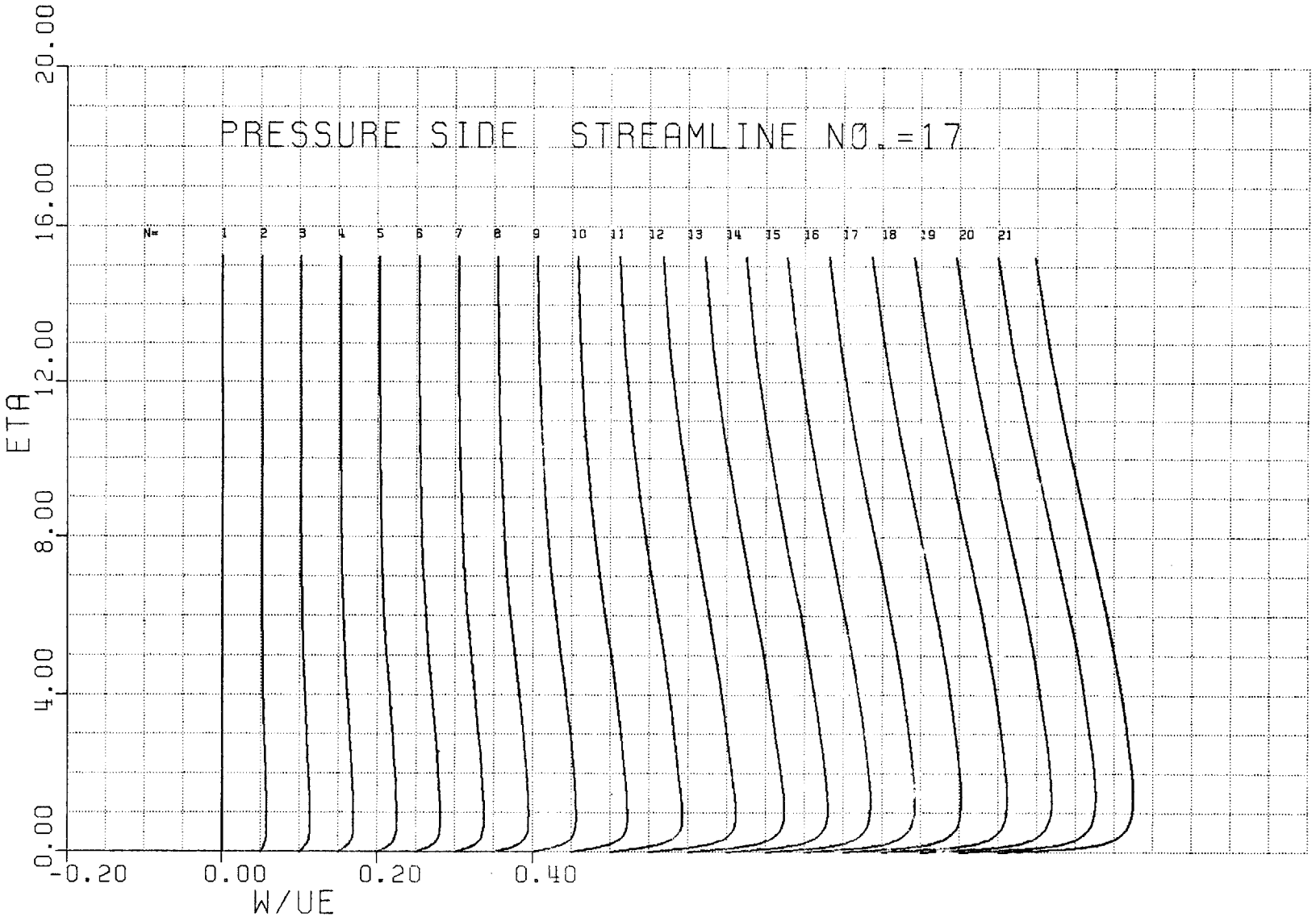

Figure 48. Crossflow velocity profile development, Streamline 17, Pressure side.

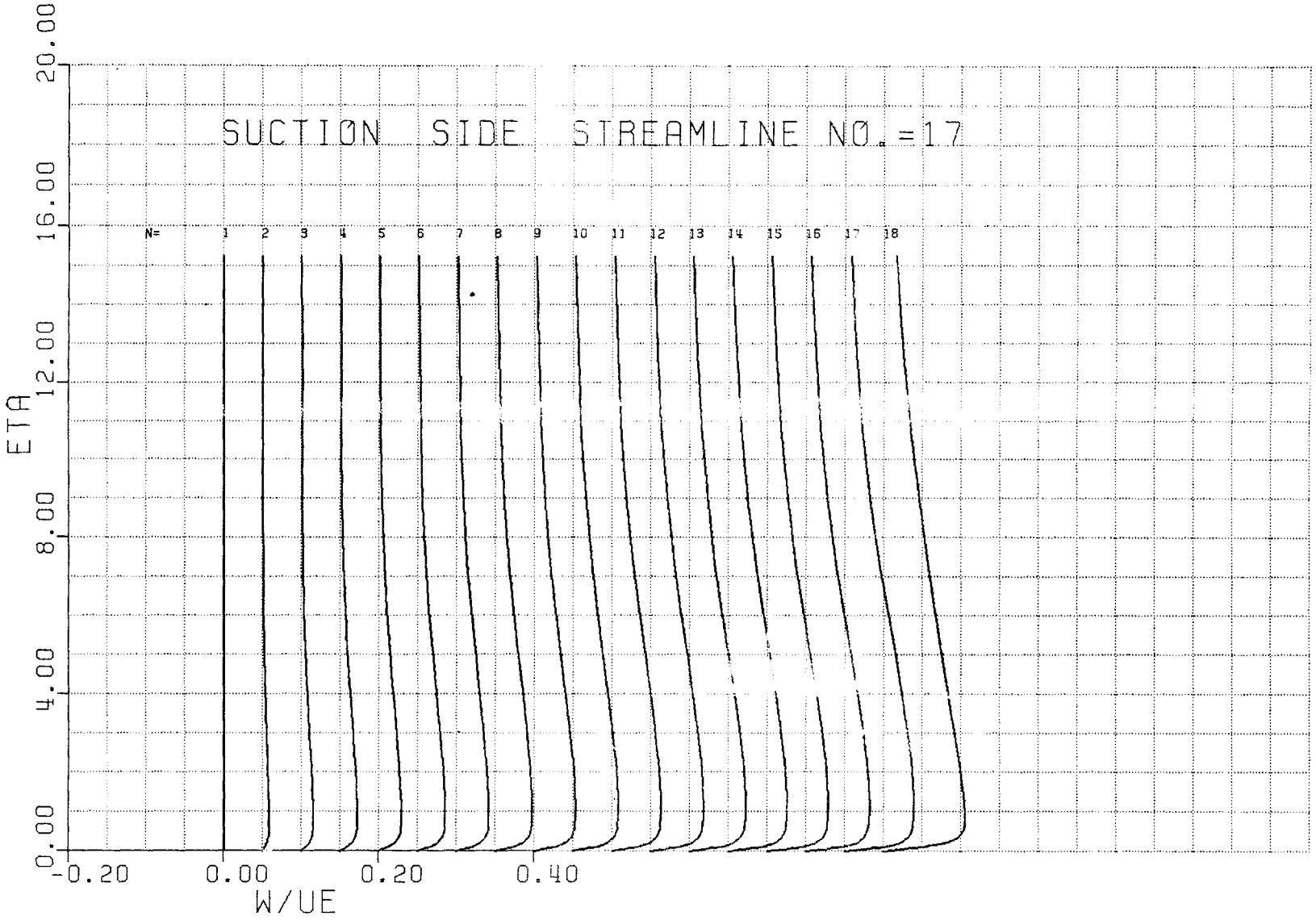

Figure 49. Crossflow velocity profile development, Streamline 17, Suction side.

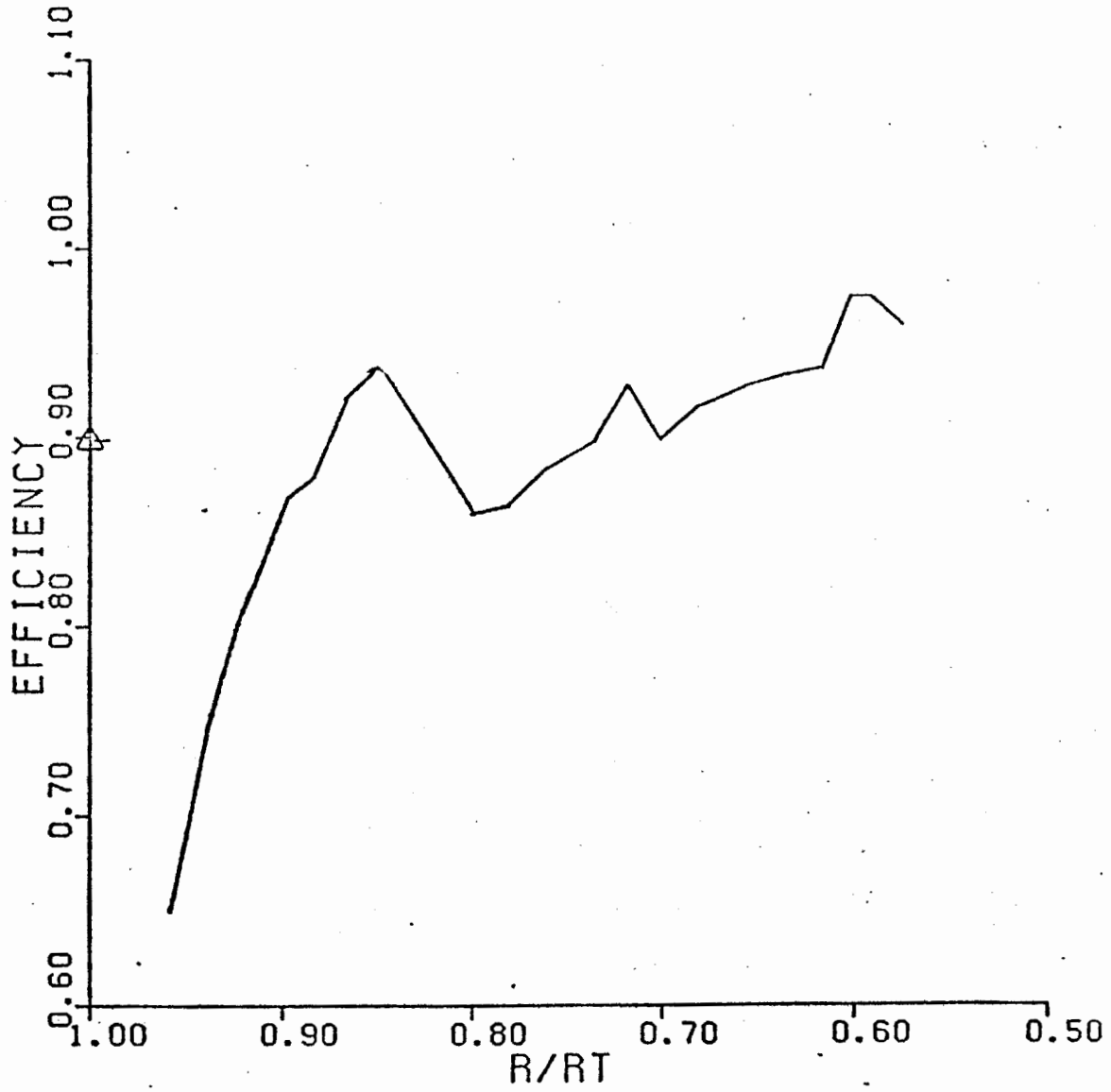

Figure 50. Rotor measured efficiency.